Magnetization Reversal Dynamics in Ferromagnetic Semiconductors

THÈSE N^{O} 4943 (2011)

PRÉSENTÉE LE 31 MARS 2011

À LA FACULTÉ SCIENCES DE BASE
LABORATOIRE DE SCIENCE À L'ÉCHELLE NANOMÉTRIQUE
PROGRAMME DOCTORAL EN PHYSIQUE

ÉCOLE POLYTECHNIQUE FÉDÉRALE DE LAUSANNE

POUR L'OBTENTION DU GRADE DE DOCTEUR ÈS SCIENCES

PAR

Liza HERRERA DIEZ

acceptée sur proposition du jury:

Prof. M. Q. Tran, président du jury
Prof. K. Kern, directeur de thèse
Prof. J.-Ph. Ansermet, rapporteur
Prof. D. Pescia, rapporteur
Dr J. Wunderlich, rapporteur

ÉCOLE POLYTECHNIQUE
FÉDÉRALE DE LAUSANNE
Suisse
2011

For what is Nature? Nature is no great mother who has borne us.
She is our creation. It is in our brain that she quickens to life.
Things are because we see them [...]

Oscar Wilde

Abstract

This thesis is dedicated to the study of the magnetization reversal dynamics in compressively strained (Ga,Mn)As and differently functionalized (Ga,Mn)As materials.
In the first part the domain wall dynamics of pure (Ga,Mn)As/GaAs materials is in the focus. The changes in the magnetic anisotropy energy landscape occurring as a function of temperature are monitored in detail by different experimental techniques. These measurements provide the necessary information for the identification of the temperature ranges corresponding to different magnetic anisotropy regimes. Knowing the biaxial anisotropy and uniaxial anisotropy dominated regimes the dependence of the domain wall dynamics on the magnetic anisotropy landscape is studied. Critical changes in domain wall alignment observed by Kerr microscopy are found upon changing from biaxial to uniaxial anisotropy. This changes could be partially attributed to the tendency of the system to minimize magnetic free poles at the domain boundaries.
To complement the space resolved studies of the magnetization reversal, magnetic time relaxation effects are addressed. In particular the magnetic aftereffect in (Ga,Mn)As/GaAs is studied in detail. The irreversible aftereffect is evidenced as a critical reduction of the domain wall velocity with time under a constant applied magnetic field below coercivity. This time relaxation is tracked as a function of both time and magnetic field. The measurements show that the overall relaxation is composed of two relaxation processes acting in parallel at short and long time scales. By fitting these experimental results the values of the relaxation times of both relaxation processes were obtained. By this modeling also the values of the activation volumes for two independent (Ga,Mn)As materials are estimated.
In the second part of this thesis the possibilities of tuning the electrical and magnetic properties of (Ga,Mn)As by volume and surface treatments are explored. As for the volume modification, oxygen species were incorporated into the (Ga,Mn)As films by means of exposure to an oxygen plasma. The incorporation of oxygen was evidenced by depth profile X-ray photoelectron

spectroscopy. This treatment is found to weaken the ferromagnetism, visible as a reduction in the Curie temperature, and to hinder the electrical transport evidenced as an increase in the electrical resistance. In agreement with theories accounting for the hole mediated ferromagnetism in (Ga,Mn)As this behaviour was related to a hole compensation mechanism arising from the presence of oxygen impurities sitting in interstitial positions of the (Ga,Mn)As Zinc blende structure.
In the last part, the modulation of the electrical and magnetic properties via surface functionalization is presented. The effects produced by the adsorption of molecular species on (Ga,Mn)As are similar to those found after oxygenation, namely a strong weakening of the magnetic properties and an increase in the values of the electrical resistance. However, in this case the distinctive feature is provided by the possibility of regulating the hole quenching effect by exploiting the additional degree of freedom provided by the chemical properties of the adsorbates. The adsorbate chosen for these experiments are dye molecules that absorb light in the visible range, in this way allowing for a light modulated interaction with the substrate. Using this concept is was possible to observe a modulation of the ferromagnetic transition temperature, the coercive field and the electrical resistance upon illumination. These observations provide a proof of principle for the realization of photo-sensitized (Ga,Mn)As devices where the magnetic properties can be regulated by light.

Keywords: Ferromagnetic semiconductors, Kerr microscopy, magnetic anisotropy, magnetic domain walls, magneto-transport, hole mediated ferromagnetism, dye molecule adsorbates, oxygenation.

Zusammenfassung

Die vorliegende Dissertation behandelt das dynamische Magnetisierungsverhalten von kompressiv verspannten und verschieden funktionalisierten (Ga,Mn)As Schichten.
Im ersten Teil der Arbeit wird die Dynamik von Domänenwänden in reinen (Ga,Mn)As/GaAs-Materialien untersucht. Die Veränderung der magnetischen Anisotropie in Abhängigkeit der Temperatur wurde mit verschiedenen Techniken experimentell bestimmt. Dabei konnten zwei verschiedene Temperaturbereiche identifiziert werden, in denen jeweils einachsige (zweizählige) bzw. zweiachsige (vierzählige) Anisotropie dominiert. Das Verhalten der Domänenwände unter Magnetfeldänderungen wurde mit Kerr-Mikroskopie untersucht. Dabei wurden wesentliche Unterschiede in der Ausrichtung der Domänenwände beim Übergang von ein- zu zweiachsiger Symmetrie beobachtet, welche sich durch die Tendenz des Systems, die Anzahl der freien Magnetpole an den Domänengrenzen zu minimieren, erklären lässt.
Zusätzlich zu den räumlich aufgelösten Messungen wurde die zeitliche Relaxation der Magnetisierung untersucht, insbesondere wurde dabei auf die magnetische Nachwirkung in (Ga,Mn)As/GaAs eingegangen. Als Effekt der magnetischen Nachwirkung wurde dabei die kritische Verringerung der Domänenwandgeschwindigkeit bei konstantem Magnetfeld unterhalb der Koerzitivfeldstärke beobachtet. Eine genauere Untersuchung der Domänenwandgeschwindigkeit als Funktion von Zeit und äuerem Magnetfeld ergab, dass sich die Gesamtrelaxation aus zwei einzelnen Relaxationsprozessen mit verschiedenen Zeitkonstanten zusammensetzt. Durch Modellierung wurden sowohl die Zeitkonstanten bestimmt, als auch die Aktivierungsvolumina für zwei verschiedene (Ga,Mn)As-Materialien bestimmt.
In zweiten Teil der Arbeit wurden die elektrischen und magnetischen Eigenschaften von (Ga,Mn)As durch Behandlung der Oberfläche oder des Volumens verändert.
Durch den Kontakt der (Ga,Mn)As-Schichten mit einem Sauerstoffplasma wurde Sauerstoffatome im gesamten Kristall eingelagert, was durch Tiefenprofilmessungen via Röntgenphotoelektronenspektroskopie (XPS) nachgewie-

sen wurde. Diese Behandlung vermindert das ferromagnetische Verhalten durch eine Reduzierung der Curie-Temperatur und verschlechtert die elektrischen Transporteigenschaften, was durch einen Anstieg des elektrischen Widerstandes sichtbar wurde. Im Modell des ladungsträgerinduzierten Ferromagnetismus lässt sich dieses Verhalten durch eine Reduzierung der Löcher erklären, die durch Sauerstoffatome auf den Zwischengitterplätzen der Zinkblendestruktur von (Ga,Mn)As ausgelöst wird.
Im letzten Kapitel wird die Oberfläche der (Ga,Mn)As-Schichten durch Adsorption von Farbstoffmolekülen funktionalisiert. Ähnlich wie bei der Sauerstoffbehandlung führt dies zur Reduzierung der Löcher und damit zur Verringerung der ferromagnetischen Eigenschaften und einem erhöhten elektrischen Widerstand. Der Vorteil des Loch-Quenching durch Adsorption ist die Möglichkeit durch die Wahl des Adsorbaten das Verhalten weiter beeinflussen zu können.
Durch die Wahl von Farbstoffmolekülen, die im sichtbaren Licht absorbieren, lassen sich die Eigenschaften des Substrats durch optische Anregung manipulieren. Auf diese Weise konnten Veränderungen der ferromagnetischen Übergangstemperatur, der Koerzitivfeldstärke sowie des elektrischen Widerstands optisch kontrolliert werden. Diese Versuche stellen eine proof-of-principle-Studie zur Realisierung von lichtsensitiven (Ga,Mn)As-Bauteilen dar, bei denen magnetische Eigenschaften durch Licht kontrolliert werden können.

Schlagworte: Ferromagnetische Halbleiter, Kerr-Mikroskopie, magnetische Anisotropie, magnetische Domänwände, Magnetotransport, ladungsträgerinduzierter Ferromagnetismus, adsorbierte Farbstoffmoleküle, Sauerstoffplasma.

Contents

Abstract **i**

Zusammenfassung **iii**

1 Introduction **1**
1.1 Ferromagnetic semiconductors 1
1.1.1 From EuO to (III,Mn)V compounds 1
1.2 (Ga,Mn)As 3
1.2.1 Incorporating Mn into GaAs 3
1.2.2 Hole mediated ferromagnetism 6
1.2.3 Magnetic anisotropy 10
1.3 Magnetic domains and domain walls 15
1.3.1 The origin of magnetic domains 15
1.3.2 Structure and energy of domain walls 18

2 Experimental Methods **23**
2.1 Kerr microscopy 23
2.1.1 Magneto-optical Kerr effect 24
2.1.2 Magnetic contrast 29
2.1.3 The Kerr microscope and measurement set-up 31
2.2 Magneto-transport 33
2.2.1 Ordinary and anomalous Hall effect 34
2.2.2 Anisotropic magnetoresistance and Planar Hall effect . 36
2.2.3 Angle-resolved coercive field measurements 39

3 Magnetic domain wall dynamics in GaMnAs/GaAs **43**
3.1 Biaxial to uniaxial magnetic anisotropy transition in (Ga,Mn)As 43
3.1.1 Temperature dependent magnetic anisotropy 44
3.1.2 Magnetic domain wall alignment 48
3.2 Magnetic aftereffect in the biaxial anisotropy regime 53
3.2.1 The magnetic aftereffect 53

3.2.2 Time dependence of the magnetization 55
3.2.3 Modeling of the magnetic aftereffect 60

4 Electrical and magnetic properties of oxygenated (Ga,Mn)As 67
4.1 Oxygen incorporation into (Ga,Mn)As 68
4.1.1 Depth profile X-ray photoelectron spectroscopy 68
4.2 Magnetism and electrical transport in oxygenated (Ga,Mn)As 72
4.2.1 X-ray absorption spectroscopy 72
4.2.2 Magneto-transport 75

5 Optical-gating of photo-sensitized (Ga,Mn)As 81
5.1 Functionalization of (Ga,Mn)As 82
5.2 GaMnAs/organic-dye system in the absence of light 83
5.2.1 Fluorescein on (Ga,Mn)As 84
5.2.2 Effect of the electronegativity of the adsorbates' substituents 87
5.2.3 Magnetic anisotropy and transport properties in the absence of light 89
5.3 Manipulating magnetism by light 91
5.3.1 Magnetic properties in the presence of light 91
5.3.2 Time relaxation of the light induced state 92

Summary and conclusions 97

Appendix 101

Bibliography 102

Publications 113

Curriculum vitae 115

Acknowledgments 117

Chapter 1

Introduction

1.1 Ferromagnetic semiconductors

The link between semiconductor physics and magnetism is a question that has drawn the attention of the research community since decades both with scientific and economic interest. The electronic properties of semiconductors are the key for information processing as much as magnetism is at the heart of information storage technologies. It is obvious that the possibility of realizing information processing and storage with the same material would enhance the performance of current devices and therefore have an enormous technological impact. On the other hand, the properties of a magnetic semiconductor system can reveal new exciting physics where the interaction between electric charge carriers and local magnetic moments plays an important role.
In this introductory chapter a short review of the evolution of magnetic semiconductor research will be given starting from the first specimens to the most recent generation of high ferromagnetic transition temperature materials including (Ga,Mn)As. The latter has been extensively quoted in the literature as a model system for the study of ferromagnetic semiconductors and is also the subject of this work. The second part of this chapter will be dedicated to a recount of its most distinctive and relevant properties.

1.1.1 From EuO to (III,Mn)V compounds

The first successful attempts to realize ferromagnetic semiconductor materials can be traced back to 1961 when EuO presented semiconducting properties and a Curie temperature of 69 K [1] making Europium chalcogenides the subject of intense research [2]. However, a new record for the Curie temperature could not be established by any other Eu chalcogenide [3] in addition to the highly difficult growth of these crystals. The impossibility of reaching

room temperature operation became clear and consequently the idea of the industrial application of these compounds seemed unrealistic. Years later, a great advancement in terms of functionality was made when carrier-mediated ferromagnetism was demonstrated in PbSnMnTe [4]. A link between electrical and magnetic properties which is the key for novel spintronics applications was now at hand, however, the highest ferromagnetic transition temperature achievable was between 4 and 5 Kelvin, again well below technologically relevant values [4, 5].

Little time passed until the strategy that proved most successful in achieving both higher Curie temperatures and semiconducting properties was reported. It was based on introducing magnetic moments in well known semiconductor materials forming the so-called diluted magnetic semiconductors. The first attempts were centered mostly around Mn doped II-VI semiconductors such as CdTe and ZnSe. Even though these compounds are easy to prepare due to the fact that the valence of the cations in the semiconductor matches that of Mn there was a key difficulty lying in the realization of n or p doping which is vital for practical applications. In addition, the magnetic order in these compounds is dominated by the antiferromagnetic interaction between the Mn centers. The only achievable ferromagnetic response was rather weak with a Curie temperature below 2 K [6] due to the presence of different types of non-ferromagnetic interactions in the material. After this first step, research turned towards the Mn doping of (III,V) semiconductors which produced a series of pioneering publications in the 1990s [6–9] that showed the possibility of increasing Curie temperatures of ferromagnetic semiconductors far beyond what had been achieved so far. As already mentioned, the most representative material from this group of compounds is (Ga,Mn)As which holds the record for the highest Curie temperature of 170 Kelvin. Although this material is the result of a great scientific effort, practical applications can only be thought of in the presence of room temperature operation. Even though mean-field theories predict that room temperature ferromagnetism could be achieved in diluted ferromagnetic semiconductors [10] provided a high enough carrier and Mn concentrations, at the moment a Curie temperature of 170 Kelvin in (Ga,Mn)As seems to be a fundamental limit.

Ongoing scientific activity is dedicated to the search of new materials with higher Curie temperatures while conserving the charge carrier influence on the magnetic properties. Among these candidates the most promising is (Zn,Cr)Te that presents room temperature ferromagnetism and the desired coupling between charge carriers and magnetic moments [11]. In addition, oxides such as (Zn,Mn)O [12] or (Sn,Fe)O_2 [13] present high Curie temperatures, however, further investigation is needed to elucidate the mechanism behind the ferromagnetism in this systems and most importantly whether it

can be electrically modulated.
As already mentioned industrial applications of (Ga,Mn)As might not be achievable, however, this system provides a unique playground for studying the most interesting physics behind the interplay between magnetism and electrical properties. The discovery of new effects and properties for the benefit of basic research will also help greatly to the design of a new generation of materials that could overcome the known difficulties and finally be incorporated in new technologies.
The upcoming section deals with the most important facts and concepts about (Ga,Mn)As that are relevant to the research reported in this thesis.

1.2 (Ga,Mn)As

1.2.1 Incorporating Mn into GaAs

The largest difficulty in producing (III,Mn)V ferromagnetic semiconductors is the low solubility of the magnetic species in the semiconductor material. This problem could be overcome by the use of low temperature molecular beam epitaxy (MBE). Working in non-equilibrium conditions Mn concentrations higher than the solubility limit [9] can be realized inside the semiconductors avoiding the formation of secondary phases such as MnAs clusters. The segregation of a second phase is impeded by the lack of thermal energy and instead the epitaxial growth of a single crystal alloy becomes possible. Other techniques such as ion implantation [14] and laser deposition [15] were employed for the growth of (Ga,Mn)As but none has proved as reliable and efficient as molecular beam epitaxy.
(Ga,Mn)As films are typically grown on GaAs, (Ga,In)As or (Ga,Al)As epitaxial buffer layers supported by semi-insulating GaAs substrates. Working in non-equilibrium conditions makes the quality of the films very sensitive to the growth temperature. A typical value for the growth temperature of (Ga,Mn)As is 250 °C [16] and typical growth rates are of the order of 0.6μm/hour. The layer by layer growth, an indication of the absence of secondary phases, is normally verified during growth by monitoring the (1x2) reconstruction of the (Ga,Mn)As surface in a reflection high energy electron diffraction (RHEED) pattern. The signature of the (1x2) reconstruction is the appearance of well defined streaks in the RHEED pattern which in the case of undesired three dimensional growth becomes a complex spotty pattern [17]. A phase diagram is shown in Fig. 1.1 where all the possible phases in the growth of (Ga,Mn)As are illustrated as a function of the growth temperature and the Mn composition. The growth temperature range where

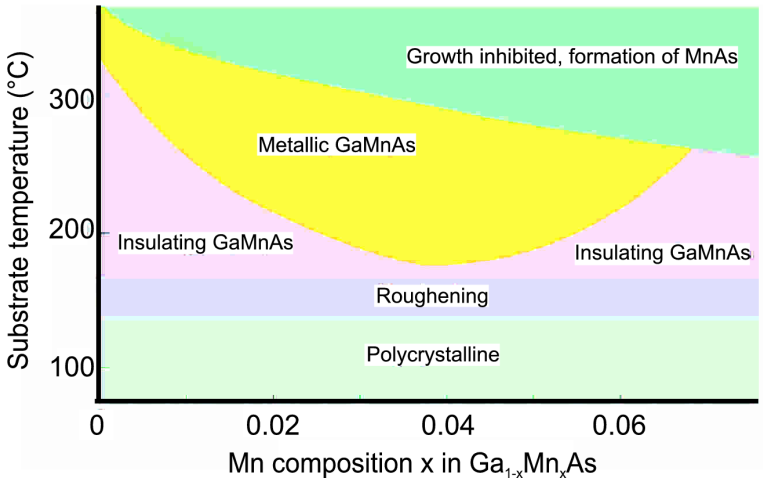

Figure 1.1: Phase diagram illustrating the different phases in the growth of (Ga,Mn)As as a function of growth temperature and Mn composition (after Ohno *et al.* [6])

single crystalline (Ga,Mn)As can be obtained (pink and yellow areas) narrows down as the Mn concentration is increased. In addition, within this range both parameters can be tuned to obtain (Ga,Mn)As crystals with electrical properties in the metallic and insulating regime [6].
The low temperature epitaxial growth is a powerful method for the incorporation of Mn atoms into GaAs beyond the solubility limit, however, the non-equilibrium nature of the growth determines certain limitations. Under these low temperature conditions, besides the desired Mn^{2+} in high spin configuration sitting in Ga^{3+} sites a variety of lattice defects in the structure of (Ga,Mn)As are expected to occur [6, 18]. Among these the most common are As anti-site defects (As atoms sitting on Ga sites) and Mn interstitial atoms, both affecting the magnetic and electrical properties of the (Ga,Mn)As films. The electronic characteristics of the As_{Ga} defects can vary from zero charge to double ionized for paramagnetic and ferromagnetic samples, respectively [19]. In addition, depending on the relative arrangement of As anti-site defects with respect to the surrounding Mn atoms a ferromagnetic or antiferromagnetic interaction can be mediated by the As defects between the neighboring magnetic centers [18]. The location of these defects in the zinc blende structure of (Ga,Mn)As, the correct stoichiometric arrangement of As and Ga atoms and the substitutional Mn atoms are summarized in Fig. 1.2. As will be described in detail later in this chapter atoms sitting on Ga sites act as electron donors [19] compensating the p-type car-

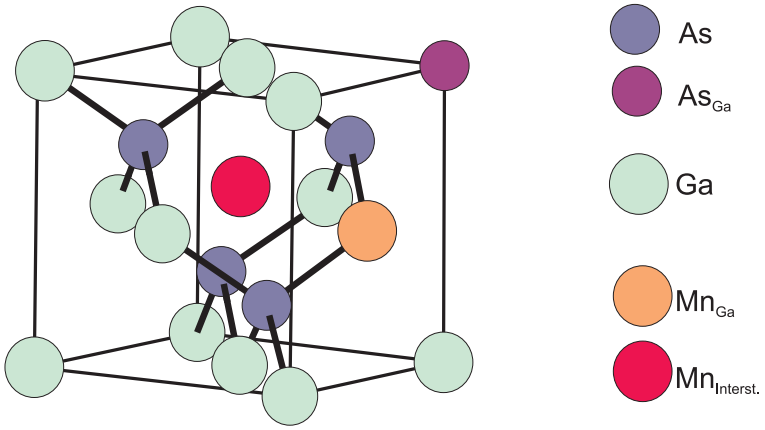

Figure 1.2: Different types of lattice defects in the zinc blende structure of (Ga,Mn)As (after MacDonald *et al.* [5]). The most common defects are As antisites and Mn interstitial atoms.

riers provided by the incorporation of Mn in the film and therefore reducing the conductivity and weakening the ferromagnetic order. In order to prevent hole compensation or an eventual antiferromagnetic coupling between Mn centers the epitaxial growth of (Ga,Mn)As has to be carried out in low As pressure conditions to avoid the formation of As-related defects defects [20]. The incorporation of a considerable amount of Mn atoms into GaAs is a key point to realize ferromagnetism. But not only the amount of Mn is important. The magnetic atoms should occupy specific positions in the lattice to contribute to the collective ferromagnetic interaction in the material. These positions are those occupied by Ga atoms in pure GaAs. However, it has been widely observed that Mn tends to occupy not only these substitutional positions but also lattice interstitial sites [21]. The value of the lattice constant of (Ga,Mn)As as a function of the atomic percentage of Mn incorporated can be a measure of the amount of Mn that occupy substitutional positions. The lattice parameter a can be determined by X-ray diffraction and its linear variation with the Mn concentration following Vergard´s Law [9,22] accounts for the full incorporation of Mn in substitutional sites. In this case also accurate values for the lattice constant of GaAs and MnAs [6,22] can be obtained by extrapolation to x= 0 and 1, respectively. Deviations from Vergard´s Law are a good indication of the presence of defects in the (Ga,Mn)As lattice and in particular of interstitial Mn which is also distinctively reflected in the electrical and magnetic properties of (Ga,Mn)As as described in the following.

Each Mn atom sitting on a Ga^{3+} site provides a p-type carrier that medi-

ates the ferromagnetic order with other substitutional Mn^{2+} ($3d^5$). On the other hand, interstitial manganese counteracts the effects of the substitutional manganese acting as a double donor [24] and coupling antiferromagnetically with the substitutional Mn atoms [25]. In this way, it is often observed that in the presence of Mn atoms in interstitial positions the Mn density in (Ga,Mn)As is larger than the p-carrier density [26] and that the saturation magnetization is too small to account for the expected 4-5 μ_B per atom [27]. These difficulties can be overcome by annealing of the films at temperatures comparable or lower than the growth temperature [28]. During annealing the interstitial manganese atoms are driven towards the surface with a diffusion barrier that is affected by the electric field of the substitutional Mn atoms and is of the order of 0.8 eV [29]. In this way, the ferromagnetic properties and the electrical conductivity of (Ga,Mn)As films can be significantly improved by low temperature annealing. Moreover, this effect can be enhanced by performing the annealing procedure under oxygen atmosphere. In this case the interstitial manganese atoms of the film are also passivated through oxidation once they have diffused to the surface [30].

1.2.2 Hole mediated ferromagnetism

In this section, the most accepted theory accounting for the carrier mediated ferromagnetism in (Ga,Mn)As will be described. This theory is based on a Zener-mean field theory that can successfully model to a large extent the results from various measurement techniques, however, it is also found to fail when predicting properties such as Curie temperatures as high as room temperature for certain Mn doped semiconductors. This theory represents a mayor advancement in the understanding of the properties of these novel systems, however, many questions still remain open regarding the mechanism of the hole mediated ferromagnetic interaction in (III,Mn)V diluted magnetic semiconductors and in particular (Ga,Mn)As.
The most cited theory describing the ferromagnetic interaction in these systems was developed by *Dietl* and is based on the exchange interaction between charge carriers and localized spins first proposed by *Zener* [31, 32] for magnetic metals. The *Zener* theory was not particulary suitable for magnetic metals since it pictures a competition between ferromagnetic and antiferromagnetic interactions that leads rather to a spin-glass than to a ferromagnetic ground state. However, in semiconductors it becomes relatively accurate and also equivalent to the well known theory developed by Ruderman, Kittel, Kasuya, and Yosida (RKKY) [33, 34]. The key point for this success is that the mean distance between the carriers in ferromagnetic semiconductors is much greater than between the spins. Under these conditions the exchange interac-

tion mediated by the carriers is mostly ferromagnetic reducing the tendency towards the spin-glass state.
In Dietl's theory Mn atoms act on the one hand as a source of localized 5/2 spins and on the other hand as effective acceptors where the magnetic d electrons do not contribute to the charge transport. In this picture, the holes residing in the valence band couple antiferromagnetically with the Mn spins resulting in an effective spin-spin long range ferromagnetic interaction that can be treated within the mean-field approximation [35]. In particular, Dietl's theory puts special emphasis in incorporating spin-orbit interactions to the Zener model. Along these lines, this modified Zener model becomes a very powerful tool for accurately calculating parameters such as Curie temperature, saturation magnetization or magnetic anisotropy for zinc blende and wurzite semiconductors and in particular for (Ga,Mn)As. Perhaps the most remarkable result of this mean field approach is the prediction of the proportionality between the Curie temperature and the cubic root of the carrier density ($T_c \propto p^{1/3}$)which has been extensively used to accurately model many experimental studies in the literature [36].

For a better understanding of the coupling between the holes and the Mn magnetic moments the orbital character of the valence band states will be shortly addressed. The top of the valence band in GaAs consists of levels that have $4p$ character. This originates from the contributed Ga and Ar 4p atomic orbitals, however, the resulting band states have not an equal contribution from Ga and As but are heavily weighted on the As atomic orbitals [37]. Since the Mn d electronic levels reside within the valence band of the GaAs host p-d hybridization is found to dominate the interaction between the holes and the magnetic moments of the Mn atoms. This argument is the key for the antiferromagnetic interaction between the holes and the Mn moments [38]. The p-d exchange interaction can be presented in a simple physical picture applicable when the problem is treated in the framework of the mean field theory. Suppose that the filled spin-down levels in the Mn d-shell have a certain energy corresponding to GaAs levels deep in the valence band and that the empty Mn d spin-up levels are located above the Fermi level in the conduction band. Under these circumstances hybridization of the p and filled d levels can occur. Hybridization is understood as the level repulsion of states having the same spin, which in this case will produce a shift of the levels in the valence band that have the same spin state as the Mn d shell (spin-down) to higher energies relative to the energy of the spin-up valence band levels. This electronic hybridization process is the origin of the antiferromagnetic coupling between the valence band states and the Mn local magnetic moments since the majority hole carriers will be created in spin-down states. This simple picture explaining the effective ferromagnetic

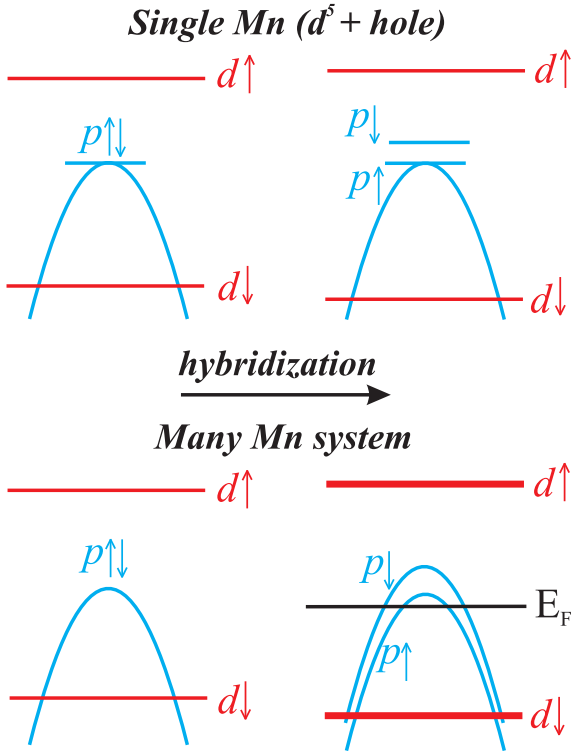

Figure 1.3: Electron diagram of the energy shift between spin-up and spin-down states of the isolated Mn acceptor level (top) and of the top of the valence band in the many-Mn system (bottom) resulting from *p-d* hybridization (after Jungwirth *et al.*)This electronic hybridization process is the origin of the antiferromagnetic coupling between the valence band states and the Mn local magnetic moments.

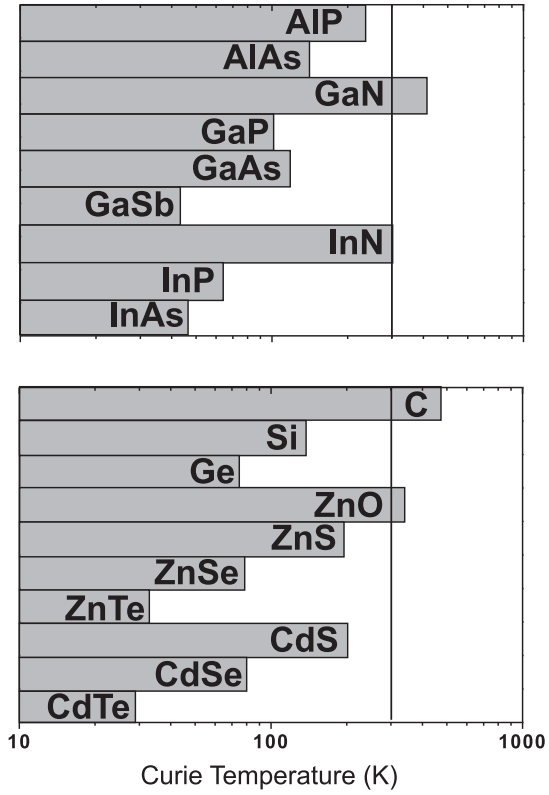

Figure 1.4: Predicted Curie temperatures for different Mn doped III-V, group IV and II-VI semiconductor compounds for a 5% Mn concentration (after Dietl *et al.*).

coupling between Mn spins emerging from *p-d* hybridization in GaMnAs was first given by Jungwirth *et al.* [39] and is presented as a summary in Fig.1.3.

In the following, a more phenomenological analysis of Dietl's theory will be presented where the predicted Curie temperature tendencies will be discussed in detail. As mentioned earlier in this paragraph this theory predicts that Curie temperatures as high as room temperature could be achieved in materials built up from light elements such as GaN, Zn or C as shown in the diagram of Fig 1.4 from Ref. [35]. Unfortunately none of these materials has reached the predicted high ferromagnetic transition temperatures partially due to experimental difficulties in achieving high doping levels. On the other hand, even in compounds such as GaN where the Mn solubility is higher than in (Ga,Mn)As, which could allow for a higher Mn incorpora-

tion, the high Curie temperatures remain elusive. In the case of (Ga,Mn)N the valence band edge and the Mn d levels are much farther apart than in (Ga,Mn)As. This makes a substantial difference since in (Ga,Mn)As the Mn d states strongly hybridize with the valence band levels [40]. Moreover, the change in the ionicity of the host crystal can also affect the electronic and magnetic state of the Mn centers for example by inducing a transition from a Mn^{2+} ($3d^5$) trivalent acceptor to a Mn^{3+} ($3d^4$) neutral impurity [41, 42]. The overestimation of the ferromagnetic interaction in these compounds is a result of not taking into account such effects that may play a role for certain materials.

1.2.3 Magnetic anisotropy

The magnetic anisotropy is strongly related to the interaction between the orbital and spin degrees of freedom of the electrons involved in the magnetic coupling. In (Ga,Mn)As these electrons are in the d^5 configuration where the orbital momentum averages to zero and no effects due to spin-orbit coupling are to be expected. However, (Ga,Mn)As has shown to have a strong magnetic anisotropy. Here the origin of the magnetic anisotropy lies in the remaining ingredient for the magnetic coupling in (Ga,Mn)As, the hole carriers. These electric charge carriers that mediate the ferromagnetic coupling have a nonzero orbital momentum and give rise to the spin-orbit interaction responsible for the magnetic anisotropy in this material [35].

The behaviour of the magnetic anisotropy in (Ga,Mn)As is also taken into account in Dietl's theory where it is found to be not only sensitive to the concentration of the charge carriers but also to the lattice strain. Fig. 1.5 shows the dependence of the anisotropy field (H_{un}) on the biaxial strain in (Ga,Mn)As for two different hole carrier concentrations simulated by Dietl's theory. The anisotropy field H_{un} is the field needed to saturate the magnetization along the hard axis and shows to be strongly dependent on strain. In particular, the biaxial strain present in GaMnAs that is namely a stress developed in two directions along the surface of the crystal, shows a transition from an in-plane to an out-of-plane easy axis as the strain increases. The notation [100]→ [001] indicates that the easy axis is along the [100] direction and that the anisotropy field H_{un} is applied along the [001] direction. As shown in the calculation in Fig. 1.5 this theory also reflects the dependence of the critical strain value needed for this transition on the carrier density in the material. The theory also predicts that such a change from in-plane to out-of-plane in the magnetic anisotropy can occur even when the layers are under a constant strain. This has been achieved in the low carrier density regime of compressively strained (Ga,Mn)As films [43] proving that the in-

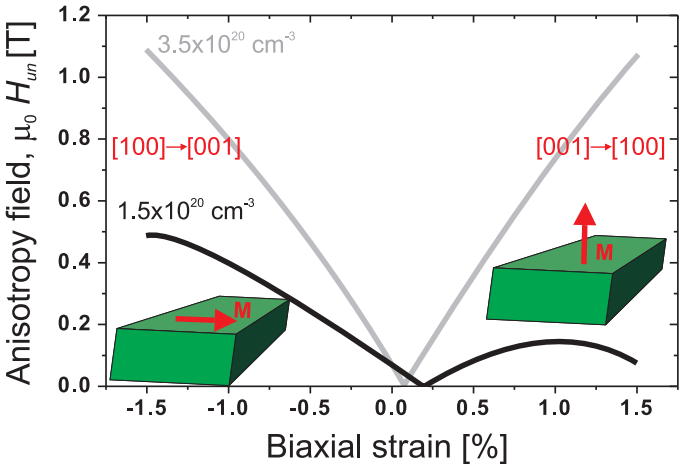

Figure 1.5: Calculated anisotropy field dependence on the biaxial strain for carrier concentrations of 3.5x10^{20} cm^{-3} and 1.5x10^{20} cm^{-3}. With increasing biaxial strain a transition from in-plane to out-of-plane easy axis can be observed (after Dietl *et al.*). The notation [100]→ [001] indicates that the easy axis is along the [100] direction and that the anisotropy field H_{un} is applied along the hard [001] direction.

plane to out-of-plane anisotropy change is sensitive to both strain and carrier concentration independently.

Experimentally, the strain dependence of the magnetic anisotropy has been most widely exploited by selecting the buffer layer on which the (Ga,Mn)As films are grown. The most widely used buffer layer materials that provide a considerable tensile strain and an out-of-plane easy axis are GaInAs or GaAlAs. In these cases the strain goes from compressive for the case of pure GaAs buffer layers (easy axis in-plane) to tensile (easy axis out-of-plane) as the concentration of the In or Al dopants increases [9, 45–47]. In addition to this epitaxial growth induced strain, the magnetic anisotropy in (Ga,Mn)As has been shown to be susceptible to externally applied strain such as in the case of GaMnAs/piezoelectric actuator hybrid structures [49, 50] and in volatile ferroelectric gating devices [48]. These devices have allowed for the detailed study of the influence of strain in the magnetic anisotropy and are model systems for the investigation of strain assisted magnetization dynamics.

Apart from the striking anisotropy changes from in-plane to out-of-plane induced by strain or carrier density modulation compressively strained (Ga,Mn)As/GaAs systems present a complex in-plane anisotropy that is at the center of the

studies presented in this thesis and will be described in detail in the following.

The in-plane magnetic anisotropy in (Ga,Mn)As has two main contributions, namely, a biaxial and an uniaxial anisotropy component [51]. It is widely accepted that the biaxial component is of crystalline origin reflecting the cubic zincblende structure of the host material. As discussed, in (Ga,Mn)As this anisotropy contribution is related to spin-orbit effects in the valence band [52] as already introduced and determines the easy axes character of the [100] and [010] cubic crystalline directions. The other anisotropy contribution is an uniaxial component that sets an easy axis along one of the cubic hard axes, namely [110] or [1$\bar{1}$0]. Unlike the biaxial anisotropy the origin of the uniaxial component has not been yet fully identified. It has been related to a surface reconstruction induced preferential Mn incorporation at every monolayer growth step [53] but also to a lowering of symmetry due to an anisotropic GaAs surface reconstruction during the growth [43]. Other theories even suggest that (Ga,Mn)As is formed by a combination of a matrix with biaxial anisotropy and an assembly of enclosed magnetic clusters with uniaxial anisotropy each having the matrix and the cluster assembly different ferromagnetic transition temperatures, respectively [44]. Despite the fact that all these theories seem reasonable and have contributed greatly to the understanding of various experimental results, the final word on the nature and origin of this anisotropy component is still under debate.

In view of these two contributions to the in-plane magnetic anisotropy in (Ga,Mn)As the expression for the energy density of a single domain magnet can be expressed in the following way [54]:

$$E = \frac{K_c}{4}\sin^2(2\varphi) - K_u\sin^2(\varphi - 135^\circ) - MH\cos(\varphi - \varphi_H) \tag{1.1}$$

where K_c and K_u are the biaxial (easy axes along the [100] and [010] directions) and uniaxial (easy axis along the [110] direction) anisotropy constants, M is the magnetization in the plane, H the magnetic field, and φ and φ_H are the angles of M and H with the [100] direction. In the absence of a magnetic field the interplay between the two anisotropy components can be clearly evaluated. In the case of a pure biaxial anisotropy (K_u=0) the energy minima are located along the cubic easy axis directions [100] and [010]. However, when the uniaxial term starts playing a role, the energy density for M oriented along the [110] direction starts decreasing and goes from a cubic hard axis to a uniaxial easy axis direction as the ratio K_c/K_u decreases. In addition to this, the energy minima shift from the biaxial cubic directions towards the [110] axis up to the limit of a full uniaxial anisotropy configuration. These magnetic anisotropy transitions as a function of the uniaxial

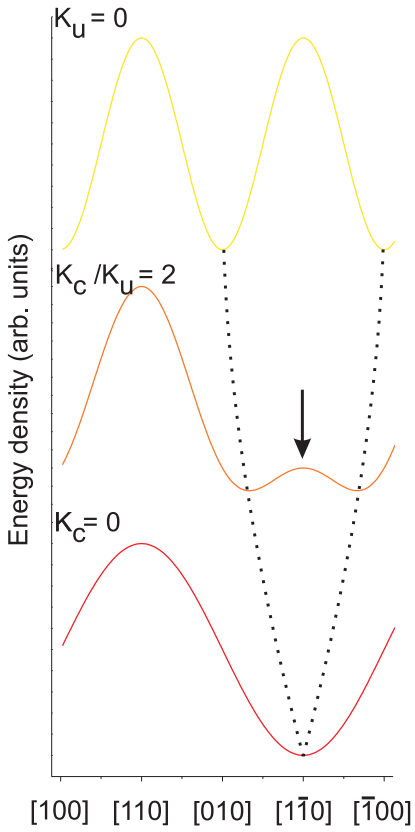

Figure 1.6: Energy density at zero field for the case of pure biaxial anisotropy (K_u=0), a mixed biaxial and uniaxial anisotropy state with K_c/K_u=2 and a pure uniaxial anisotropy case (K_c=0).

anisotropy contribution are summarized in Fig. 1.6 where the energy landscapes are given for the case of K_u=0, K_c/K_u=2 and K_c=0.
The most interesting aspect of the in-plane magnetic anisotropy contributions in (Ga,Mn)As is the possibility of changing from a biaxial to a uniaxial state by changing the temperature of the system. This biaxial-to-uniaxial transition has been widely observed in experiments and is a consequence of the different temperature dependencies of the anisotropy constants K_c and K_u [55,56]. The anisotropy constants do not depend directly on the temperature but follow power laws on the value of the magnetization which decreases as the temperature is increased. The corresponding dependences according to theory [57] are $K_c \propto M^4$ and $K_u \propto M^2$ and have been also found experimentally [56]. In view of these facts, the magnetocrystalline anisotropy constant will hold the largest values at low temperatures when M is maximum but will also be expected to decay rapidly as the temperature increases. Since the uniaxial anisotropy constant decreases only as the cube of the magnetization it can be expected, provided that K_c dominates at low temperatures, that at a critical value of M (or the temperature) both constants will hold the same value and eventually the uniaxial anisotropy component will start dominating the energy landscape. At the temperature where the crossing point occurs not only changes in the coercive fields along the in-plane directions can be observed but also striking changes in the magnetic domain wall dynamics as will be discussed in detail in chapter 3.
It is interesting at this point to recall the theory proposed by *Hamaya et al.* [44] already introduced in this section based on the coexistence of mixed magnetic phases in (Ga,Mn)As. This alternative theory explains the temperature variation of the magnetic anisotropy not in terms of the temperature dependence of the anisotropy constants but by assuming that a matrix with cubic uniaxial anisotropy has a lower ferromagnetic-to-paramagnetic transition temperature than an ensemble of clusters with uniaxial anisotropy located inside the matrix. Also this description is in good agreement with the experimentally observed gradual transition between a biaxial to uniaxial anisotropy and with the mixed anisotropy states found close to the biaxial-to-uniaxial transition temperature.
The disparity between these two interpretations accounting for the temperature dependence of the magnetic anisotropy is summarized in the cartoon in Fig. 1.7. In this picture it is shown that after applying a small magnetizing field in a certain direction the average magnetization projection on the direction of the external field is the same for both models. These models seem to be in accordance with the experimental results regarding the mixed biaxial-uniaxial anisotropy in (Ga,Mn)As. Thus, the theory accounting for the magnetization dynamics in (Ga,Mn)As needs further development and is

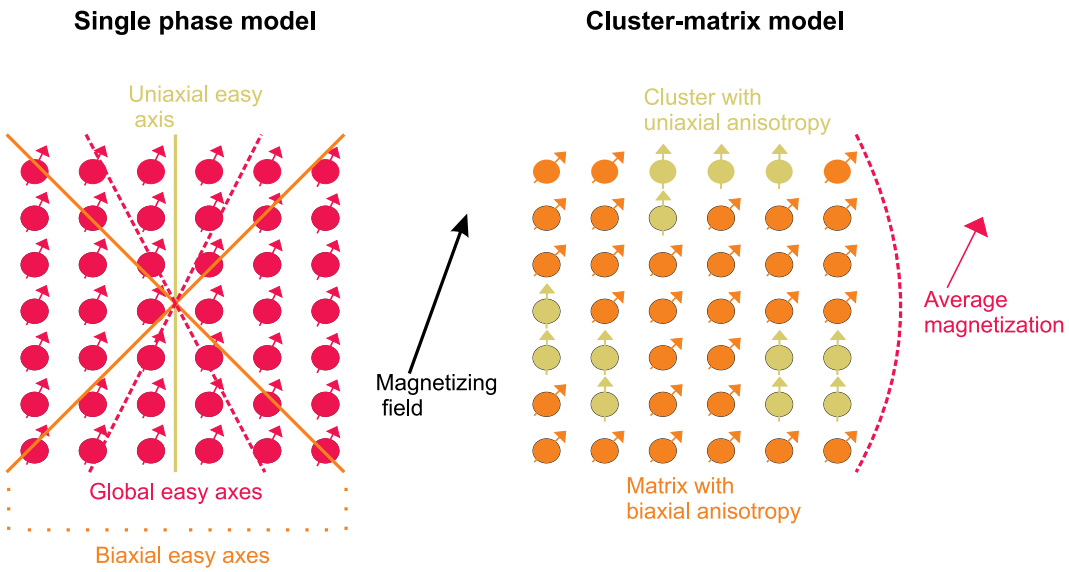

Figure 1.7: Sketch of the single phase and the cluster-matrix model. After magnetizing the average projection of the magnetization on the direction of the applied field is the same in both cases despite the different proposed local arrangement of the magnetic moments.

still a subject of intense debate in the scientific community.

1.3 Magnetic domains and domain walls

In this section the basic physics of magnetic domains and domain walls will be given. Different domain wall structures and the driving force for the formation of magnetic domains will be introduced in order to provide a background for the results that will be presented in chapter 3. Magnetic domain imaging techniques will not be discussed in this part of the thesis as a special section will be dedicated to the Kerr microscopy set-up used in this work in chapter 2.

1.3.1 The origin of magnetic domains

To begin with a discussion on the origin of ferromagnetic domains it is necessary to move one step back and recall the fundamental basis of ferromagnetism.
The first satisfactory explanation for the stronger tendency of elementary moments to align in a ferromagnet with respect to the moments in a para-

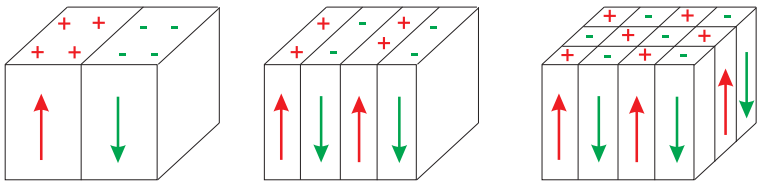

Figure 1.8: Reduction of the demagnetizing fields or "free poles" by subdivision of the magnetic domains at the expense of a considerable domain wall energy cost.

magnet was given by Pierre Weiss in 1907 [58]. In this theory a so called "molecular field", an analog to the "internal pressure" in the van der Waals theory of the condensation of gases, was introduced in order to model the overall effect of the magnetic interaction. This theory proved to be generally successful in modeling experimental results such as the temperature dependence of the saturation magnetization. This pioneering concept of a "molecular field" was later further developed into a quantum mechanical formulation by Heisenberg known as the exchange interaction [59].
Within the framework of Weiss' theory the fact that ferromagnetic materials can be spontaneously magnetized even in the absence of an external magnetic field is well accounted for, but this theory in itself could not give an explanation to the common fact of finding the majority of the ferromagnetic materials in a zero average magnetization state. This difficulty was overcome by Weiss by considering the magnetization vector as being only fixed in its magnitude while its direction remains as a variable. In this way a case such as the non-magnetic state of a ferromagnetic material like iron at room temperature (far below the ferromagnetic transition temperature) could be explained by considering that the magnetization vectors in different parts of the magnetic sample are magnetized in opposite directions and in average cancel one another. It is worth mentioning that this first notion of ferromagnetic domains presented by Weiss had not been supported by any experimental observation. The first experimental confirmation of the magnetic domain concept was provided more that ten years later by Barkhausen [101], therefore, as often stated in the literature, ferromagnetic domains are a discovery of theory [61, 62].

In order to continue with the development of domain theory and reach a general description of the static magnetization state problem further important parameters still had to be incorporated in the description, that is the so called magnetostatic energy or the stray field energy. When a magnetized sample has surfaces through which flux lines emerge with a normal component, so-called "free poles" exist at the end of these surfaces. A mag-

netic field emanates from the north poles and terminates at the south poles. Depending on the shape of the sample, the closing path of least energy for part of this dipole field, namely the shortest distance connecting these poles with opposite polarity, is through the sample. To the extent that this field passes through the sample, it opposes the magnetization that set up the surface poles in the first place. The magnetic pole strength per unit surface area σ is given by the component of the magnetization that is normal to the surface: $\sigma = \mathbf{M} \cdot \mathbf{n}$ where $\boldsymbol{n}$ is a unit vector normal to the surface. The surface pole density gives rise to a magnetic field on both sides of a surface. The $\boldsymbol{H}$ field lines emanate from the north poles (positive charges) and terminate on the south poles (negative charges). The field of the surface poles that passes through the interior of the sample is called the demagnetizing field [66]. Any finite specimen uniformly magnetized in one direction is subject to a demagnetizing field which can attain considerable values. This field can even be larger than that required to overcome any magnetocristalline effect that might be holding the magnetization in its original direction. Under these conditions, the original uniformly magnetized state becomes clearly unstable unless a large external magnetic field is applied. As mentioned, the demagnetizing fields can be also seen as the result of the abrupt change of the magnetization from a finite value M to zero at the end of the specimen generating fictitious "free poles" on the surface. A straightforward way of reducing the number of "free poles" and stabilizing the system would be to further subdivide the domains into a great number of areas of alternating pole signs as schematized in Fig.1.8 [63]. However, creating more and more domains is eventually energetically unfavorable since energy is needed for the formation of domain walls as it will be discussed in the following section.
This problem was successfully addressed in the magnetic domain theory by Landau and Lifshitz [64]. Their approach proposed avoiding the stray field energy by adopting a flux-closure type of domain arrangement as shown in Fig.1.9. This domain configuration was the result of a variational calculation method which minimizes the total energy of the system. The largest contribution to this reduction in the overall energy in this case comes from avoiding the stray field energy. What is most important about the contribution to domain wall theory from Landau and Lifshitz is the fact that the system can reach its minimum energy state not only by taking into account the magnetic anisotropy to define the magnetization direction but also by adopting a suitable arrangement of the magnetic domains. In this way they proved for the first time that a flux-closure domain pattern has a lower energy than the uniformly magnetized state and therefore is preferred by the magnetic system
As often in research, the initial simple model of Landau and Lifshitz soon

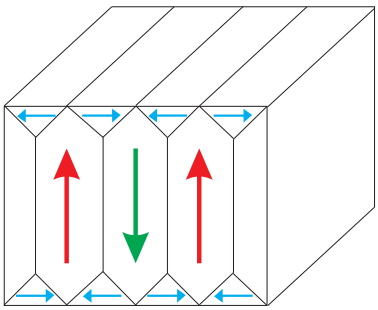

Figure 1.9: Minimal demagnetization energy domain structure (flux-closure domains) as first proposed by *Landau* and *Lifshitz*.

proved not extensive enough to describe all ferromagnetic systems especially due to their differences in magnetic anisotropies. Intensive research activity followed in order to explain various experimental observations such as the differences between domain patterns in uniaxial and cubic crystals. However, the initial contribution made by Landau and Lifshitz was enormous and served as a starting point for a series of pioneering studies in the field of magnetic domains. They provided the general and solid explanation that was needed for the understanding of the origin of magnetic domains in ferromagnetic materials.

1.3.2 Structure and energy of domain walls

As mentioned in the previous section, it is necessary to break up the ferromagnet into magnetic domains of opposite magnetization directions in order to attain a minimum energy state. It is now left to describe the internal structure of the domain boundaries.

The presence of a boundary between domains implies the rotation of the magnetization vector within the so-called domain wall. To be stable, this rotation of the spins has to find the right compromise between two distinct energy contributions, namely, the exchange energy and the magnetocrystalline anisotropy. The exchange energy contribution tries to keep all the spins aligned and therefore tends to reduce the rotation angle between two adjacent moments by spreading the width of the boundary. On the other hand, the magnetocrystalline anisotropy term tries to keep all the spins aligned along the direction of the easy axis. This contribution counteracts the effect of the exchange energy and tends to minimize the width of the boundary in which the spin direction is deviating from the easy axis direction. The schematic of the structures of two hypothetical 180° domain walls are presented in

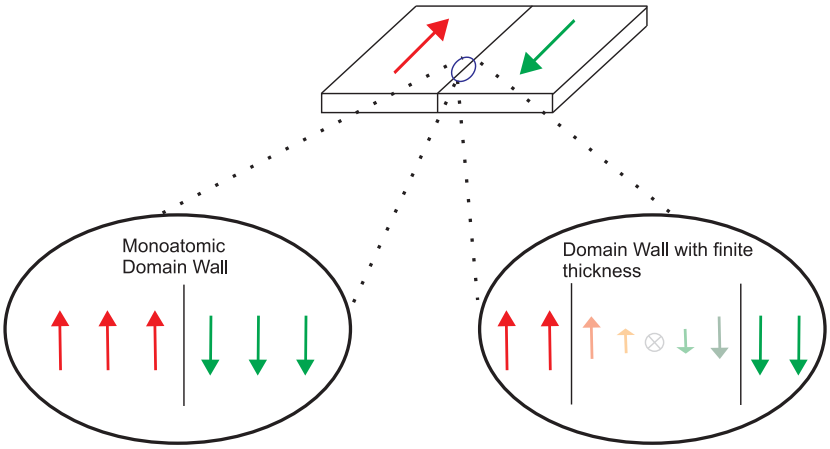

Figure 1.10: Schematic of the hypothetical structure of a 180° domain wall as a monoatomic boundary and with a finite domain wall thickness.

Fig.1.10. One is fully dominated by the magnetocrystalline anisotropy (left) presenting a sharp monoatomic transition, the other is a more realistic structure that considers also the exchange energy and presents a finite thickness. The structure of a magnetic domain wall represents a balance between the exchange effects which tend to produce a wide wall and the anisotropy forces which tend to produce a thin wall. To illustrate this more quantitatively it is worth looking at the expression of the width of a 180° domain wall for the case of uniaxial materials: $\delta = \pi\sqrt{\frac{A}{K}}$, where δ is the domain wall width, A is the exchange constant and K is the magnetocrystalline anisotropy constant [61,62,65,66]. The value of A is susceptible to the crystalline structure of the material and it is also proportional to the exchange integral J which in turn has a linear dependence on the Curie temperature [67]. Provided that the value of A is similar for two different magnetic materials the domain wall width will be determined by the magnetic anisotropy energy. Thus, the wall thickness can be of the order of 0.2 μm in systems with small anisotropy such as in soft magnetic materials and be as small as 10 nm in high anisotropy systems like permanent magnets [66].
It is important to mention at this point that the simplest case of a continuous 180° spin rotation inside the domain boundary is by no means the only possible scenario. Domain walls of reduced angle such as 90° or even more exotic like 120° and 60° are often found. In fact, most of the domain wall dynamics studies in this work have been performed on such types of reduced angle domain walls in (Ga,Mn)As. This topic will be discussed in detail in chapter 3.

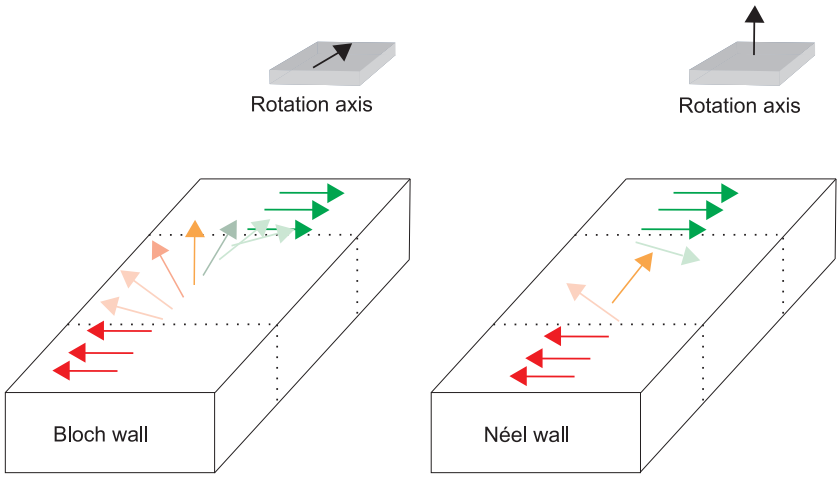

Figure 1.11: Illustration of the internal spin arrangement inside Néel and Bloch walls.

In addition to the possibility of a spin rotation of less than 180° inside the domain boundaries there is another fundamental parameter characterizing magnetic domain walls and that is the direction of the spin rotation axis with respect to the sample surface. The most simple cases are the so called Néel and Bloch walls. In the first case the spin rotation inside the wall occurs within the plane of the sample surface while in the case of Bloch walls the transition is accompanied by the alignment of the spins in a plane that is perpendicular to the surface. The structure of Bloch and Néel walls are illustrated in Fig.1.11 left and right, respectively.

Interesting results are obtained when modeling domain walls in thin films if the magnetostatic energy is taken into account. It is found that the Bloch wall energy density increases with decreasing film thickness because of the increased magnetostatic energy due to the appearance of "free poles" on the surfaces above and below the wall. On the other hand, the Néel wall energy decreases with decreasing film thickness because it is proportional to the area of the charged surfaces inside the film. In this way, a transition from a Bloch wall structure to a Néel wall is expected to occur as the thickness of the film decreases.

As the final remarks of this section it is good to mention that not only these two simple domain boundary structures are to be found in ferromagnetic materials. Much more complex structures can also be adopted to minimize the magnetostatic energy as the structure, dimensions and magnetic anisotropy of the material are changed. As an example the so-called cross-tie walls can be mentioned. In this case the boundary is a composite wall that can be

found in replacement of a 180° Néel wall. Occasionally the cross-tie walls are energetically favourable compared to the 180° Néel walls and consist of a spin substructure that is mainly formed by a combination of several 90° transitions.
Another variable relevant for the domain wall structure is given by the possibility of taking one or the opposite sense for the rotation of the spins inside the domain wall. This gives rise to domain wall chirality which is a parameter of great importance when analyzing the interaction between neighbouring domain walls. The sense of rotation combined with the type of wall (Néel or Bloch walls) can determine either an attractive or a repulsive interaction between two adjacent domain walls. In addition, the sense of rotation inside the domain wall can also be found to vary along the length of the wall, in this way giving rise to substructures inside the boundary. This case may appear when the two possible rotation senses of the spins in the domain walls have the same energy and therefore are equally likely to occur. In this case, both modes can coexist in the same wall divided by lines between the different rotation senses called Bloch lines. These Bloch lines can move within the wall and influence the wall motion in a drastic way interacting strongly with pinning centers.
As stated previously, many other interesting aspects about magnetic domain walls could be included in a more extensive recount, however, only the most basic concepts necessary for the understanding of the work in this thesis have been discussed.

Chapter 2

Experimental Methods

In this chapter the experimental techniques that were most extensively used will be presented. These experimental tools are low temperature magneto-optical Kerr microscopy and magneto-transport. In both cases a detailed description of the experimental set-up together with a recount of the basic physical concepts behind the measurement techniques will be given.

2.1 Kerr microscopy

Kerr microscopy together with Faraday microscopy are the two most prominent techniques for the observation of magnetic domains. For decades they have been widely used for both the time and space resolved study of magnetization dynamics in magnetic materials. In the case of Faraday microscopy the magnetic contrast necessary for distinguishing magnetic domains with different orientation of the magnetization is obtained by light transmission thought the magnetic material. On the other hand, Kerr microscopy provides magnetic information by evaluating the light that is reflected from the sample. The Faraday effect can be rarely applied since few magnetic samples are transparent while the Kerr effect detection in microscopy is a very powerful tool for imaging the domain structure in a much wider variety of materials.
One of the main advantages of magneto-optical techniques and in particular Kerr microscopy is that it allows to monitor the magnetization dynamics without influencing the magnetization during the observation time as the heating effect of the illumination is negligible. In addition, it is a non-destructive technique which leaves samples intact after the measurements and consequently allows for a simultaneous analysis with other experimental methods. However, there are also disadvantages like the limitation in

the spacial resolution. This restriction limits the accurate observation of the magnetic processes typically to domains larger than 0.15 μm corresponding to an optical resolution of approximately 0.3 μm.
In the following the basics and most important concepts of the magneto-optical Kerr effect is introduced. In a second part of this section the low temperature Kerr microscopy set-up used for the collection of the data presented in this thesis is described in detail.

2.1.1 Magneto-optical Kerr effect

The interaction of a beam of linearly polarized light with a magnetized medium can lead to changes in the polarization state of light. These changes can be usefully detected to study time resolved magnetization dynamics and to reveal the magnetic domain structure in magnetic materials. In particular, the magneto-optical Kerr effect manifests itself as the change in polarization of incident linearly polarized light to elliptically polarized light on reflection at a magnetized surface [63].
To understand this effect better, it is useful to go one step back and analyze the interaction between linearly polarized light and a non-magnetic material. In this case, it is possible that the light reflected from the surface is also linearly polarized. This can occur when the light polarization direction lies in or perpendicular to the plane of incidence. If the surface is magnetized, the reflected beam emerges elliptically polarized even when the incident beam is polarized parallel or perpendicular to the plane of incidence. In this case the magnetization of the sample gives rise to an additional light vibration component, called the Kerr component, perpendicular to the incident light vibration. This Kerr component added to the original vibration of the incident beam is responsible for the elipticity in the polarization of the reflected light. It is worth mentioning that the magnitude of this rotation of the polarization is rather small, and moreover, much smaller in general than the rotation produced by the Faraday effect in transmission systems [68].
The dependence of the Kerr and Faraday effect on the direction of magnetization can be rigorously derived from Maxwell's equations. However, the solutions can also be described by rather simple arguments using the concept of a Lorentz force acting on light-agitated electrons. As an illustrative example [61], let us assume the magnetization vector to be oriented perpendicular to the surface. In this case a linearly polarized light beam will induce electrons to oscillate parallel to its plane of polarization, the plane of the electric field $\boldsymbol{E}$ of the light. As previously introduced, in some cases the reflected light can be polarized in the same plane as the incident light. Let us call this the regular component ($\boldsymbol{R}_N$) of the emerging light. Additionally, the

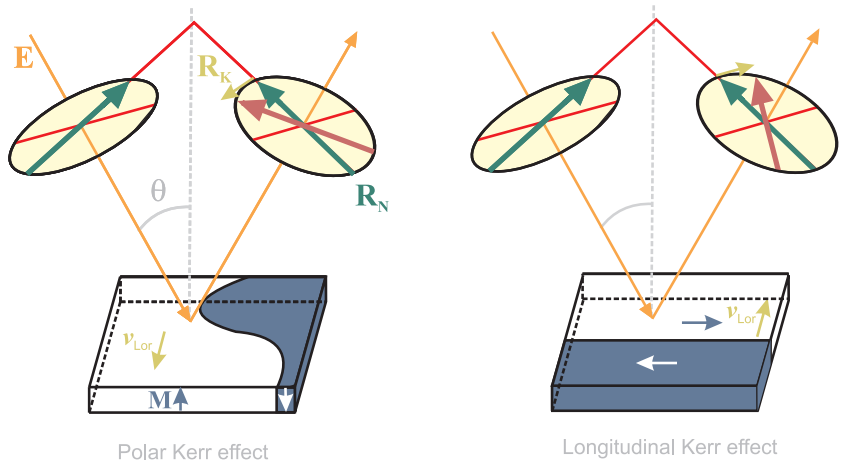

Figure 2.1: Schematics of the orientation of the magnetization ($\boldsymbol{M}$) with respect to the plane of incidence and the plane of the surface for the polar (left) and longitudinal (right) Kerr effect. $\boldsymbol{R}_N$ is the regularly reflected electric field ($\boldsymbol{E}$) amplitude and the Kerr amplitude $\boldsymbol{R}_K$ can be thought as generated by the Lorentz motion $\boldsymbol{v}_{Lor}$.

Lorentz force arising in a magnetic material induces a small component of vibrational motion perpendicular to the primary motion and to the direction of magnetization. This secondary motion is proportional to the magnitude and the orientation of the electric field $\boldsymbol{E}$ with respect to the direction of the magnetization: $\boldsymbol{v}_{Lor} = -\boldsymbol{m} \times \boldsymbol{E}$ being $\boldsymbol{m} = \boldsymbol{M}/M_s$ (M_s = saturation magnetization) the direction of magnetization. As previously discussed, this generates secondary amplitudes: the Faraday amplitude $\boldsymbol{R}_F$ for transmission and the Kerr amplitude $\boldsymbol{R}_K$ for reflection. The superposition of the amplitude of the regular component of the reflected light $\boldsymbol{R}_N$ with either the Faraday or the Kerr amplitudes $\boldsymbol{R}_F$ and $\boldsymbol{R}_K$ leads to magnetization-dependent polarizations.
In particular, the Kerr effect can be observed in three different forms depending on which one of the three possible orientation the magnetization vector adopts with respect to the plane of incidence and the plane of the reflecting surface. These three possibilities are named *Polar*, *Longitudinal* and *Transverse* effects.

- *Polar effect.*
  In this case the magnetization vector lies along the axis perpendicular to the plane of the reflecting surface as shown in Fig 2.1. This arrangement produces the greatest rotation of the plane of polarization, which is usually of the order of 20 minutes of arc. In addition, it is the only effect

that is non-zero at normal incidence. This light incidence arrangement ($\theta = 0°$) is actually where the effect is expected to be strongest. In the $\theta = 0°$ configuration, the rotation in the plane of polarization of the incident light is by symmetry the same for all polarization directions of the incident beam chosen parallel to the plane of incidence.

- *Longitudinal effect.*
  For the longitudinal effect the magnetization lies in the plane of incidence and also in the plane of the reflecting surface. The light beam has to be inclined relative to the surface. It yields a magneto-optical rotation both for parallel and perpendicular polarization with respect to the plane of incidence, only the sense of rotation is opposite in the two cases. The rotation produced by this effect is considerably less, typically a factor of five smaller, than that of the polar effect and also varies with the angle of incidence. The Lorentz force is found to be zero at normal incidence or points along the beam thus not generating a detectable rotation. The maximum rotation is achieved for angles of incidence close to 60°.

- *Transverse effect.*
  In the transverse configuration the magnetization is again in the plane of the reflecting surface but is perpendicular to the plane of incidence. Interestingly, from the three arrangements the transverse is the only one that shows no magneto-optical effect in transmission since the Lorentz motion is either zero or points along the propagation direction. However, in reflection, light of parallel polarization will generate a Kerr amplitude but the polarization direction is the same as that of the regularly reflected beam. The transverse effect therefore causes an amplitude variation of the light that can be measured but it will produce little contrast in a visible image. To generate a detectable rotation in the transverse case, the polarization of the incident beam is chosen between the parallel and perpendicular orientations. In this way, the perpendicular component is not affected while the parallel component is modulated in its amplitude leading to a detectable polarization rotation.

In Fig. 2.2 the longitudinal effect for perpendicular polarization with respect to the plane of incidence and the transverse effect are schematized. Note the change in sign in the Lorentz motion with respect to the longitudinal effect with parallel polarization shown in Fig. 2.1.
All these effects can be combined in a quantitative way by a general formula for the Kerr effect. In this model, the light passes first through a polarizer

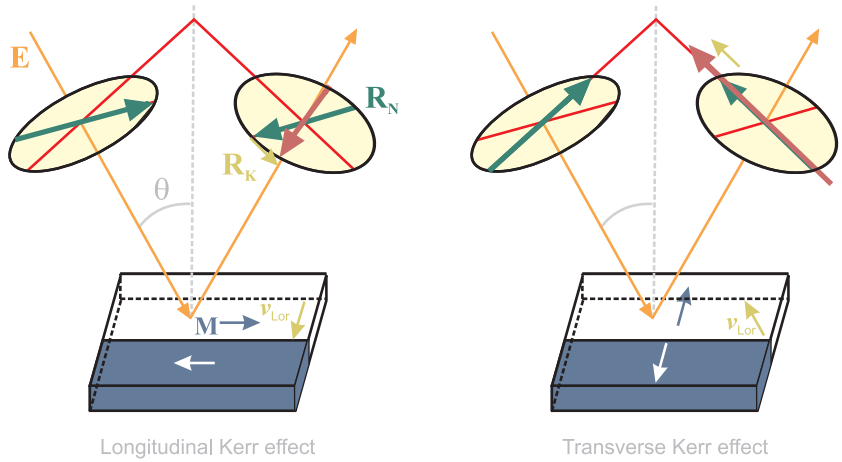

Figure 2.2: Diagram of the longitudinal Kerr effect with perpendicular polarization (left) and the transverse Kerr effect (right). The magnitude of the longitudinal effect is the same as in Fig 2.1 but of opposite sign. In the transverse configuration only parallel polarization yields an effect and only in reflection.

of setting ψ_p measured from the plane of incidence as indicated in Fig. 2.3. Then it is reflected from the surface of the sample, experiencing regular amplitude reflection coefficients R_p and R_s for the components parallel and perpendicular to the plane of incidence. The Kerr amplitudes ${R_K}^{pol}$, ${R_K}^{lon}$ and ${R_K}^{tra}$ for the polar, the longitudinal and the transverse cases are excited, depending on the magnetization components m_{pol}, m_{lon} and m_{tra}. Finally the light passes through an analyzer with the setting α_s measured from the axis perpendicular to the plane of incidence, leading to the total signal amplitude that has the following form [61]:

$$\begin{aligned} A_{tot} = &-R_p \cos\psi_p \sin\alpha_s + R_s \sin\psi_p \cos\alpha_s + R_K^{pol} \cos(\alpha_s - \psi_p) m_{pol} \\ &+ R_K^{lon} \cos(\alpha_s + \psi_p) m_{lon} - R_K^{tra} \cos\psi_p \sin\alpha_s m_{tra}. \end{aligned} \tag{2.1}$$

The regular reflection coefficients R_p and R_s can be derived from the optical constants and the angle of incidence. Only small values of α_s and ψ_p are needed to adjust the polar and longitudinal effects for optimum contrast. The transfer effects yield the largest modulation in the amplitude A_{tot} after the analyzer if $\alpha_s \approx \psi_p \approx 45°$, provided that the two regularly reflected amplitudes R_p and R_s are about equal.

A simplified expression for the absolute values of the Kerr amplitudes ${R_K}^{pol}$, ${R_K}^{lon}$ and ${R_K}^{tra}$ involved in the expression of A_{tot} (Eq. 2.1) can be derived

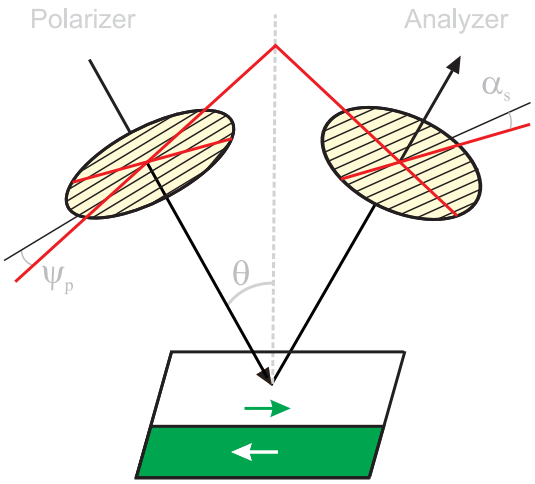

Figure 2.3: Schematics of the general arrangement of the polarizer of setting ψ_p and the analizer of setting α_s in a Kerr effect detection set-up. The angles ψ_p and α_s are measured from the plane of incidence of the beam and its perpendicular, respectively.

in terms of the easily accessible regular intensity reflectivities r_p and r_s.

$$|R_K^{pol}| = (|Q_v|/4n_1)\sqrt{n_1^2 + k_1^2}\sqrt{(1 - r_s)(1 - r_p)} \tag{2.2}$$

$$|R_K^{lon}| = (|Q_v|/4n_1)n_0 \sin\theta\sqrt{(1 - r_s)(1 - r_p)} \tag{2.3}$$

$$|R_K^{tra}| = (|Q_v|/4n_1)n_0 \sin\theta(1 - r_p) \tag{2.4}$$

where n_0 is the refractive index of the environment and n_1+ik_1 is the complex refractive index of the magnetic substrate. The angle θ is the angle of incidence measured form the surface normal. From these relations it can be observed that if the regular reflectivities r_p and r_s are reduced to zero, the Kerr amplitudes R_K assume their largest values. In this way, an enhancement of the Kerr effect can be achieved by incorporating an effective dielectric anti-reflection coating for the material of interest. As an example of this Kerr effect enhancement method ZnS is commonly employed for the coating of metallic samples.

The equations 2.2, 2.3 and 2.4 also show clearly that, as it has been already qualitatively introduced, the polar Kerr effect is stronger than the other two effects. This difference is not only dependent on the angle of incidence by the factor $1/\sin\theta$, but also by the factor $\sqrt{n_1^2 + k_1^2}$ related to the refractivity of the magnetic material to be analyzed that as a consequence of Snell's

law reduces the angle of incidence inside the magnetic medium affecting the magnitude of the Kerr effect.

2.1.2 Magnetic contrast

This section is dedicated to provide some relevant theoretical considerations regarding the optimization of the magnetic contrast in Kerr microscopy [61]. For two domains with opposite magnetization, the Kerr amplitudes differ only in sign. The expression for the total amplitude given in the last section (Eq. 2.1) can be written in a more compact way. If A_N and A_K account for the regular and the Kerr amplitudecontributing to A_{tot}, respectively then A_N contains the first two terms of Eq. 2.1 and the rest of the expression is represented by A_K therefore, the expression for the total amplitude becomes A_{tot}=A_N $\pm A_K$. In this way we may define the 'Kerr rotation' as the angle φ_K=A_K/A_N which typically yields rather small values. According to what has been previously introduced we can assume in a simplified picture that in such a configuration where α_s =φ_K the light coming from one of the domains will be completely extinguished. Setting the analyzer in this fashion will result in one domain appearing dark while another domain with opposite magnetization will appear bright in comparison. A summary of the parameters involved in this discussion regarding the magneto-optical contrast are presented in the diagram in Fig. 2.4
However, rotating the analyzer beyond the extinction point (α_s =φ_K) can be of great benefit in terms of improving the magnetic contrast as will be shown in the following. If we assume that the phases of the regular and the magneto-optical amplitude are equal then the intensity of the domains observed as 'dark' (I_d) becomes relative to the incident intensity as follows:

$$I_d = A_N^2 \sin^2(\alpha_s - \varphi_K) + I_0 \cong (A_N \sin\alpha_s - A_N \cos\alpha_s)^2 + I_0 \tag{2.5}$$

where I_0 is a background intensity and φ_K=A_K/A_N as introduced above. In this way the relative intensity of the 'bright' domain becomes:

$$I_b = A_N^2 \sin^2(\alpha_s + \varphi_K) + I_0 \cong (A_N \sin\alpha_s + A_N \cos\alpha_s)^2 + I_0 \tag{2.6}$$

since the 'dark' and 'bright' domains differ only by the sign of φ_K. As follows from these expressions the relative magneto-optical signal is the difference between the two intensities:

$$s_{mo} = I_b - I_d = 2\sin(2\alpha_s) A_N A_K. \tag{2.7}$$

The magnetic contrast is, thus, a function of the Kerr amplitude A_K and therefore of the corresponding magnetization component. From this expres-

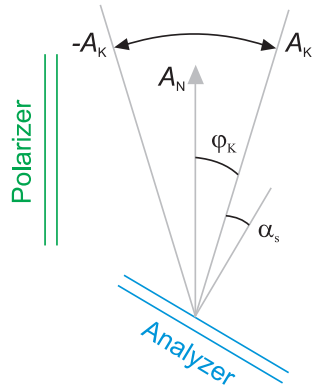

Figure 2.4: Diagram illustrating the parameters involved in the optimization of the magnetic contrast in Kerr microscopy.

sion it can be also extracted that increasing the angle α_s leads to the enhancement of the magneto-optical signal. However, the important quantity for the magneto-optical contrast is the magneto-optical signal normalized to the total signal: $C_{mo}= s_{mo}/(I_b+I_d)$. This simple expression for C_{mo} can be optimized with respect to the angle α_s to give the following results:

$$\tan \alpha_{opt}^{C} = \sqrt{\frac{A_K^2 + I_0}{A_N^2 + I_0}}, C_{opt} = \frac{A_K A_N}{\sqrt{(A_N^2 + I_0)(A_K^2 + I_0)}} \approx \frac{A_K}{\sqrt{A_K^2 + I_0}} \quad (2.8)$$

The last expression is only valid for $I_0 \ll A_N^2$. These expressions suggest that for large values of A_N the optimum contrast depends only on the background intensity and on the magneto-optical amplitude A_K and not on the regular amplitude A_N or the Kerr rotation φ_K. The contributions to the background intensity are determined by imperfect polarizers and surface imperfections among other factors.

It is important to note that the criterion of maximum contrast is a key point to be considered when thinking of magnetic domain imaging, however, it does not guarantee the best visibility of domains. As in many occasions found in experimental work, it is vital to have a good signal-to-noise ratio. In this regard potential sources of noise such as fluctuations in the light source, in the optical path, or in the sample itself can play a significant role and therefore need to be reduced to the absolute minimum to achieve good magnetic contrast.

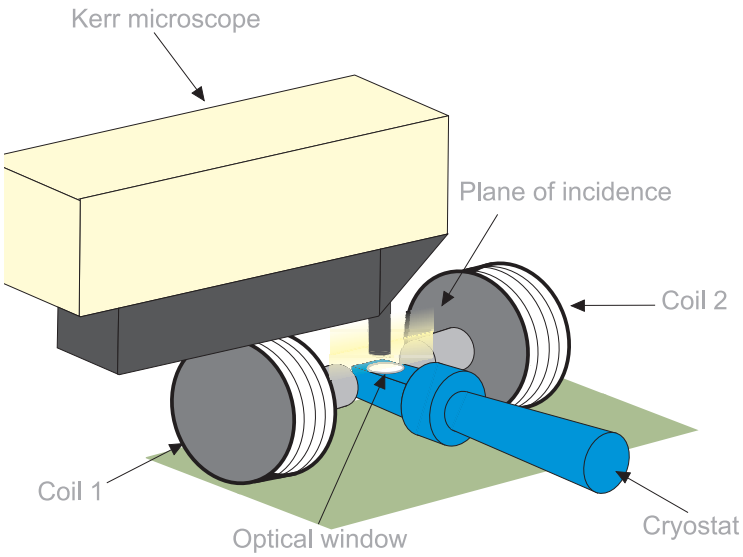

Figure 2.5: Scheme of the experimental low temperature Kerr microscopy set-up used in this work. The geometrical arrangement of the plane of incidence of the light of the microscope and the coils generating the in-plane magnetic field exploits the *Longitudinal* Kerr effect.

2.1.3 The Kerr microscope and measurement set-up

In the following technical aspects of Kerr microscopy and in particular those applying to the instrument employed in these studies will be given. At this point it is important to recall that the magnetic domain studies in this thesis where carried out on (Ga,Mn)As materials with in-plane magnetic anisotropy. Therefore, as can be understood from the previous sections the optical arrangement chosen for the measurements relies on the *Longitudinal* Kerr effect.

Since the Curie temperature of GaMnAs is below 70 Kelvin, an experimental set-up allowing for optical measurements at cryogenic temperatures is needed. In Fig. 2.5 the experimental set-up employed for the investigations presented in this work is sketched. The cryostat consists of a cold finger situated in a high vacuum environment which is cooled with liquid Helium under continuous flow conditions. Even at low temperatures of 3 Kelvin, the temperature of the sample does not differ substantially from that of the cold finger provided there is a good thermocoupling. The cold sample inside the cryostat can be optically analyzed through optical windows which allows for measurements both in reflection and in transmission. As shown in Fig. 2.5, there are two coils situated at both sides of the cryostat that can generate

an in-plane magnetic field up to 200 mT.
As mentioned previously, the *Longitudinal* Kerr effect was exploited to reveal the magnetization dynamics of (Ga,Mn)As with in-plane anisotropy. The Kerr microscope is arranged accordingly as shown in Fig. 2.5 namely, with the plane of incidence of the light beam parallel to the axis of the coils. As discussed in the previous section magnetic contrast between 'dark' and 'bright' domains is influenced by the value of the magnetization. In materials such as iron the magnetic contrast is high enough to detect domains without image processing. In the case of (Ga,Mn)As the magnetization values are much smaller and the domain pattern is not visible at a first sight. In order to reveal the domain wall dynamics an image substraction processing of the recorded data was employed. This consists in initially saturating the magnetization of the samples and saving an image detected by a CCD camera that will later be substracted from the recorded frames during the magnetization reversal process of interest. This methods proves successful for the observation of the changes in the domain pattern with respect to the saturated material. In a final step, all the substracted images are treated for contrast enhancement with the software WSxM [69] using the 'smoothing' and 'equalize' functions. This procedure has been used for the image processing of all the Kerr microscopy data shown in this work.
The longitudinal Kerr effect has not only been used for imaging of the magnetic domain walls but also for measuring magnetization loops. This has been done using the MOKE (magneto-optical Kerr effect) technique which is based on the same magneto-optical principle as Kerr microscopy but lacks of spacial resolution and is therefore, non-local. In this case the illumination source is a red diode laser beam with the same plane of incidence as the microscope. After going though a polarizer the beam is reflected on the sample surface, passes through an analyzer and is finally detected by a photomultiplier. In this case the signal obtained is not an image but the average Kerr rotation across the complete spot size of the laser (approximately 1 mm). Unlike SQUID (superconducting quantum interference device) the MOKE technique does not provide a quantitative value for the magnetization but it is of great use for the determination of coercive fields and multiple step reversals as will be presented in the upcoming chapter.

In the following the arrangement of the microscope optical components will be shortly discussed. The microscope exploits the so-called Köhler illumination method. The principle of the Köhler illumination light path is schematized in Fig. 2.6. The Köhler set up has the advantage of avoiding optical distortions without attaining negative effects on the quality and homogeneity of the light illuminating the sample which is vital for achieving magnetic contrast. The use of a Berek prism as a mirror element is par-

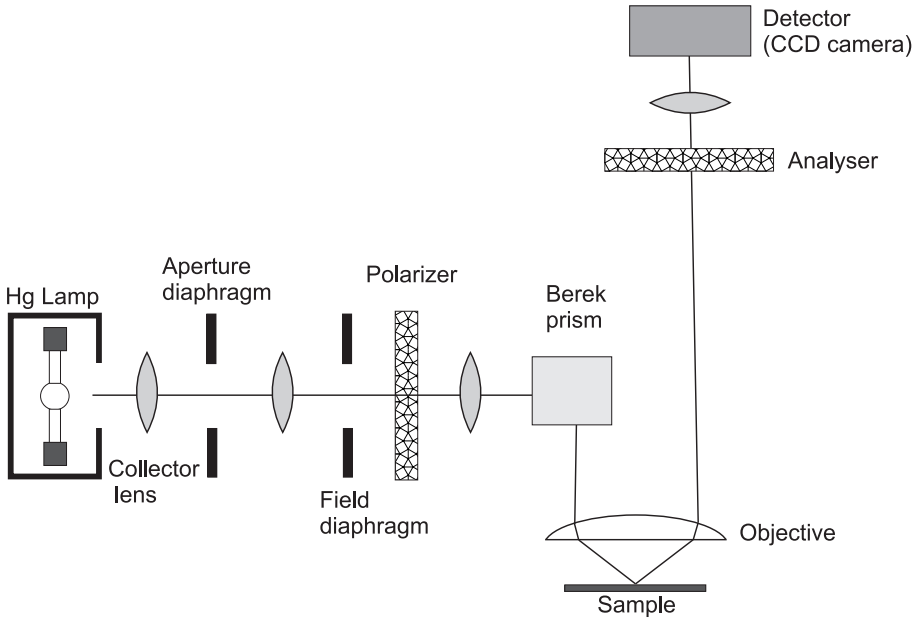

Figure 2.6: Diagram of the arrangement of the optical components for Köhler illumination inside the Kerr microscope. The light source is a Hg lamp and the detection is performed with a CCD camera.

ticularly suitable for measurements of the longitudinal effect since it causes no light loss and introduces little depolarization, however, it also restricts the resolution in one direction [61]. As for the light source a mercury lamp has been employed since it offers sufficient brightness and emits in a wide frequency range (white source), however, its stability is rather poor and its lifetime quite limited. The detection of the light reflected from the sample is done by a CCD (charged-coupled device) camera that provides both sufficient spacial and time resolution. This allows to study the magnetic relaxation as well as the anisotropic domain wall propagation as will be shown in the following chapter.

2.2 Magneto-transport

Measurements of electric charge transport in metallic and semiconducting materials is a key point for the understanding of their physical properties and even their structure. Moreover, transport under the influence of magnetic fields can lead to the observation of new effects that can be particularly

interesting when the devices are made out of magnetic materials. In addition to the interesting physics behind these magneto-transport effects, enormous technological applications have been discovered from which we benefit today such as the giant magneto-resistance [70, 71] in magnetic storage media exploiting spin dependent transport.
In this section a concise overview on the most relevant magneto-transport effects to this work will be given. Special emphasis will be put on some of the various types of Hall effects and how they are approached both from a theoretical and experimental point of view to reveal the magnetic properties of (Ga,Mn)As. At the end of this section a short comment will be given on the fabrication of the (Ga,Mn)As magneto-transport devices.

2.2.1 Ordinary and anomalous Hall effect

As an introduction to the magneto-transport effects relevant to the study of (Ga,Mn)As with in-plane anisotropy let us discuss some of the basic concepts regarding the ordinary and anomalous Hall effect. The ordinary Hall effect is a phenomenon in which a transverse electric field (E_H) appears across a sample when an applied magnetic field $\boldsymbol{H}$ has a component perpendicular to the current density $\boldsymbol{I}$:

$$\boldsymbol{E}_H = R_H(\boldsymbol{I} \times \mu_0 \boldsymbol{H}), \qquad R_H = (ne)^{-1} \tag{2.9}$$

where R_H is the Hall coefficient which describes the strength of the effect and depends on the carrier density n. This ordinary Hall effect is a result of the Lorentz force $\boldsymbol{F}=\mu_0 q(\boldsymbol{v}\times\boldsymbol{H})$ acting on the charge carriers of charge q and velocity v [66]. From these expressions it is evident that the Hall voltage will change sign according to the charge of the carriers and most importantly that the carrier density can be calculated from Hall measurements, a method widely used in the literature.
The material in which the Hall effect is observed needs not to be magnetic although the magnitude of the Hall resistivity appears to be much higher in ferromagnetic materials. This stronger effect is due to an additional contribution to the Hall resistivity that is dependent on the magnetization of the material and is called anomalous Hall effect [72]. Since the anomalous Hall effect is linearly dependent on the magnetization M we can write the complete expression for the Hall resistivity (ρ_{xy}) for ferromagnetic materials:

$$\rho_{xy} = R_H H + 4\pi R_{an} M \tag{2.10}$$

where the first term is the ordinary Hall resistivity proportional to the external field and the second term accounts for the anomalous Hall effect proportional to the magnetization M.

The anomalous Hall contribution is usually attributed to a spin-orbit coupling induced anisotropic scattering of spin up and down electrons. The scattering mechanisms involved are accounted for in the dependence of the anomalous Hall coefficient R_{an} on the longitudinal resistivity ρ_{xx}. In particular, the co-called 'skew' and 'side-jump' scattering mechanisms hold a linear and quadratic dependence of R_{an} on ρ_{xx}, respectively. However, it is also found in the literature that the dominant contribution to the anomalous Hall effect in ferromagnetic semiconductors is due to a scattering-independent component arising from the Berry phase acquired by the itinerant electrons traversing closed paths on the spin-split Fermi surface which also shows the relation $R_{an} \propto \rho_{xx}^2$ [73–76].
In the ferromagnetic semiconductor (Ga,Mn)As the contribution of the anomalous Hall resistivity to the overall Hall resistivity is large due to the participation of the charge carriers in the magnetic interaction [75]. In this way, to reliably calculate the hole density it is necessary to separate the ordinary and anomalous Hall contributions. However, the differentiation between these two components appears not to be a simple task since, as previously mentioned, the anomalous Hall coefficient R_{an} is found to depend not only on the magnetization that can be saturated with a large enough magnetic field but also on the longitudinal magnetoresistance ρ_{xx}. Under these circumstances both the ordinary and the anomalous contribution to the Hall resistivity are functions of the magnetic field making a separation between them a non-trivial matter.
In order to circumvent this problem, a very accurate procedure has been developed for the calculation of the carrier density in the presence of the anomalous Hall effect contribution in (Ga,Mn)As. In this approach, both ρ_{xy} and ρ_{xx} are measured at high magnetic fields as a function of temperature. In this way the functional form of $R_{an}(\rho_{xx})$ can be obtained. The dependence is found to follow the expression $R_{an}(\rho_{xx})^n$ where the exponent n varies between 1 and 2 and is sample dependent. Once n is known the expression for R_{an} can be used to fit ρ_{xy} versus magnetic field and determine the value of the hole density. However, accurate values can not be obtained from all types of samples and for some cases certain limitations of the method need to be taken into account. In the curves of ρ_{xx} versus field the low field part (approximately below 0.5 T) shows an initial positive magnetoresistance typical of (Ga,Mn)As with in-plane anisotropy. Beyond this regime a negative magnetoresistance is observed whose contribution decreases as the magnetic field is increased. The value of this negative magnetoresistance can be of crucial importance for the accuracy of the calculation of the hole density. Reliable results can be obtained with a negative magnetoresistance of up to 3%. The contribution of the negative magnetoresistance has been found to

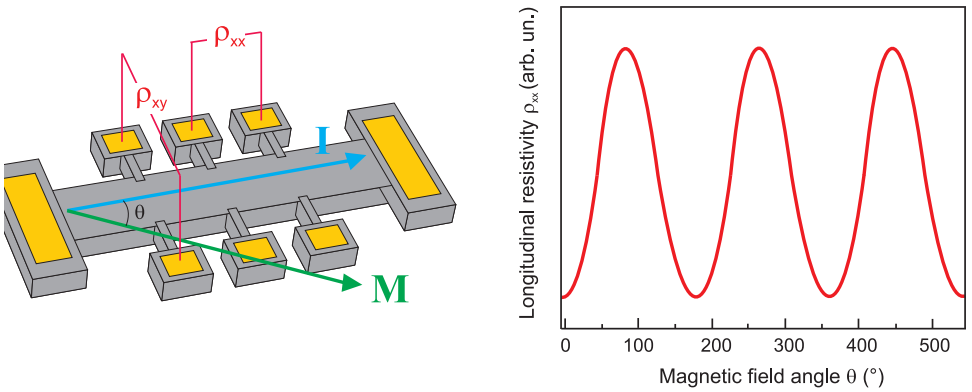

Figure 2.7: Anisotropic magnetoresistance in (Ga,Mn)As. The longitudinal resistivity (ρ_{xx}) goes from a minimum to a maximum value when the magnetic field rotates the magnetization from parallel to perpendicular directions with respect to the current.

be largest in insulating samples, therefore limiting this method to metallic samples where the negative magnetoresistance is small [76].

2.2.2 Anisotropic magnetoresistance and Planar Hall effect

The presence of the external magnetic field, as previously discussed, deflects charges from the current path due to the Hall effect and therefore increases the resistance. This so-called ordinary magnetoresistance is present in both metals and semiconductors. On the other hand, just as the Hall effect in a ferromagnet has two components dependent on the magnetic field and the magnetization, respectively, so does the magnetoresistance. This additional contribution, the anisotropic magnetoresistance, depends on the orientation of the magnetization with respect to the direction of the current and is normally much stronger than the ordinary magnetoresistance component. This is exemplified in Fig. 2.7 for (Ga,Mn)As where the resistivity perpendicular to the magnetization ($\rho_\perp$) is larger than the resistivity parallel to the magnetization ($\rho_\parallel$) [77]. The dependence of the longitudinal resistivity on the direction of the magnetization with respect to the direction of the current follows the expression:

$$\rho_{xx} = \rho_\perp - (\rho_\perp - \rho_\parallel)\cos^2(\theta) \tag{2.11}$$

as shown in the plot in Fig. 2.7. Thus, if the crystalline axis of the (Ga,Mn)As sample are known with respect to the Hall bar orientation the direction of

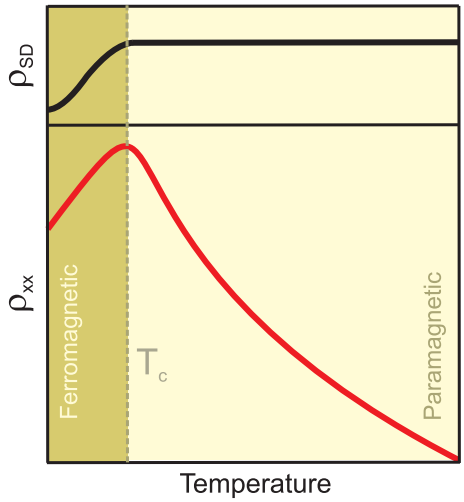

Figure 2.8: Sketch of the typical temperature dependence of the longitudinal resistivity in (Ga,Mn)As and the temperature variation of the spin-disorder scattering contribution. This last contribution allows for the identification of T_c as the maximum of the ρ_{xx} versus temperature plot.

the magnetization can be traced by analyzing the value of the resistivity as a function of the magnetic field.

The longitudinal resistivity is not only valuable when probed as a function of the magnetic field but also its temperature dependence can give very important information about the magnetic properties even in the absence of a magnetic field. The ρ_{xx} versus temperature plot typically shows a distinct peak centered at the ferromagnetic transition temperature that can be unambiguously used to measure T_c in a simple and reliable way exclusively by means of electrical transport. This peak is attributed to spin-disorder scattering. In Fig.2.8 the spin-disorder scattering contribution to the resistivity is schematized together with the typical shape of the temperature dependence of ρ_{xx} for a metallic GaMnAs sample. The spin-disorder scattering remains constant in the paramagnetic region and when going down in temperature through the ferromagnetic transition it gradually drops until the magnetic order of the spin system is completed [78]. In this way, the Curie temperature can be evaluated by monitoring the temperature dependence of the longitudinal resistivity due to the significant contribution to ρ_{xx} coming from spin-disorder scattering. This simple method for the determination of T_c will be recalled in many occasions throughout this thesis as it was employed to test the effects of various treatments on the magnetic and electrical properties of different (Ga,Mn)As samples. A more accurate procedure for

obtaining the value of the Curie temperature from resistance vs. temperature measurements involves taking the derivative of the temperature dependence of the resistance [79]. In the plot of the first derivative of the resistance vs. temperature data the Curie temperature can be observed as a clear singularity which substantially decreases the error bar for the determination of T_c. As mentioned, in the results presented in this thesis the Curie temperature values will be analyzed in a more simple way only by reading the values of the resistance peak. This approximation is made considering that in this case the focus is on the relative differences between the position of the resistance peaks before and after different treatments. Consequently, a larger error bar does not affect the conclusions drawn since they do not rely on the magnitude of the absolute values but rather on their relative differences.
To continue with the description of the magnetic field dependence of the transport properties of (Ga,Mn)As let us address once again the Hall effect. The conventional configuration for the Hall effect involves an applied magnetic field perpendicular to the current and to the voltage probes, namely a magnetic field that points out of the plane of the Hall device. However, if the magnetic field is applied in the plane of the device rather than normal to it a component of the electric field can appear normal to the current and also normal to the ordinary Hall effect. This is a pseudo Hall effect or most commonly known as the planar Hall effect. It arises due to the difference between the electrical resistivity measured when the magnetization is perpendicular ($\rho_\perp$) or parallel ($\rho_\parallel$) to the current. If the magnetization makes an angle θ with the current density then, because of the difference between $\rho_\perp$ and $\rho_\parallel$ the resistivity of the sample is effectively anisotropic so that the electric field and the current are not longer parallel [80]. The component of the electric field that is perpendicular to the current is given by a sinusoidal function of the angle 2θ that divided by the current density gives the following expression for the transverse resistivity:

$$\rho_{xy} = \frac{-(\rho_\perp - \rho_\parallel)}{2} \sin(2\theta) \tag{2.12}$$

The planar Hall effect, thus, can provide information on the magnetization dynamics in a similar way as the anisotropic magnetoresistance (ρ_{xx}).
In (Ga,Mn)As the planar Hall effect is particularly strong showing signals up to four orders of magnitude larger than in the case of metallic ferromagnets which is why the effect is also called 'giant planar Hall effect' [54]. This unusually enhanced effect is also present in the absence of a magnetic field as a spontaneous transverse voltage that develops due to spin-orbit coupling solely in response to a longitudinal current. However, it is most interesting to employ the marked magnetic field dependence of this effect together with

the anisotropic magnetoresistance to elucidate the magnetic anisotropy in (Ga,Mn)As. It follows from the expression given for ρ_{xx} and ρ_{xy} that for a system with cubic biaxial anisotropy, as it is the case for (Ga,Mn)As, there are certain configurations for the direction of the current that give the optimum signal. In the case of the current running along one of the easy axes a distinct and sharp magnetization reversal event can be observed when monitoring the longitudinal resistance in the presence of 90° domain walls. The same holds for the case of the Hall bar (and therefore the current) directed along a crystalline hard axis, namely bisecting the two biaxial easy axes, and the transverse resistance.
In order to probe the magnetic anisotropy by transport means it is not enough to measure the anisotropic magnetoresistance and the planar Hall effect in only one direction of the magnetic field. The most widely spread method involves recording the magnetic field dependencies of either ρ_{xx} or ρ_{xy} for different angles of the applied magnetic field with respect to the direction of the current. From each one of these measurements the field necessary to reorient the magnetization, the coercive field, can be extracted and plotted in a polar graph as a function of the direction of the applied in-plane magnetic field. This plot can give a considerable amount of information on the magnetic anisotropy, most importantly the direction of the easy axes that can be in turn related to the relative strength of the two in-plane anisotropy contributions in (Ga,Mn)As. This method has been widely exploited in this work to trace the changes in anisotropy resulting from the effects of temperature (chapter 3), of the incorporation of oxygen species (chapter 4) and of the adsorption of molecules (chapter 5).

2.2.3 Angle-resolved coercive field measurements

As mentioned in Section 2.1.3 the coercive fields can be in principle obtained by means of the longitudinal Kerr effect. However, the number of measurements needed to obtain enough data points for the angle dependence makes this method inconvenient since in the experimental set-up described previously the sample can not be rotated inside the cryostat. In this way each measurement requires warming up and cooling down the system which can become considerably time consuming. In order to perform these measurements more efficiently another cryogenic set-up has been employed for the angle-resolved magneto-transport studies. This system has no optical access but has a step motor that provides the desired rotation inside the refrigeration chamber and perfectly complements the system described in Section 2.1.3.
Unlike the one already presented this cryostat does not rely on the thermo-

coupling of the sample to a cold finger but cools the sample to liquid He temperatures via a He exchange gas. The lowest temperatures achievable by this cryostat are on the order of 1.6 Kelvin. In addition, it is equipped with a superconducting magnet hat provides magnetic fields as high as 12 Tesla and can be used for measurements where the magnetization is required to be saturated along the field direction. The step motor is one of the great advantages of this system which allows for a full 360° rotation with a smallest step size of 1°. This rotation can span the magnetic field within the plane of the sample or also from in to out of plane depending on the initial position of the chip carrier. A simple illustration of the sample holder including the electrical connections to the (Ga,Mn)As devices and the sample position with respect to the magnetic field is shown in Fig. 2.9. In this configuration the field is always in the plane of the sample which rotates as indicated by the red arrow.

At this point it is worth to comment on the structure and fabrication of the (Ga,Mn)As devices used for the magneto-transport measurements. These structures are patterned in the shape of standard Hall bars as shown in Fig. 2.7 where two main pads serve as bias current connections together with several side leads used for monitoring longitudinal and transverse voltages.

The first step in the fabrication of these devices consists in defining the so-called mesa structure of (Ga,Mn)As that will later support the electrical connections. This pre-structuring of the bare (Ga,Mn)As films is done by photolithography followed by wet etching. The lithographic procedure is based on the modification of a coating polymer, the photoresist, upon exposure to ultraviolet-visible light. In a first step the photoresist is spin-coated on the (Ga,Mn)As films to assure a homogeneous thickness which can be adjusted by the rotation speed and in this case is typically of 400 nm. Subsequently, the sample is laid under a mask that contains the Hall bar structures, namely, as reflective and transparent regions determining the parts that will be protected and exposed to the light, respectively. In a positive process, as the one used here, the parts of the photoresist that have seen the light can be thereafter be removed leaving some parts of the film exposed. At this stage the films with the patterned photoresist are introduced in an etching mixture of H_2O_2/H_2SO_4 with an etching rate of 40 nm/min (for GaAs). In this way, the (Ga,Mn)As material exposed is etched away until reaching the underlying GaAs to define the mesa structures. The etching time required varies with the thickness of the (Ga,Mn)As layer that is being patterned and it is normally set as to etch twice the value of the thickness of the magnetic film to assure the perfect decoupling of each individual device from the neighbouring ones. After this procedure is completed the remaining photoresist protecting the GaMnAs Hall bars is completely removed and a new lithography process

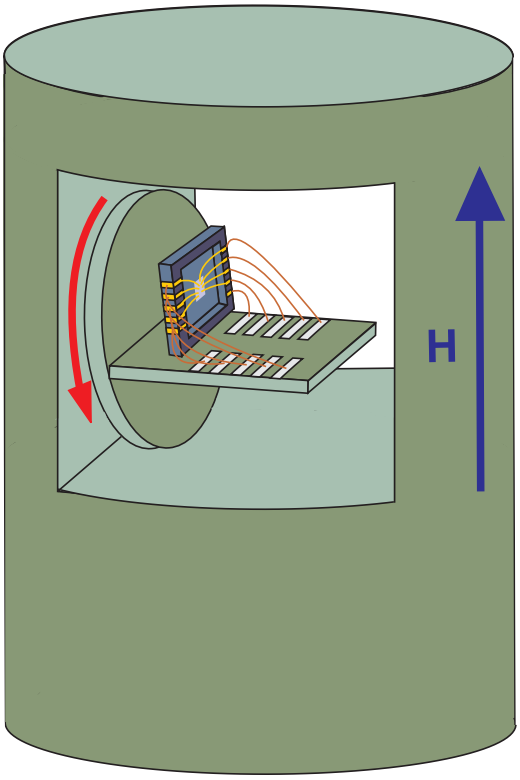

Figure 2.9: Illustration of the sample holder used to perform angle-resolved magneto-transport measurements at low temperatures. The direction of the magnetic field together with the sense of rotation of the chip-carrier are indicated by arrows. The shown sample orientation corresponds to the longitudinal and Hall measurements with in-plane fields.

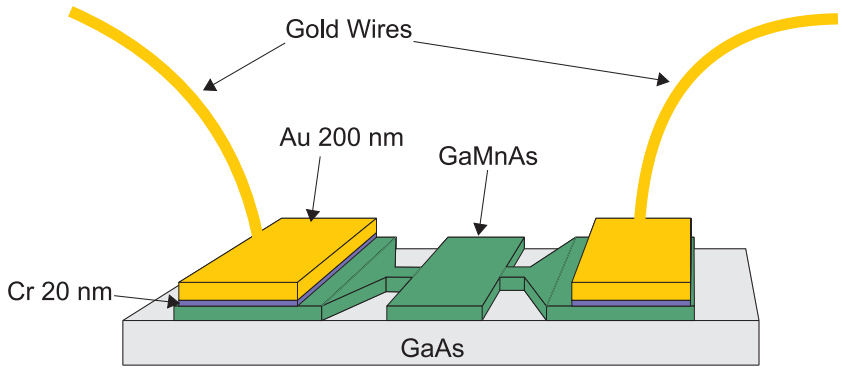

Figure 2.10: Sketch of the electrical contact structure of the (Ga,Mn)As devices. A layer of Cr is evaporated prior to the Au deposition to reassure the good stability of the gold wires bonded to the pads.

starts, this time for defining the metal pads for the electrical connections. In this case the regions left unprotected by the photoresist will be covered by the metal chosen for the contact pads. The structure of the pads consists of a layer of chromium in direct contact with (Ga,Mn)As followed by a layer of gold as shown in Fig. 2.10. The thicknesses of these layers are typically of 20 and 200 nm for Cr and Au, respectively. The intermediate Cr layer is needed for a good adhesion of the Au layer which is crucial for the bonding of gold wires on the pads. Finally the bonding to the chip-carrier is realized by applying an ultrasonic pulse to the bonding wire in contact with the gold pad. This pulse that can be regulated in strength and duration produces a local melting of the Au wire and in this way builds an electrical contact between the wire and the pad.

The experimental techniques described in this chapter are those extensively used in this work. Other techniques such as Superconducting Quantum Interference Device (SQUID) magnetometry, X-ray photoelectron spectroscopy and X-ray absorption spectroscopy have been used additionally but to a much lower extent which is why they are not explained in detail. However, a brief description will be given in the corresponding chapters before the presentation of the experimental data provided by each one of these techniques.

Chapter 3

Magnetic domain wall dynamics in GaMnAs/GaAs

In this chapter the experimental results on magnetic domain wall dynamics in compressively strained (Ga,Mn)As materials will be presented. The chapter is divided in two main sections. In the first part the interplay between in-plane biaxial and uniaxial anisotropy will be analyzed as a function of temperature. Studies of domain wall propagation at variable temperatures give valuable information on how the anisotropy affects the domain wall dynamics.
In the second part of this chapter magnetic relaxation processes in GaMnAs/GaAs will be addressed. In this section a general introduction to the magnetic aftereffect and the various models that can successfully describe it will be given. In the end, the formulation proposed for the modeling of the aftereffect in (Ga,Mn)As is discussed in detail.

3.1 Biaxial to uniaxial magnetic anisotropy transition in (Ga,Mn)As

According to the concepts mentioned in chapter 1, the magnetic anisotropy in GaMnAs/GaAs has two main contributions, a biaxial and an uniaxial term. These contributions are dependent on the value of the magnetization with different power laws. Therefore, since M is temperature dependent a temperature variation will allow for the study of different anisotropy regimes where either the biaxial or the uniaxial component is dominant. In the following this temperature dependence will be analyzed in terms of the projection of the magnetization on the easy axes of biaxial and uniaxial anisotropy a quantity which is accessible from SQUID measurements. This information

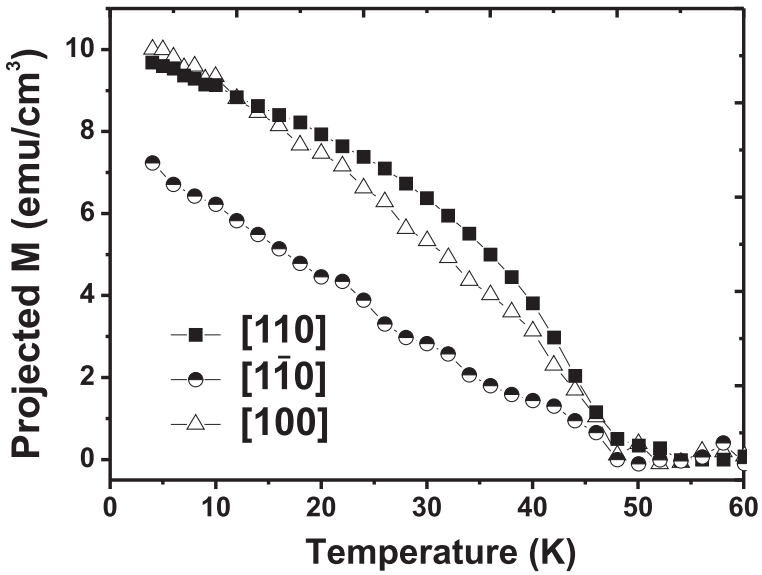

Figure 3.1: Projected magnetization as a function of temperature measured by SQUID in a non saturating magnetic field of 50 Oe. The different curves correspond to the magnetic field applied along one biaxial easy axis ([100]), the uniaxial easy axis ([110]) and the uniaxial and biaxial hard axis ([1$\bar{1}$0]) indicated by full squares, open triangles and half open circles, respectively.

together with the change in the shape of the angle-dependence of the coercive field as a function of temperature will be used to interpret the domain wall dynamics below and above the temperature where the system switches from a biaxial to a uniaxial dominated magnetic anisotropy in section 3.1.2.
The sample used in the studies presented in this first section is a GaMnAs/GaAs film of 170 nm thickness with a manganese concentration of 5% and a Curie temperature of 49 Kelvin. A summary of the most relevant properties of all the samples used in this thesis can be found in the appendix.

3.1.1 Temperature dependent magnetic anisotropy

The value of the magnetization as a function of temperature was measured by SQUID starting from the lowest temperature after cooling down the sample in a field of 1000 Oe. The measurements were performed by applying a non-saturating magnetic field of 50Oe in three different crystalline directions. These directions are the uniaxial easy axis ([110]), one of the two biaxial easy axes ([100]) and the uniaxial and biaxial hard axis ([1$\bar{1}$0]) as indicated in Fig. 3.1. The magnetization that is measured by SQUID is the projection of the

saturation magnetization on the axis of the applied field. Thus, the SQUID technique allows to trace not only the absolute magnitude (by using a saturating field) but also the angle of the magnetization with respect to the field direction (when applying a non-saturating field). As follows, the temperature dependence of the magnetization direction can give important information of the magnetic anisotropy when correlated with the crystalline axes of the sample which is done by evaluating the changes in the projections on these directions.

The plot in Fig. 3.1 shows the projected magnetization values versus temperature measured using SQUID. In the lowest temperature regime the projected magnetization on the [100] and [110] directions are similar. This indicates that the contributions from the biaxial and uniaxial terms seem to be comparable. In the region between 15 and 25 K a transition is occurring where the importance of the uniaxial term increases with respect to the biaxial term. Finally, at temperatures around 30 K the uniaxial anisotropy component is already clearly dominating over the biaxial contribution. Despite the changes in the strength of the uniaxial and biaxial components the $[1\bar{1}0]$ remains the hard axis through the whole temperature range.

As mentioned in the first chapter this biaxial-to-uniaxial transition is due to the different dependencies of the anisotropy constants on the magnetization, and therefore on temperature. In the literature the biaxial anisotropy constant is found to be proportional to $M(T)^4$ while the uniaxial anisotropy constant is proportional to $M(T)^2$ [56]. The biaxial anisotropy constant, thus, is expected to dominate at high values of M, however, it is also expected to decrease faster than the uniaxial anisotropy constant as M decreases. Therefore, between 2K and T_c a crossing over occurs that is in close correspondence with our experimental observations.

This anisotropy transition is also evident from the angle dependence of the coercive fields. As illustrated in Fig. 3.2, the magnetization loops measured by means of the magneto optical Kerr effect (MOKE) can have more than one transition in certain directions. The coercive fields corresponding to these transitions are denoted as H_{c1} and H_{c2} and reflect the two easy axes directions in the GaMnAs system. The magnetization loop that is taken as example in Fig. 3.2 (b) corresponds to a magnetic field applied in the [100] direction (45°). Typically, in (Ga,Mn)As the polar plot of H_{c1} and H_{c2} as a function of the direction of the applied field (in this case with respect to the hard $[1\bar{1}0]$ direction) H_{c1} qualitatively describes a rectangle whose aspect ratio is determined by the interplay between biaxial and uniaxial anisotropies. Along the global easy axis the system shows the largest H_{c1}, which is namely, the corner of the rectangle. Thus, in the case of a pure biaxial anisotropy the corners of the rectangle should coincide with the [100] and [010] directions, and the

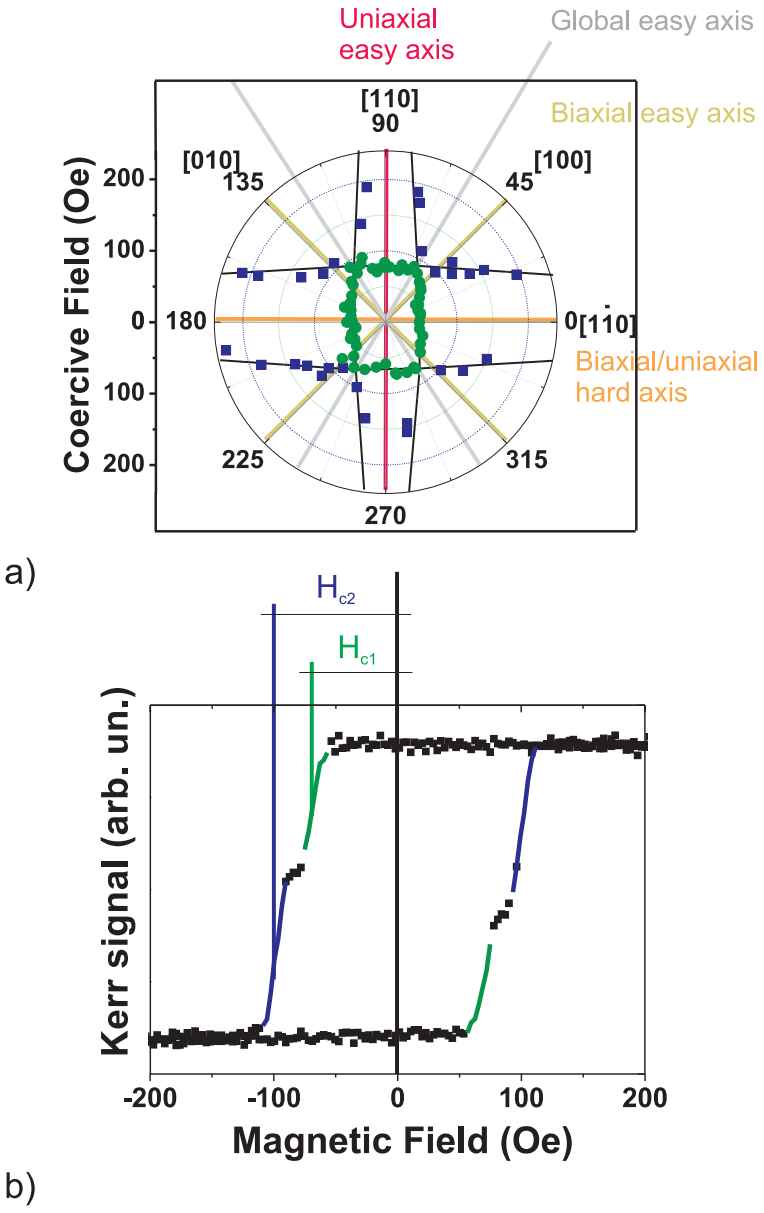

Figure 3.2: (a) Polar plot of the coercive field as a function of the direction of the applied magnetic field with respect to the [1$\bar{1}$0] direction at a temperature of 3 Kelvin. (b) Double step magnetization loop along the [100] direction with coercive fields H_{c1} and H_{c2} indicated by green and blue, respectively.

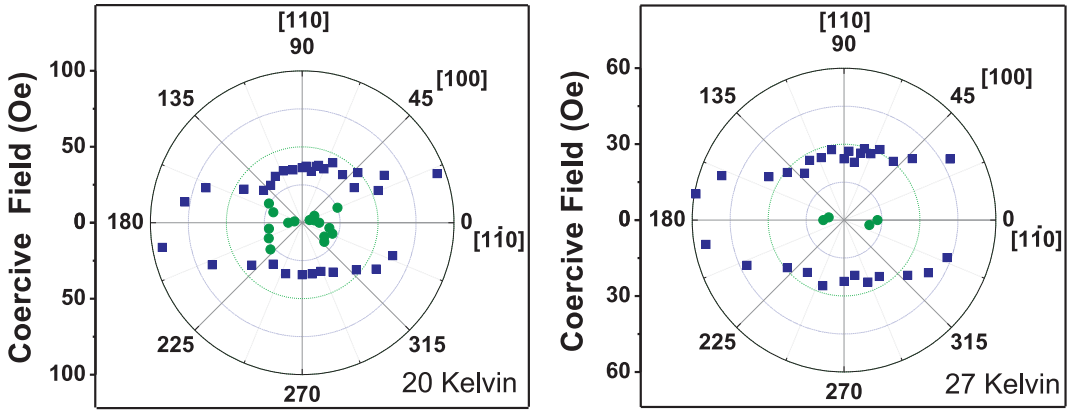

Figure 3.3: Angle dependence of the coercive field at 20K (left) and 27K (right). The uniaxial magnetic anisotropy is dominating the anisotropy landscape at 27K.

rectangle becomes a square. In light of these facts, we can conclude that the extent of the deformation of this square into a rectangle is a measure of the contribution from the uniaxial anisotropy term. The value of the second coercive field H_{c2} describes two pairs of almost parallel lines directed along the uniaxial easy and hard axes, the [110] and [1$\bar{1}$0] crystalline directions, respectively. In rigor, the complete graph could be thought simply as the intersection of two sets of parallel lines rotated by a 90° angle with respect to each other. In this picture the inner part of the lines is described by H_{c1} while the extremes are defined by H_{c2}. This model will be recalled in the following section to introduce the fitting procedure employed for modeling the angular dependence of the coercive field.

As the temperature is increased a strong change in the shape of the polar coercivity plot can be observed. Shown in Fig. 3.3 are the polar plots measured at 20K and 27K. The plot at 20K illustrates an intermediate state in the biaxial-to-uniaxial transition. The lines corresponding to H_{c2} have disappeared along the uniaxial easy axis direction indicating that the magnetization reversal in the close vicinity of this direction has changed from a two step to a single step process. This gives a hint towards the enhancement of the uniaxial easy axis since the magnetization reversal is now more favorable to occur with both the initial and final state along the [110] direction. However, moving away from this axis the two step reversal can still be found. In the 27K plot the uniaxial anisotropy contribution has fully developed in detriment of the biaxial term. There are single transitions in all directions

and the reversal mechanism seems to be mediated in all cases by coherent rotation of the magnetization and successive nucleation/propagation of 180° domain walls separating two opposite magnetization states oriented along the uniaxial [110] easy axis.
In this way combining the information given by SQUID and the MOKE angle dependence of the coercive fields the temperature ranges corresponding to the full biaxial and full uniaxial anisotropy landscape have been identified. With this information let us look at the magnetic domain wall dynamics in both the biaxial and uniaxial regime at temperatures of 3K and 27K, respectively.

3.1.2 Magnetic domain wall alignment

In this section the changes in the domain wall dynamics, in particular the domain wall alignment with respect to the crystalline axes, associated with the transition between biaxial and uniaxial anisotropy will be discussed. Although the internal structure of the domain walls can not be resolved by our Kerr microscopy equipment, still very important information can be extracted from the spacial arrangement of the domain walls in the films.
In Fig. 3.4 the nucleation/propagation of the magnetic domain walls under a constant magnetic field at 3K is shown. The magnetic field is chosen just above the coercive field to induce a slow transition. In this case the (Ga,Mn)As bare film had been previously patterned into a Hall bar structure of 200 μm width as described in chapter 2. This geometry was introduced in order to observe the magnetization reversal in a geometry that is normally used in standard Hall effect measurements. The first observation from these images is the selective domain nucleation at the contact pads. This can be related to small demagnetizing fields arising at the narrower constrictions whose long axes are perpendicular to the magnetic field. In this images several domain walls can be distinguished which tend to have an approximate $\pm 25°$ orientation with respect to the $[1\bar{1}0]$ axis (vertical axis). At this point one step back should be taken to give a few words on the nature of the domain wall that is involved in this process.
It is known from various experimental studies including our own [54, 55, 81] that because of the interplay between the biaxial and uniaxial anisotropy terms in (Ga,Mn)As different domain walls of reduced angle can be found for different directions of the applied magnetic field with respect to the crystalline axes. The deviation of these domain walls from 90°, 90° being the pure biaxial anisotropy case, is determined by the extent of the uniaxial anisotropy contribution. In the cited publications it is discussed how the deviation from 90° can be estimated by evaluating the shift of the global easy axes away from the [100] and [010] directions. It is found that the reversal

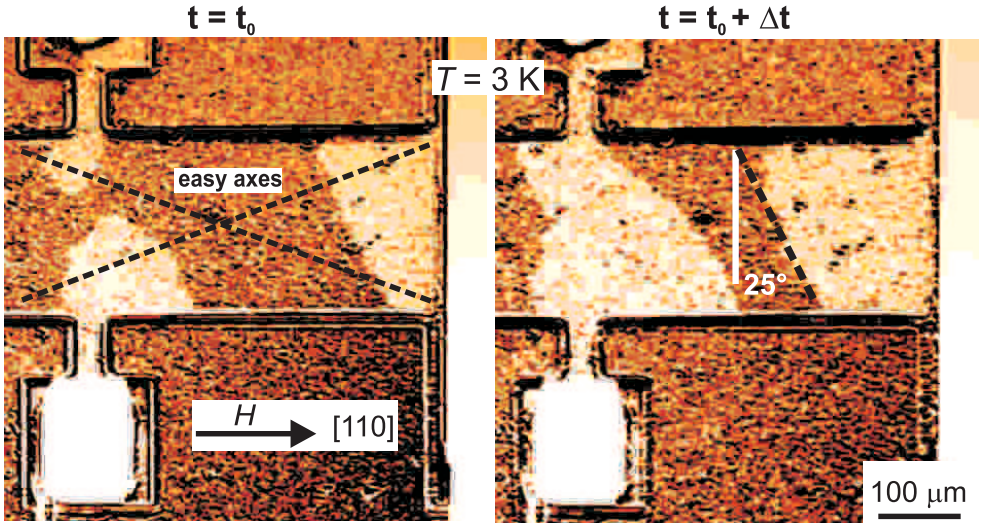

Figure 3.4: Two subsequent frames showing the propagation of magnetic domain walls in a (Ga,Mn)As Hall bar structure. The magnetization reversal is mediated by 120° domain walls. There is a preferential ±25° orientation of the domain walls with the $[1\bar{1}0]$ axis.

mediated by two 90° domain walls typical of a material with purely cubic anisotropy is replaced by a process with one $90° + \delta$ and one $90° - \delta$ domain wall where the value of $\delta/2$ is the shift of the global easy axes due to the uniaxial anisotropy contribution. This value can be extracted from the shift of corners of the rectangle described by H_{c1} in Fig. 3.2 (a) away from the cubic directions. In our case the value of $\delta/2$ extracted from the polar plot at 3K is 15°. Therefore we expect to find domain walls with an angle deviating 30° from the purely biaxial case, namely 120° and 60° domain walls.

The particular directions of the applied magnetic field that will trigger magnetization reversal processes involving one or the other type of walls can be deduced by fitting the angle dependence of the coercive fields. The following expression models the two pairs of quasi parallel lines observed in the polar plot in Fig. 3.2 oriented along the [110] and $[1\bar{1}0]$ directions for the $90° + \delta$ and the $90° - \delta$ cases, respectively [55].

$$H_{90\pm\delta} = \frac{\epsilon_{90\pm\delta}}{M\sqrt{2}\cos(45 \mp \frac{\delta}{2})(\sin(\varphi_H) \mp \cos(\varphi_H))} \tag{3.1}$$

where $\epsilon_{90\pm\delta}$ is the domain wall nucleation/propagation energy. The fitting procedure allows to identify that the coercive fields describing the pair of lines parallel to the $[1\bar{1}0]$ direction correspond to a magnetization reversal

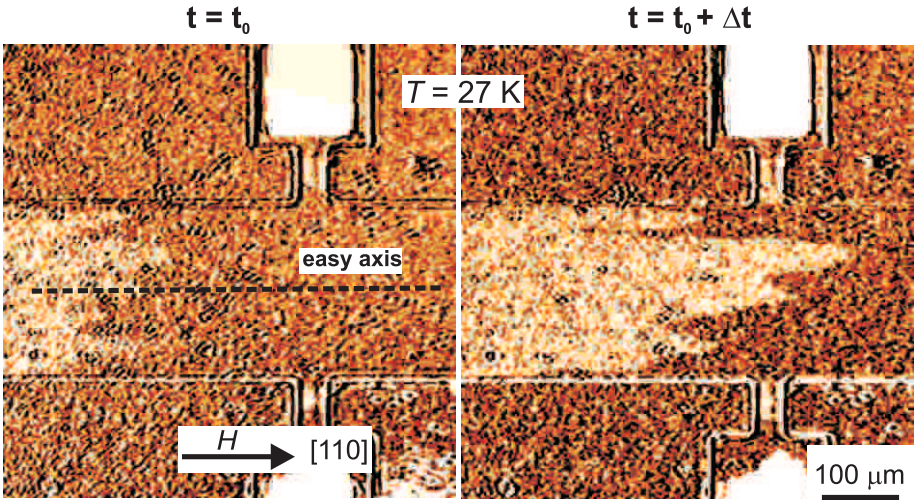

Figure 3.5: 180° magnetic domain walls under a constant magnetic field along the [110] easy axis direction at 27K in the uniaxial anisotropy regime. In this case there is a clear tendency of the walls to align with the uniaxial easy axis. The (Ga,Mn)As device is the same as that in Fig. 3.4.

mediated by 120° domain walls. On the other hand, the pair of lines perpendicular to the $[1\bar{1}0]$ axis describes a 60° domain wall mediated reorientation of the magnetization. To be more explicit this means that at 3 Kelvin 120° domain walls will be found for H_{c1} for magnetic fields applied in the angle range ± 30° from the [110] uniaxial easy axis and also for H_{c2} when the field is applied ± 60° from the $[1\bar{1}0]$ direction. The opposite holds for the 60° domain walls. These walls of reduced angle can be found for H_{c1} within a range of ± 60° from the $[1\bar{1}0]$ direction and for H_{c2} within a range of ± 30° from the [110] direction. The crossing point between 60° and 120° domain walls for a given coercive field H_{c1} or H_{c2} as the magnetic field is rotated is located at the positions of the global easy axes (the corners of the rectangle described by H_{c1}).

Using this it is now possible to identify the type of domain walls that are present in the images of Fig. 3.4. This reversal corresponds to the coercive field H_{c1} and as indicated in the figure with the magnetic field applied along the [110] direction. In view of what was stated in the previous paragraphs the domain boundaries presented in these images are 120° magnetic domain walls.

Recalling the changes in the magnetic anisotropy as a function of temperature it has been already mentioned that in the high temperature regime where the uniaxial anisotropy is dominant 180° domain walls are preferred

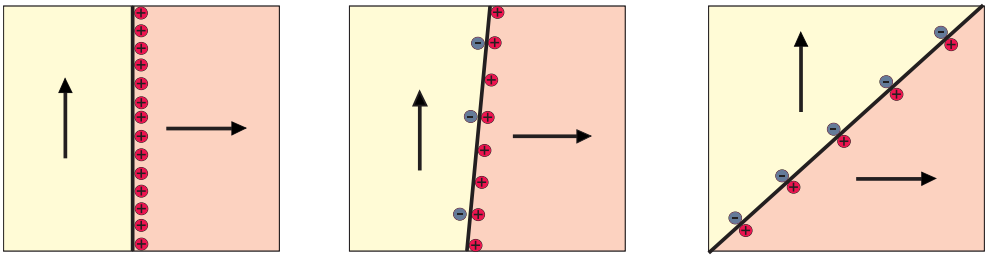

Figure 3.6: Magnetic 'free poles' at the interface between two domains with magnetization vectors rotated 90° respect to each other. The 'free poles' can be compensated by the rotation of the domain wall such that it intercepts the angle between the magnetization states at both sides of the wall (right).

for the magnetization reorientation. Thus, by studying the domain wall dynamics at 3K and 27K it is possible to identify differences for 120° and 180° domain walls in GaMnAs/GaAs. To this end, after performing the Kerr microscopy measurements of Fig. 3.4 the temperature was raised to 27 Kelvin and the magnetization reversal under a constant magnetic field was imaged once again on the same Hall bar device. The corresponding images are presented in Fig. 3.5. In this case the reversal seems to be taking place via the expansion of a single domain possibly nucleated at the bias contact pad on the left side of the device. Nucleation at the contact leads can still be observed although these small domains do not expand into the wide channel of the Hall bar as seen in the 3K measurements. The most striking observation when comparing to the low temperature case is the dramatic change in the domain wall orientation. At 27 Kelvin the domain walls present a clear preference for aligning parallel to the [110] easy axis direction.

For a better understanding of the domain wall alignment the concepts of stray fields discussed in chapter 1 need to be revisited. If the domain wall is thought as an infinitely thin interface between two domains with magnetization vectors pointing in different directions it becomes evident that this interface can show so-called 'magnetic poles' arising from the sudden discontinuity of the magnetization, just like on the surface of a magnetic material. The elimination of these energetically unfavourable poles at the domain wall can be achieved if the magnetization components perpendicular to the domain wall in the two domains separated by this wall are equal and therefore cancel each other out. This reduction in energy can be induced in the system by rotating the wall with respect to the magnetization vectors in order to equalize the magnetization components perpendicular to the wall [62]. This concept is illustrated in Fig. 3.6 for a 90° domain wall. In certain cases the

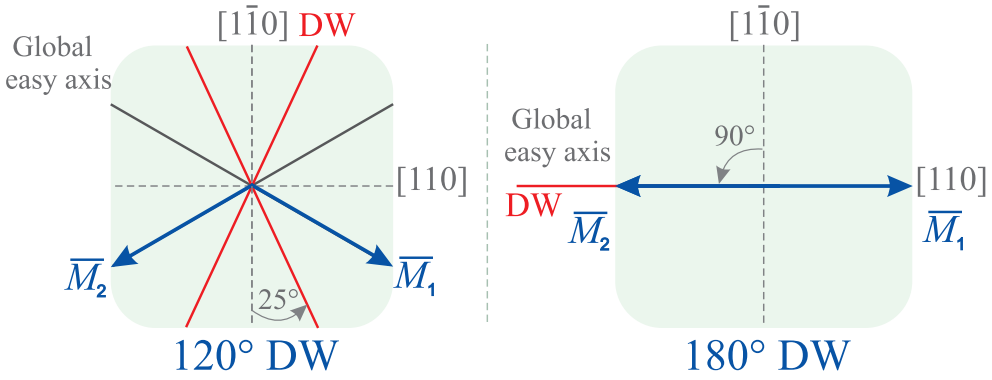

Figure 3.7: Diagram of the observed alignment of domain walls with respect to the easy axes and the directions of magnetization for the low (left) and (high) temperature cases.

rotation is not completed as to fully eliminate the free poles and therefore the wall is said to be 'charged'.

Let us now analyze what is expected in terms of domain wall alignment for the two cases we have previously discussed, namely 120° and 180° domain walls in (Ga,Mn)As. The general configuration that could provide a full compensation of the free poles for any type of domain walls is the one where the wall bisects the angle between the initial and final magnetization state. Considering this, in the present case the 120° domain walls are expected to align perpendicular to the [110] direction and the 180° domain walls could align either parallel or perpendicular to the same axis. However, in practice quite some discrepancies with this model were found, in Fig. 3.7 a summary of the alignment of the domain walls with respect to the easy axes and the magnetization directions for both low and high temperature cases is presented.

In the case of 180° domain walls the experimental observations seem to fit the predictions. However, only one of the two possible arrangements is adopted by the system. Looking more closely at these two possibilities one sees that when the wall lies perpendicular to the magnetization the wall is a so-called head-to-head wall where poles are generated and compensated at the boundary. On the other hand, if the wall is parallel to the initial and final magnetization vectors the wall is still not charged but not because of compensation but because there are no poles at all being generated at both sides of the wall. This last configuration has most likely a lower energy compared to the head-to-head case and therefore would be expected to prevail.

The analysis of the alignment of 120° domain walls is not as simple as that for 180° walls. In this case the walls are ∼25° rotated from the expected

direction parallel to the $[1\bar{1}0]$ axis. The domain wall in this case is clearly charged and proposing that it is due to a tendency to reduce the domain wall area is not applicable since the domain wall area in this case is larger than what it would be if it adopted the predicted alignment. One possible explanation for the deviation from the simple model presented above is related to the magnitude of the magnetic parameters such as saturation magnetization, magnetic anisotropy and the exchange constant in (Ga,Mn)As. In this material these parameters are remarkably lower than those found for instance in $3d$ metals. The stray field energy densities in (Ga,Mn)As can be orders of magnitude lower than for example those for iron, and therefore might not be the determining factor for the optimum domain wall alignment [82]. In addition, in very thin films there is the possibility of finding more complex Néel wall shapes compared to the simple picture presented in chapter 1. For these cases theory predicts that charged walls can be among the possible solutions even in the presence of non-zero stray fields [83].
Even though the appearance of charged domain walls in magnetic materials is not rare a throughout general explanation of extensive applicability is still lacking.

3.2 Magnetic aftereffect in the biaxial anisotropy regime

In this section the space resolved study of the domain wall dynamics in (Ga,Mn)As presented in the last part will be complemented with time resolved studies of magnetic relaxation processes. The study of the magnetic aftereffect in this work has been performed by time and space resolved Kerr microscopy and time dependent magneto-transport. For all measurements the temperature of the samples was 3 Kelvin, therefore the study has been carried out in the biaxial anisotropy regime.

3.2.1 The magnetic aftereffect

The interest in magnetic relaxation effects can be traced back several decades where the study was mostly centered around the influence of the aftereffect in the mechanical properties of materials [84].
Magnetic relaxation effects during domain wall transitions as described by Néel have two distinct origins and are called reversible and irreversible aftereffects [85, 86]. In the irreversible aftereffect the time variation of the magnetization is attributed to the thermal activation of the magnetization

reversal. The reversible aftereffect (or diffusion aftereffect) is also a thermally activated process but it is associated to the diffusion and reorientation of the symmetry axis of point defects inside the structure of the ferromagnet [87,88]. This diffusion of defects is a consequence of the general tendency of the system to find a lower energy minimum. In this case of the reversible aftereffect a new lower minimum can be found by changing the orientation of the symmetry axis of the defect with respect to the local magnetization direction within the domain wall. The most effective path to realize this is a short range migration to a different neighboring site. This lower energy minimum exists only if the symmetry of the defect (interstitial) sites differs from that of the ideal lattice (substitutional) sites [84, 89].
Although (Ga,Mn)As seems to be a good a candidate to show the reversible aftereffect due to the well-known presence of interstitial Mn atoms in the lattice, symmetry arguments speak against it as will be shown in the following. In chapter 1 only the presence of interstitial Mn atoms in (Ga,Mn)As due to a non-equilibrium growth was discussed, however, the interstitial sites that can potentially host these atoms can have either tetrahedral or hexagonal symmetry. These two geometries of the interstitial sites are also not equivalent from an energetic point of view. In fact, from experimental and theoretical work it is known that interstitial Mn atoms exclusively occupy tetrahedral sites [90, 91]. This has important consequences for the mechanism of the magnetic aftereffect. Since the non-equality of the symmetry of the interstitial sites with respect to the substitutional sites is not fulfilled in (Ga,Mn)As (both sites are tetrahedral) the reversible aftereffect is not expected to occur. Therefore, taking into account these symmetry considerations the magnetic relaxation processes observed in this study can be attributed to the irreversible aftereffect.
After identifying the type of aftereffect that is involved in the relaxation process in (Ga,Mn)As a brief recount of the possible and most simple models describing it will be given in the following. The mathematical formulation of the magnetic aftereffect involves deriving an expression for the time dependence of the magnetization *M(t)* averaged over a large area of the sample. This can be done in a simple way by considering the aftereffect as a relaxation process with a relaxation time τ [93, 95]:

$$M(t) = \alpha + \beta \exp[-t/\tau] \tag{3.2}$$

The constants α and β are time independent and the relaxation time τ, for the case where the transition occurs via domain wall motion, depends both

on temperature and magnetic field according to [93, 94]:

$$\tau = \tau_0 \exp[E_A/k_B T] \tag{3.3}$$

Here τ_0 is a pre-exponential factor fairly independent of the field, T is the temperature and E_A is the activation energy that has the following expression:

$$E_A = 2M_s\cos(\phi)V(H_A - H) \tag{3.4}$$

where V is the activation volume, $2M_s\cos(\phi)$ is the total magnetization change during the switching process projected on the field direction (ϕ is the angle between M_s and the field direction), and H_A is the propagation field without thermal activation. In a more complex scenario where a wide distribution of relaxation times are present, the following expression is commonly used assuming a flat-topped distribution function for τ:

$$M(t) = \gamma - S\ln[t] \tag{3.5}$$

where S is the coefficient of magnetic viscosity that includes the activation volume and γ is a constant independent of t [95].
In the following section the results obtained for the magnetic aftereffect in (Ga,Mn)As will be presented. It will become evident that none of the models described here can accurately fit the obtained time dependence of the magnetization. In order to model the magnetic aftereffect in (Ga,Mn)As an alternative formulation partially based on those introduced here will be presented and discussed.

3.2.2 Time dependence of the magnetization

Domain wall velocity measurements have been carried out on two samples grown in two different MBE laboratories to confirm that the present study on the magnetic aftereffect has a far-reaching validity in the field of ferromagnetic (Ga,Mn)As materials. The as-grown samples employed in this study (samples A and B, respectively) have different Mn concentrations (2.5 and 8 % Mn) and Curie temperatures (53 and 65 Kelvin) and are also of different thicknesses (170 and 50 nm).
The irreversible magnetic aftereffect in the compressively strained (Ga,Mn)As samples was measured by tracking the position of individual domain walls versus time. The respective position is monitored in movies taken during Kerr microscopy [69]. To obtain a well-defined initial magnetization state, the magnetic film was first saturated in a positive in-plane field of 500 Oe.

After reducing the field to zero in one step, an opposing magnetic field of a certain value just below the coercivity was applied which remained constant through the entire time of the Kerr microscopy measurement. As mentioned, all measurements where carried out at a temperature of 3 Kelvin and with the magnetic field applied along the uniaxial easy axis direction ([110] and $[1\bar{1}0]$ for samples A and B, respectively).

The time variation of the position of the domain wall is tracked as a function of the applied magnetic field and always in the exact same section of the film (see Fig. 3.8 (b)). The starting time of the measurement ($t = 0$) is defined as the time corresponding to the frame (in the Kerr microscopy movie) that precedes the first image where the smallest switched area is observed. The reverse domain area (DA) at different times is normalized with respect to the size of the whole image (500μm x 500μm), and by considering the difference between the switched and the unswitched areas a local value of the magnetization ($\tilde{M}$) for the portion of material under analysis can be evaluated. This calculation is pictured in Fig. 3.8 (a) where M_s is the saturation magnetization of the film obtained from SQUID magnetometry. The corresponding saturation magnetization values for samples A and B (obtained in a saturating field of 1T) are 10 emu/cm^3 and 40 emu/cm^3, respectively. In the following, the magnetization values used in the modelling of the magnetic aftereffect will correspond to $\tilde{M}$.

As already discussed in-plane magnetized GaMnAs/GaAs materials with Curie temperatures and magnetization values in the range of those corresponding to the samples studied here are known to exhibit a biaxial dominated anisotropy landscape at low temperatures that evolves into an uniaxial regime at higher temperatures. The angle between the global easy directions and the biaxial and uniaxial easy axes is a material and temperature dependent property. While for sample A the global easy axes are located approximately $\phi = 30°$ away from the uniaxial easy axis along [110] [81], for sample B the global easy direction is at $\phi = 45°$ with respect to the uniaxial easy axis ($[1\bar{1}0]$). Since the magnetic field is applied along the uniaxial easy axis, the value of the projection of the magnetization on the direction of the applied field for the initial state (magnetization in zero field after saturation) is approximately -$M_s$cos(30°) for sample A and -$M_s$cos(45°) for sample B and with domain wall displacement (120° and 90° domain wall, respectively) this value can grow up to $M_s$cos(30°) and $M_s$cos(45°), respectively for the switched state. Therefore, for the areas covered by the reverse domains the change in magnetization is $\Delta M = 2M_s\cos(30°)$ for sample A and $\Delta M = 2M_s\cos(45°)$ for sample B with respect to the initial state. Stoner rotation processes are considered negligible in the present case since the applied magnetic fields are very low. Only at much higher values of the magnetic

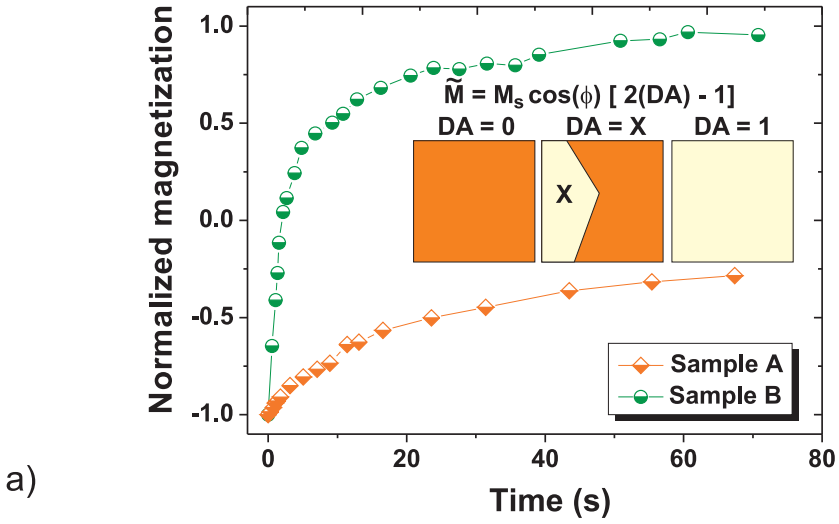

a)

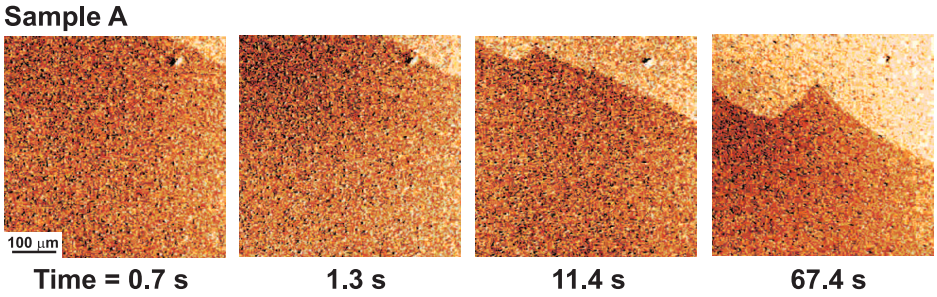

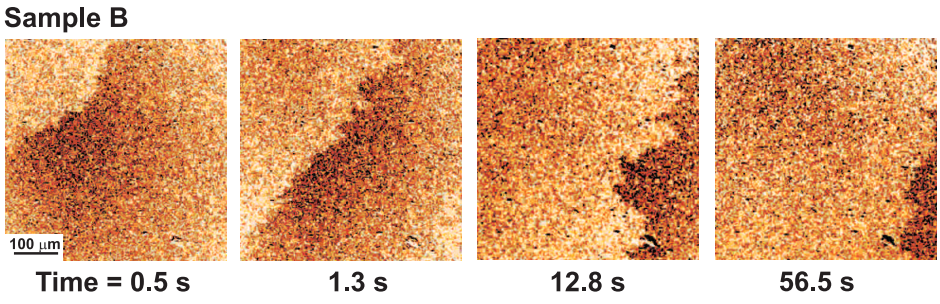

b)

Figure 3.8: (a) Normalized magnetization vs. time for sample A (diamonds) and B (circles) at a constant magnetic field of 28.0 and 24.6 Oe, respectively. The derivation of the magnetization values from the domain area (DA) at a given time is also schematized. (b) Kerr microscopy images corresponding to the curves in (a) for sample A and B at the indicated times.

field the magnetization would further rotate in a coherent way.
A typical curve of normalized magnetization vs. time calculated in the described manner (and divided by $M_s\cos(30°)$ and $M_s\cos(45°)$ for normalization) is presented in Fig. 3.8 (a) for samples A and B at a constant magnetic field of 28.0 and 24.6 Oe, respectively. The slope of these curves, that can be correlated to the domain wall velocity, is observed to decrease dramatically as a function of time which is a signature of the magnetic aftereffect. The Kerr microscopy images in Fig. 3.8 (b) correspond to four points of the curves in Fig. 3.8 (a) for sample A and B taken at the indicated times. The magnetic field is applied along the easy axes of samples A and B which lay in both cases along the horizontal axis of the images. On a larger scale the domain is mainly moving in one direction, however, kinks in the wall shape are observed which are tentatively attributed to infrequent strong pinning events at large domain wall pinning centers (macropins). These stronger pinning events introduce inhomogeneous variations of the domain wall velocity on a local scale.

It remains to verify that the observed time dependence of the domain wall velocity is not an artefact, e.g. due to the influence of light penetrating the sample during the acquisition of the Kerr microscopy movies. From the time dependent magneto-transport measurements shown in the following it becomes evident that the aftereffect is also visible in the absence of the Kerr microscope illumination. The Hall bar structures employed for these measurements are of 100μm width and fabricated by photolithography as indicated in chapter 2. The 90° orientation of the Hall bar longitudinal axis with respect to the direction of the magnetic field favors the nucleation of magnetic domains at the sides of the Hall bars [82]. This also allows for the investigation of the aftereffect in conditions where the magnetization reversal involves more than one reverse domain. The time and magnetic field dependence of the planar Hall voltage of sample B are presented in Fig. 3.9 (a) and (b), respectively. The time dependence is again recorded under constant magnetic field conditions with fields of 33.4 Oe (orange), 33.9 Oe (dark green), 34.0 Oe (red) and 39.6 Oe (light green). The overall decrease in domain wall velocity over time observed in the single domain case (Fig. 3.8) is also evident in the overall magneto-transport signal from $t = 0$ to 3300 seconds. Moreover, looking more closely to the time dependence of the planar Hall voltage, small steps corresponding to the displacement of single domain walls after nucleation can be observed. In the inset of Fig. 3.9 (a) a few of these small steps are shown in more detail. The shape of the magneto-resistive signal of a single step strongly resembles that shown in Fig. 3.8 (a) for the time dependence of the domain size for a single domain process, suggesting a similar dynamics. However, it is important to mention

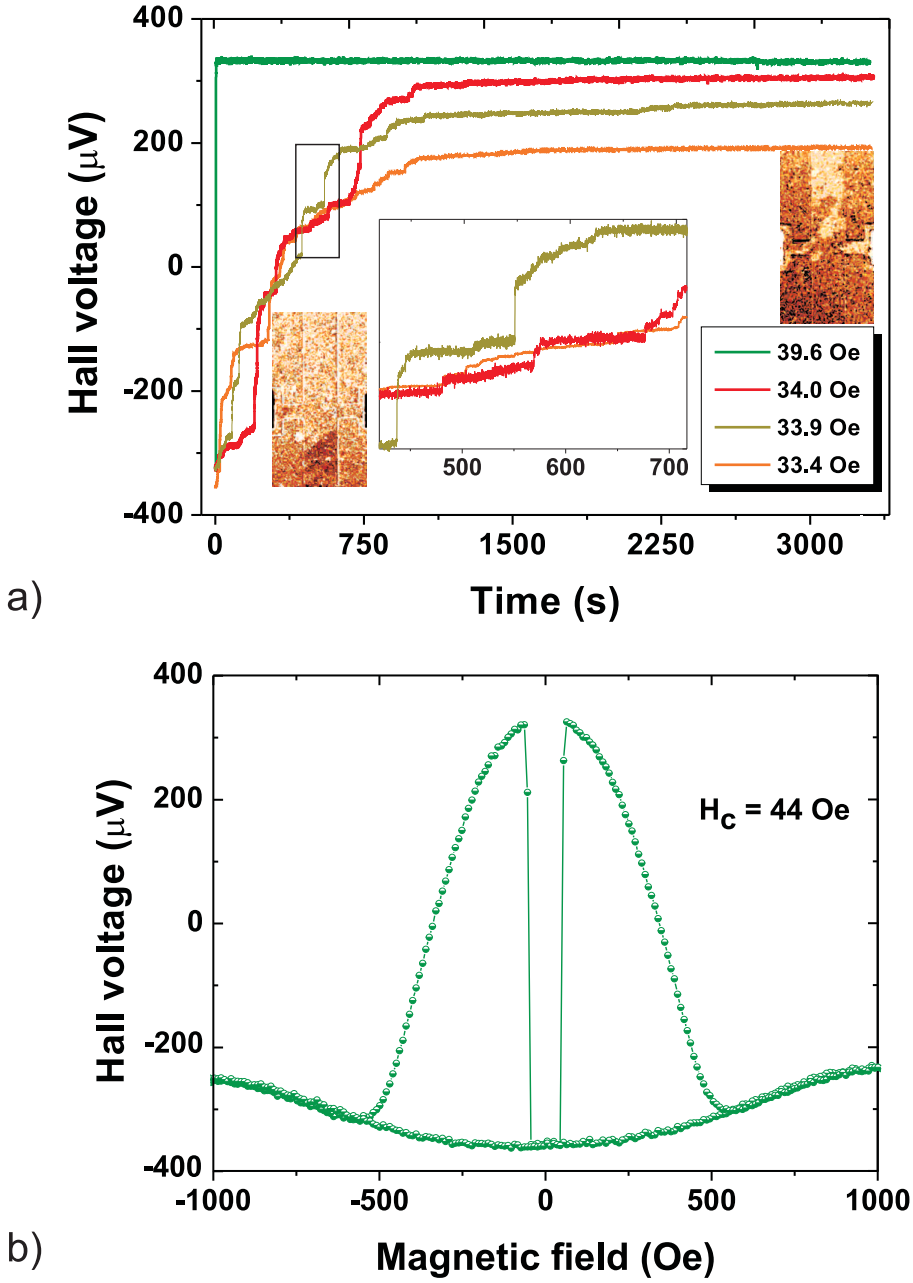

Figure 3.9: (a) Planar Hall voltage vs. time for sample B at different constant values of the magnetic field: 33.4 Oe (orange), 33.9 Oe (dark green), 34.0 Oe (red), and 39.6 Oe (light green). The steps observed in all the curves (see inset) correspond to the growth of single magnetic domains. (b) planar Hall voltage as a function of magnetic field.

that in a multi domain configuration other contributions to the domain wall dynamics may arise with respect to the single domain scenario. Interactions between neighboring domain walls can influence the dynamics by including affinities between neighboring Néel walls [96]. At the same time pinning effects at the Hall bar edges can play a role. Two typical Kerr images of the Hall device during magneto-transport are shown in Fig. 3.9, one in the early stage of reversal (left) and the other approximately 1 hour after applying a constant magnetic field (right). For comparison the bottom plot in Fig. 3.9 shows the planar Hall voltage vs. magnetic field while sweeping the magnetic field between ±1000Oe representing a full magnetization reversal of the entire device. The full domain wall transition at $H_c = \pm 44$Oe switches the device between two well-defined magneto-resistive states corresponding to $\approx \pm 325$mV, and the time-dependent graphs in Fig. 3.9 (a) can be compared to these values.
In the following, these results of domain size vs. time for sample A and B will be analyzed in terms of the known models developed to describe the magnetic aftereffect.

3.2.3 Modeling of the magnetic aftereffect

As mentioned in the introduction, in the present study the best fitting of the time dependence of the magnetization is obtained neither considering a single relaxation process nor a flat-topped distribution of relaxation times.
This disagreement with the Néel formulation has also been reported in studies analyzing the relaxation of the thermoremanent magnetization in (Ga,Mn)As within the cluster/matrix model [44] discussed in chapter 1 and in other materials such as manganite compounds. In the latter case, the time dependence of the magnetization is well described by a stretched exponential function of the form [97]:

$$M(t) = M_0 \exp[-t/\tau]^{\beta}, \quad 0 < \beta < 1. \tag{3.6}$$

Additionally, the experimental results of reference [97] can also be modeled using the following expression:

$$M(t) = M_0 + \xi \exp[-t/\tau] - \omega \ln[t], \tag{3.7}$$

combining an exponential and a logarithmic term. The authors suggest that this formulation becomes suitable due to the existence of two relaxation processes acting simultaneously.
The stretched exponential function can also fit the experimental data presented in this work, however, a model considering two relaxation processes

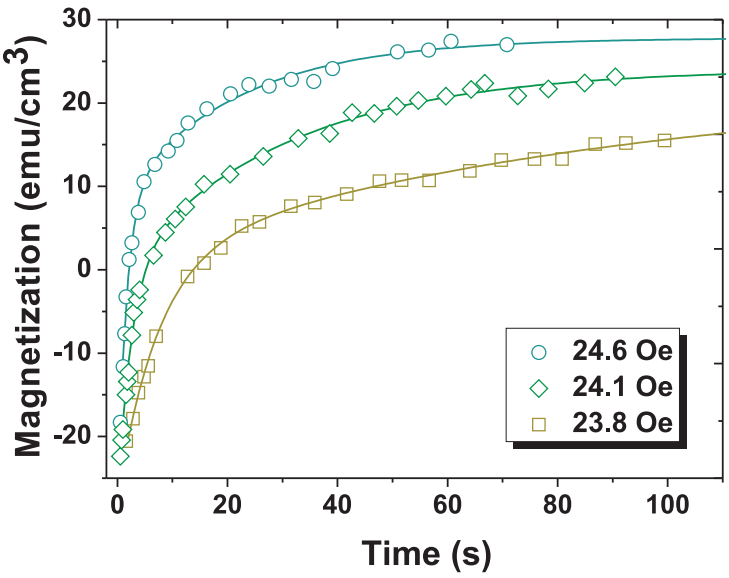

Figure 3.10: Magnetization ($\tilde{M}$) vs. time plots (sample B) for different values (23.8, 24.1, and 24.6 Oe) of the applied magnetic field and the corresponding fit curves (solid lines). The fitting was done considering two coexisting magnetic relaxation processes each one described by Eq. 4.1 with the relaxation times τ_1 and τ_2

gives an equally satisfying result. The fittings shown in Fig. 3.10 correspond to the combination of two distinct relaxation processes of the form of Eq. 3.2 with relaxation times τ_1 and τ_2. The first relaxation time describes the fast increase of *M(t)* at short time scales while τ_2 covers the slow increase for $t \gg \tau_1$.

Small additional contributions from other magnetic relaxation processes occurring simultaneously can not be excluded, but from the good agreement between fit and data it can be concluded that the aftereffect is dominated by two main relaxation processes.

According to Eq. 3.3 and 3.4 the activation volume V can be derived from the magnetic field dependence of the relaxation time at a given temperature. The logarithm of the relaxation times $\tau_1(H)$ and $\tau_2(H)$ plotted in Fig. 3.11 (a) and (b) (for samples A and B, respectively) were extracted from fittings shown in Fig. 3.10 for sample A and from those obtained in the same manner corresponding to sample B.

At this point it is worth commenting on the possibility to derive the acti-

vation volume also from the temperature dependence of the relaxation time in Eq. 3.3, a method often found in the literature [98]. Variable temperature measurements are not applicable in the case of (Ga,Mn)As in which the anisotropy energy and saturation magnetization is strongly temperature dependent. In fact a temperature dependent activation volume due to the strong changes in the magnetic anisotropy would be expected. In contrast, by measuring the magnetic field dependence of τ at a single temperature of 3 Kelvin as shown in this work most of the magnetic quantities in Eq. 3.3 remain constant.

In Fig. 3.11 the slope of the curves of $\ln[\tau_1]$ and $\ln[\tau_2]$ vs. magnetic field is then equal to $2M_S \cos(\phi)V/k_BT$ from which the activation volume can be estimated. From the field dependence of τ_1 activation volumes V_{A1} =(3.4 $\pm$ 0.2) $\times$ 10^4 nm^3 for sample A and V_{B1} =(1.5 $\pm$ 0.1) $\times$ 10^4 nm^3 for sample B are obtained. From the plot of $\ln[\tau_2]$ V_{A2} =(3.7 $\pm$ 0.7) $\times$ 10^4 nm^3 and V_{B2} =(1.6 $\pm$ 0.4) $\times$ 10^4 nm^3 are extracted for sample A and B, respectively. Comparing these values to the literature one finds that activation volumes of similar size are reported for magnetic recording materials such as barium ferrite films [99] while $3d$ metals such as nickel show more than ten times larger activation volumes [100].

Activation volumes calculated from magnetic aftereffect measurements are related to the energy barrier involved in the first elementary magnetization reversal [101]. The activation volume is the volume of material that changes magnetization as the result of going from a maximum (activated state) to a local minimum energy state by a change in the position of the domain wall. This volume is often not only related to this elementary magnetization reversal but also to the entire volume swept by the domain wall between different pinning centers called Barkhausen volume, which is closely related to the structural properties of the material [94]. On the other hand, it was stated by *P. Gaunt* [102] that in the case of strong domain wall pinning the volume swept between pinning centers (which in this model contains in average the volume associated with one additional pinning site) can not be directly related to the activation volume calculated from aftereffect measurements but is inversely proportional to the density of pinning centers. Under these conditions, the Barkhausen volume can be several orders of magnitude larger than the activation volume. In some experimental studies this distinction is clearly done by calculating the activation volume from aftereffect measurements and independently estimating the Barkhausen volume from the pinning site distribution [103].

It is important to notice that the value of the activation volume can not only be obtained by fitting of the aftereffect measurement data on long time scales. Several studies in the literature show that the value $V\Delta M/k_{\mathrm{B}}T$ can

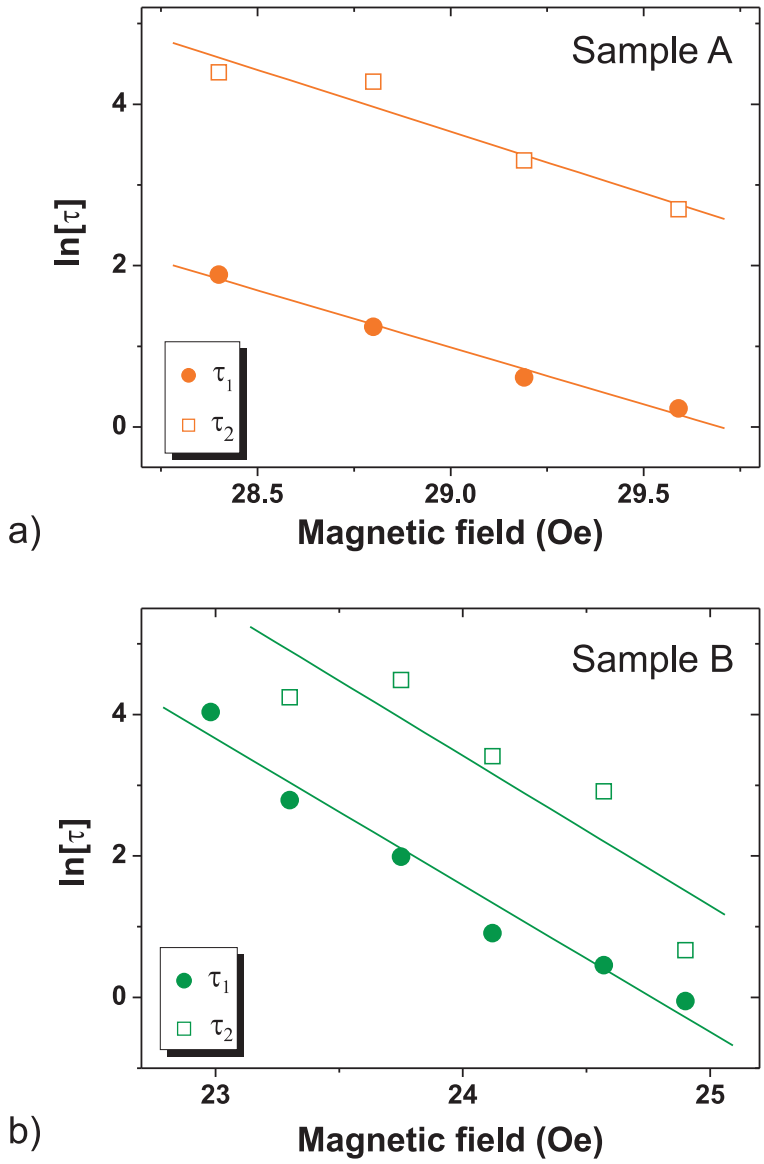

Figure 3.11: Linear dependence of $\ln[\tau(s)]$ vs. magnetic field for τ_1 (circles) and τ_2 (squares) ((a) sample A, (b) sample B). The corresponding linear fittings of the data points are shown in solid lines.

be obtained from constant domain wall velocity measurements at fields where the domain wall motion is not yet in the viscous regime but in the thermally activated depinning where the field dependence of the domain wall velocity can be described by an Arrhenius law. Measurements of a constant domain wall velocity as a function of the applied magnetic field in the Arrhenius regime lead to activation volumes which are in excellent agreement with values calculated from aftereffect measurements [104]. More specifically, these constant velocity measurements have been performed also in (Ga,Mn)As materials [105] obtaining the corresponding values for the activation volume V. In the cited (Ga,Mn)As work the authors used non-local magneto-transport measurements to monitor constant domain wall velocities at different fields. Most likely, the typical aftereffect profile present at long times scales has not been observed in the work by Tang *et al.* possibly because of both the small size of the devices used and, though still in the thermally activated depinning regime, larger magnetic fields with respect to $H_c$than those used in this study.

The order of magnitude of the activation volumes calculated in this work are comparable to results in the literature obtained by analyzing the field dependence of the constant domain wall velocity in both compressively [105] and tensile strained [106] (Ga,Mn)As. The difference of nearly a factor of 2 in the values of the activation volumes for samples A and B is attributed to the difference in the manganese concentration. Since the activation volume is a parameter closely related to the density of defects, a smaller activation volume is expected for a larger manganese concentration if each manganese center is considered as a point defect.

By analyzing the results obtained in this work and those obtained by other studies in the constant velocity regime it is evident that modeling the aftereffect signature could be of use for calculating activation volumes in a very low field range. In this case the pronounced curvature of the magnetization vs. time dependence will allow for a linear approximation to obtain the domain wall velocity vs. magnetic field curve only at very short times. Therefore, in the low magnetic field regime modeling the aftereffect over a long measurement time (providing a larger set of data points) becomes a more reliable method to calculate the activation volume than the constant velocity method.

As a closing remark for this section it is worth commenting on the possible physical interpretation of the mathematical model proposed for fitting the aftereffect signature in (Ga,Mn)As. The origin of the two relaxation processes on fast and slow time scales considered in the proposed model could be related to the different length scales of the pinning centers that can impede domain wall motion in this material. The well known structural defects

mentioned in chapter 1 created during (Ga,Mn)As growth such as interstitial manganese atoms, arsenic antisites and the substitutional manganese itself can play a role in the pinning of domain walls at the nanometer scale. However, other defects in the micrometer range such as surface imperfections can also greatly influence the domain wall dynamics. Both types of pinning centers progressively reduce the mobility of the domain wall as its area, together with the domain size, grows larger. However, approximating the distribution of pinning energies involved in these pinning events using a flat-topped distribution seems not to be the best choice considering the significant difference in the length scales where these two processes take place.
The approximation proposed in this study is based on considering two distinct independent processes that occur simultaneously and is in excellent agreement with the observed experimental data. This close correspondence between the presented mathematical model and the results of the measurements may indicate the accuracy of the proposed biexponential relaxation model in resembling the complex scenario behind the magnetic aftereffect in (Ga,Mn)As.

Chapter 4

Electrical and magnetic properties of oxygenated (Ga,Mn)As

Research in the (Ga,Mn)As scientific community has not only been focusing on the development of devices exploiting the intriguing electrical and magnetic properties of this material but also on modifying the material itself, in order to add more degrees of freedom for controlling the magnetoelectric properties of (Ga,Mn)As. In this respect, a substantial improvement in view of practical applications was the achievement of higher Curie temperatures upon low temperature annealing as described in chapter 1. On the other hand, methods allowing for the controlled suppression of ferromagnetism [107,108] have been developed and can be important for devices where a local modification of the magnetic properties is required.
In this chapter the post-growth tunability of the properties of (Ga,Mn)As is in the focus. Unlike in the previous chapter where the magnetic properties of pure (Ga,Mn)As were studied, in this part of the thesis both the magnetic and electrical properties of modified (Ga,Mn)As materials are probed. The modification in this case consists in the suppression of the ferromagnetic interaction by inclusion of oxygen species into the lattice by means of exposure to an oxygen plasma. The general observation after the plasma treatment is a weaker ferromagnetic coupling where the Curie temperature (T_c) shifts to lower values and the coercive field increases indicating a reduction in the value of the magnetization.
The plasma treatment will be described in the following together with its effects on the magnetic and transport properties of (Ga,Mn)As observed by various experimental techniques.

4.1 Oxygen incorporation into (Ga,Mn)As

The starting point of these oxygenation experiments is the oxygen plasma treatment of the (Ga,Mn)As films. The manganese concentrations of the samples employed, designated A and B, are 1.2 and 3 % with thicknesses of 170 nm and 40 nm, respectively. Magneto-transport measurements have been carried out using 30 μm wide Hall bar devices.
The plasma treatment was performed using a microwave (2450 MHz) TePla 100-E oxygen plasma system. Because of the use of microwaves, this plasma system reduces the surface charging to the minimum during the exposure with respect to radio frequency plasma systems used for instance in hydrogenation experiments [108]. Under these conditions of minimum charging there is only a negligible acceleration of ions towards the surface which prevents undesired surface bombardment [109] leaving the films less damaged by the treatment. The first step in the treatment is placing the sample inside a vacuum chamber that is later evacuated to reach a pressure of approximately 0.1 mbar. Subsequently oxygen gas is let inside the chamber with a final pressure of 1 mbar. Finally the plasma is activated (it takes approximately 2 seconds for the full development of the plasma) with an input power of 300 W. The results shown in this study were obtained from oxygenated samples with an exposure time of 3 hours.
Due to the high sensitivity of the (Ga,Mn)As materials to temperatures higher than that used during the epitaxial growth the sample temperature needs to be carefully monitored inside the plasma chamber. High temperature exposure may lead to the formation of MnAs clusters [110] that can significantly alter the magnetic and transport properties of (Ga,Mn)As. The highest temperature detected during the 3 hours plasma exposure was of 177°C, well below the growth temperature of 260 °C and 270 °C for samples A and B, respectively. This ensures that the effects observed are to be attributed to the incorporation of oxygen into the lattice and not to the deterioration of the (Ga,Mn)As films.
In the following the necessary characterization of the (Ga,Mn)As films after treatment will be presented. The incorporation of oxygen will be shown by means of X-ray photoelectron spectroscopy.

4.1.1 Depth profile X-ray photoelectron spectroscopy

Prior to the presentation and discussion of the results obtained the most important concepts of X-ray photoelectron spectroscopy (XPS) are introduced. In XPS the sample to be analyzed is kept in ultra high vacuum conditions and is irradiated with X-rays while detecting the kinetic energy of the electrons

escaping from the first few nanometers of the material [111] with an electron energy analyzer. This technique is suitable and particularly powerful for evaluating electron binding energies of individual elements in a compound. In the present case, the element selectivity provided by this technique will be employed to elucidate the extent of oxygen incorporation into the (Ga,Mn)As layers.

In order to analyze the oxygen content in the oxygenated (Ga,Mn)As films the element selectivity is fundamental but not the only requirement. Additionally, it is of major importance to access the oxygen content not only on the surface of the films but also on the subsequent layers of material that compose the full volume of the sample. To obtain this information XPS spectra need to be taken after subsequent removal of small portions of the material. In this way a depth profile of the oxygen content was acquired by recording the O $1s$ XPS spectrum between steps of sputtering with Ar^+ ions accelerated at a voltage of 4kV with an etching rate of 4.5 nm per minute (calibrated with a GaAs film).

The depth profile of the X-ray photoelectron spectra (XPS) of sample A showing the oxygen content as a function of the distance from the surface for the as-grown (top) and oxygenated (bottom) samples is shown in Fig. 4.1. The oxygen content is represented as the peak area of the background substracted O $1s$ peak in counts per second (CPS) shown in the insets. The presence of oxygen can be already detected in the as grown sample consistently with studies in the literature which report the formation of a manganese rich surface oxide on (Ga,Mn)As exposed to air which has been identified to be MnO [112]. Additionally, Ga and As oxides known to form at the surface of GaAs materials in contact with air also contribute to the oxygen signal in (Ga,Mn)As films [113]. Although the surface oxide layer thickness in (Ga,Mn)As is reported to be between 1 and 2 nm [113, 114], in our experiments oxygen can still be detected up to $\sim$20 nm along the growth direction. Most likely, this is due to the inter-diffusion of O atoms from the surface into the structure assisted by the sputtering procedure.

In the as-grown sample the maximum oxygen intensity is found at the surface as expected. After the oxygenation treatment a peak in the oxygen intensity is observed at $\sim$17 nm and is a factor of 2 higher than that of the oxygen on the surface of the as-grown sample. Going deeper into the sample the O intensity drops to zero at approximately 60 nm. Such a depth profile of the oxygen intensity in the plasma treated sample reflects the energy distribution of the oxygen species penetrating into the structure of the films. Oxygen species with relatively low energies will be confined to regions of the sample closer to the surface while those with larger kinetic energies are expected to penetrate further into the structure. As already mentioned, the peak value

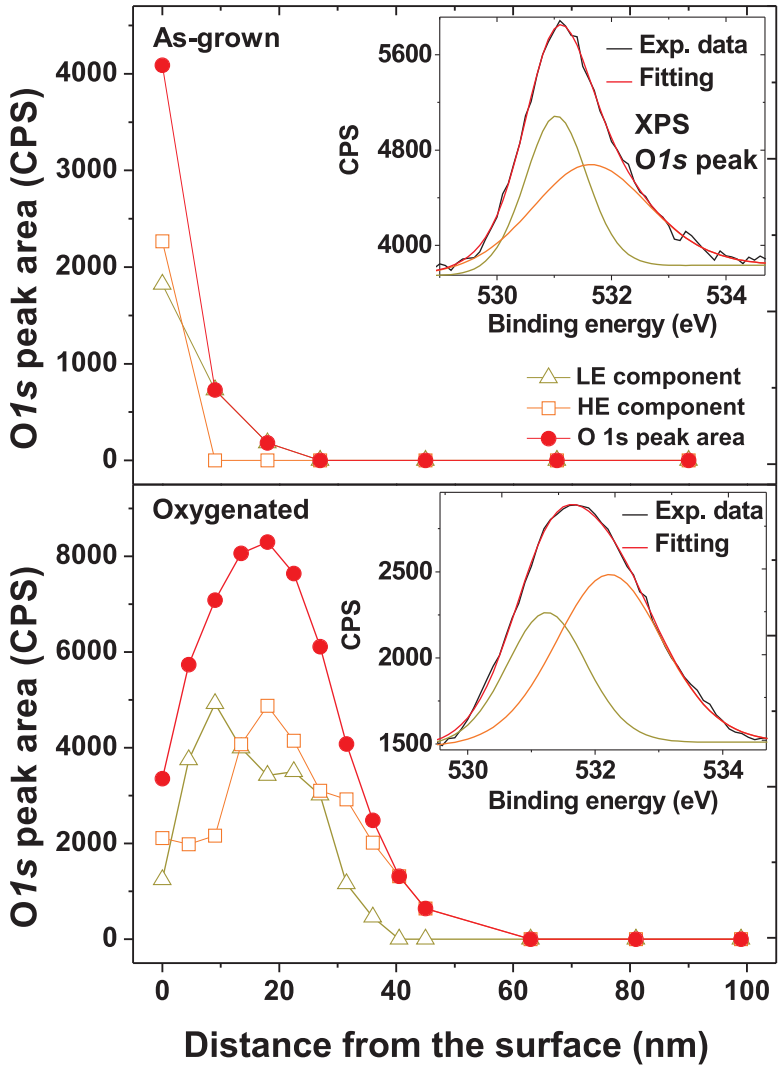

Figure 4.1: Depth profile of the oxygen 1*s* peak measured by XPS. The oxygen intensity in the as grown sample (top) is largest at the surface and vanishes at 20 nm. The oxygenated sample (bottom) has the largest oxygen intensity at 17 nm from the surface and it reduces to zero at approximately 60 nm. The insets display the oxygen 1*s* peak at the surface of the as-grown (top) and oxygenated (bottom) samples where two contributions at higher (squares) and lower (triangles) energies are combined in the fitting to give the total peak area.

of the oxygen content is twice as high in the treated sample compared to the surface value of the as-grown sample. However, the total amount of oxygen contained in the whole sample volume expressed as the area under the depth profile curves presented in Fig. 4.1 (O1s peak area (CPS) vs. distance from the surface (nm)) is almost ten times higher after oxygenation. This significant increase in the oxygen intensity leads to the observed distinct changes in the electrical and magnetic properties that will be introduced later in this chapter.

The XPS oxygen 1s peaks of the as-grown and oxygenated samples at the surface of the films are displayed in the insets of Fig. 4.1 (top) and (bottom), respectively. Fitting of the O 1s signal requires considering two contributions (70% Gaussian-30% Lorentzian peaks) to the total area of the peak which are centered around different energies. By modeling the XPS lineshape the higher and lower energy contributions can be traced in the depth profile shown in Fig. 4.1. In the case of the as-grown sample, the high energy peak can only be found in the vicinity of the surface while for the oxygenated sample a similar contribution from the high and low energy peaks is observed also inside the film in the region of highest oxygen content. The decomposition of the XPS O 1s lineshape into two components has been already reported in the literature for the case of oxygen adsorption on GaAs [115]. The authors propose that the higher energy component may correspond to a less tightly chemisorbed type of oxygen. Additionally, the authors present evidence supporting the idea of dissociated oxygen being the species represented by the lower energy peak. As previously mentioned the high and low energy contributions are comparable in the oxygen rich parts of the oxygenated samples. In the present case the diffusion of dissociated oxygen into the structure of the films seems to be a reasonable scenario. On the other hand, as mentioned in the previous chapter, (Ga,Mn)As is known to have energetically different interstitial sites where the energy is determined by the coordination of the interstitial atom to the neighbouring atoms in the lattice. In (Ga,Mn)As there are two inequivalent tetrahedral positions surrounded by four As or Ga atoms, respectively, and one with hexagonal symmetry. However, the tetrahedral sites are strongly preferred over the hexagonal sites by the manganese atoms sitting in interstitial positions [90, 91]. In view of these facts, we tend to attribute the high and low energy contributions to the total content in the oxygenated samples to dissociated oxygen species sitting in differently coordinated interstitial sites inside the lattice of the (Ga,Mn)As films.

In the next section the effects of the oxygen incorporation discussed in the last paragraphs will be analyzed. These changes will be sensed by observing the changes in the magnetic and electrical properties of the oxygenated (Ga,Mn)As films with respect to the untreated samples.

4.2 Magnetism and electrical transport in oxygenated (Ga,Mn)As

As mentioned in previous discussions the transport characteristics of (Ga,Mn)As can give information both about the electrical and magnetic properties. Exploiting this fact, the temperature dependence of the resistance and angle dependent coercivity measurements are presented in order to evaluate in this case the effects of the oxygenation treatment. In addition to this another technique is employed to analyze in further detail the influence of the oxygenation on the magnetic properties. This technique is X-ray absorption spectroscopy and a short review on the basic concepts it is based on together with the experimental results obtained is presented in the following.

4.2.1 X-ray absorption spectroscopy

According to chapter 1 the magnetic properties of (Ga,Mn)As can be manipulated by changing the density of magnetic moments and by changing the hole carrier density. In this section, the magnetic properties of the (Ga,Mn)As films after the oxygenation treatment will be analyzed in terms of the effects produced on the magnetic moments provided by the Mn atoms.
This information was obtained by means of X-ray absorption spectroscopy. This powerful technique is highly suited for the determination of the electronic structure of materials. However, intense X-ray beams are needed for this purpose, therefore the experiments need to be carried out in a synchrotron radiation facility which is in our case the Berliner Elektronen-Speicherring Gesellschaft für Synchrotronstrahlung (BESSY). The X-ray radiation excites core level electrons and the type of spectrum, or so-called edge, receives a name according to the principal quantum number (n) of the electron that is excited. In this way, the excitation of $1s$ electrons can be found in the K-edge while the L-edge can give information about the excitation of $2p$ electrons. The analysis of the L-edge is particulary interesting for the study of magnetic interactions since it allows transitions from the $2p$ levels to unoccupied d states and contains the information about the magnetic properties of the material [116].
In Fig. 4.2 (top) and (bottom) the Mn L_2 and L_3 edges and the oxygen K edge X-ray absorption spectra (XAS) for as-grown and oxygenated film A are presented. The splitting of the L edge into L_3 and L_2 peaks is due to the spin-orbit splitting of the initial $2p$ levels. The spectra were taken after sputtering the samples for 5 minutes following reference [117] at a rate of approximately 1ML/min. In the Mn spectra no mayor differences upon oxygenation are ob-

served apart from the reduction of the intensity of the low energy shoulder of the L_3 peak at 640 eV. The decrease in intensity of this particular feature has been already observed in (Ga,Mn)As after annealing [118] and therefore is unrelated to the oxygenation treatment and only accounts for a small annealing effect due to the enhanced temperature of 177°C during plasma treatment. It is important to notice that even though a mild annealing effect could be expected in the electrical and magnetic properties of the films, this is in the present case negligible. The effect of annealing as mentioned in chapter 1 would produce a strengthening of the magnetic interaction and the effect of oxygenation, as mentioned, causes the opposite effect. In this way if any changes occur due to annealing these are widely obscured by the oxygenation process.

Taking these considerations into account, the spectra before and after the treatment show the typical lineshape corresponding to a d^5 electronic state of Mn [118] indicating no mayor changes in the electronic configuration of the Mn magnetic centers during oxygenation. However, such a good correspondence between the as-grown and oxygenated samples is not observed in the oxygen K edge spectra. It can be seen in Fig. 4.2 (bottom) how the profile changes dramatically after the plasma treatment.

A similar XAS profile to the one presented in Fig. 4.2 (bottom) for the as-grown sample has been reported in the literature for other (Ga,Mn)As materials and has been attributed to MnO forming on the surface of (Ga,Mn)As [112]. The spectrum shows a single broad structure centered approximately around 537 eV as the result of the superposition of multiple peaks laying close in energy. The XAS signal corresponding to the oxygenated sample consists of a broad peak (540 eV) and a feature at lower energies (532 eV). According to studies of manganese oxides in the literature the energy range corresponding to the O K edge involves transitions from the O $1s$ level to excited levels of O $2p$ character hybridized with the Mn $3d$ and $4sp$ states at lower and higher energies, respectively. The O $2p$-Mn $3d$ states have predominantly Mn character while the O $2p$-Mn $4sp$ states are more related to the oxygen $2p$ orbitals [119–122].

The scenario in the present case is more complex than that of pure manganese oxides since in (Ga,Mn)As samples the manganese atoms are quite diluted and the oxygen atoms will not only interact with the magnetic centers but also with the gallium and arsenic atoms. However, the strong change in the oxygen K edge spectra measured before and after the plasma exposure indicates a significant change in the electronic state of the oxygen species. The change in the electronic state of the oxygen after the treatment is most likely due to a different coordination with respect to that existing in the MnO and As or Ga surface oxides. Considering that the additional oxygen present in

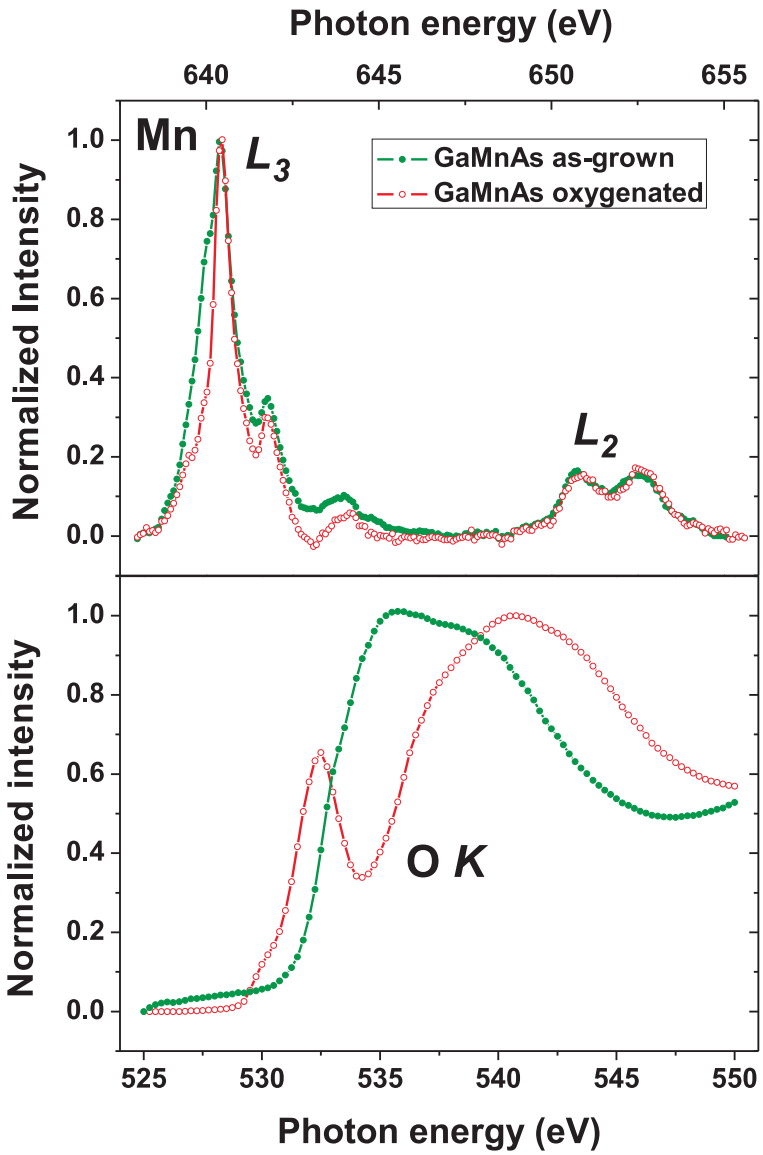

Figure 4.2: Normalized XAS spectra of the Mn $L_{2,3}$ edges (top) and the oxygen K edge (bottom) for the as-grown (green symbols) and oxygenated (red symbols) (Ga,Mn)As samples. The normalization was done at the respective peak intensities. While the Mn d^5 electronic state is preserved upon oxygenation the type of oxygen present in the oxygenated sample is clearly different from that of the surface oxide of the as-grown sample.

the oxygenated samples diffuses from the plasma into the (Ga,Mn)As lattice it is realistic to propose that the plasma-incorporated oxygen species are sitting in interstitial sites. Thus, keeping in mind the mechanism of the oxygen incorporation it could be intuitively argued that the species that will most easily diffuse into the material will be those uncharged, namely atomic oxygen. This last argument suggests that the incorporated oxygen species might have a different oxidation state (O^0) with respect to that in the MnO surface oxide (O^{2-}) which in combination with a different coordination given by the chemical environment of the (Ga,Mn)As interstitial sites as shown earlier by XPS gives rise to the changes observed in the XAS profile.
By means of the analysis of the XAS spectra we can draw the important conclusion that the magnetic moments in oxygenated (Ga,Mn)As are quite unaffected by the treatment. Thus, the changes in the magnetic properties in (Ga,Mn)As that are analyzed in the following are attributed to changes in the hole carrier density. In the upcoming section, magnetic field angle and temperature dependent transport measurements of as-grown and oxygenated samples are presented and analyzed in detail.

4.2.2 Magneto-transport

Magneto-transport measurements were performed using Hall bar devices 30 μm wide patterned on sample B where the thickness of the magnetic film is 40 nm. According to the depth profile presented in Fig. 4.1 this thickness range contains exactly the part enriched with oxygen and therefore we expect to observe the largest possible effect of the plasma treatment for an oxygenation time of three hours.

In Fig. 4.3 (top) the resistance vs. temperature plots of the as-grown and oxygenated samples are displayed. Recalling the concepts mentioned in chapter 2, the maximum in the resistance vs. temperature plot due to critical spin disorder can be used to trace the value of the ferromagnetic transition temperature. Indeed, a clear shift of the resistance peak of the oxygenated sample with respect to the untreated one can be observed which indicates a decrease of the Curie temperature by about 30% from 45 to 32 Kelvin together with a large increase in the values of resistance at all temperatures. In Fig. 4.3 (bottom) the effects of oxygenation can be seen in the coercive field dependence on the angle of the applied in-plane magnetic field with respect to the [110] uniaxial easy axis direction. A significant increase in the coercive fields in all directions is observed for the oxygenated sample with respect to the as-grown material. Considering the following expression for

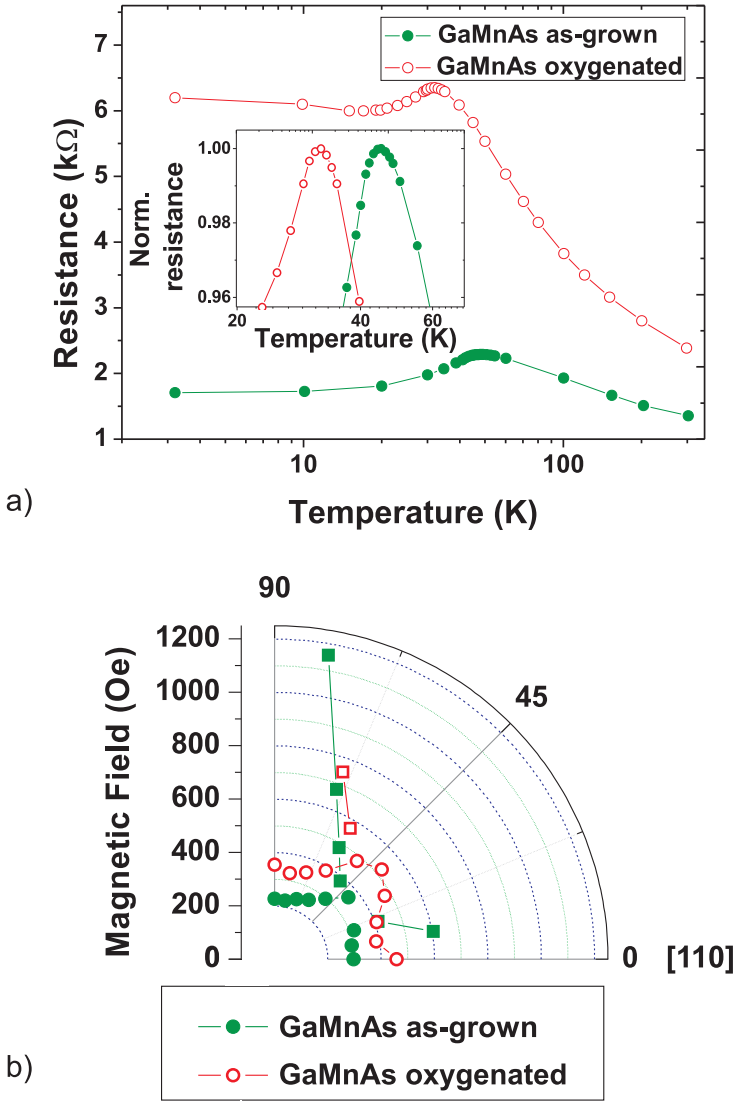

Figure 4.3: (top) Resistance vs. temperature for as-grown (full symbols) and oxygenated (open symbols) (Ga,Mn)As samples. A zoom-in of the resistance peaks is shown in the inset. (bottom) First (circles) and second (squares) coercive fields as a function of the orientation of the magnetic field with respect to the [110] direction.

the domain wall pinning energy density (ϵ) [54]

$$\epsilon = (\mathbf{M}_2 - \mathbf{M}_1) \cdot \mathbf{H}_c, \tag{4.1}$$

where $\mathbf{M}_1$ and $\mathbf{M}_2$ are the initial and final magnetization vectors involved in the magnetization reversal and $\mathbf{H}_c$ is the coercive field, it can be concluded that the increase in coercivity can be due to a decrease in the value of M assuming ϵ constant. This assumption is made considering the close relation between the value of ϵ and the magnetic anisotropy. As mentioned in the last chapter, the mathematical expression given for ϵ can be used to fit the angle dependence of the coercive field and is therefore clearly linked to the degree of deviation from pure biaxial anisotropy due to the presence of the uniaxial contribution. In this case, the qualitative rectangular shape of the angle dependent coercivity plot in Fig. 4.3 has not changed after oxygenation, indicating a rather constant relation between the magnetic uniaxial and cubic anisotropy energies. From this we conclude that the domain wall pinning energy density ϵ remains fairly constant. In particular, the ratio of approximately 1.2 between the coercivities along the uniaxial easy axis (0°, [110] direction) and the uniaxial hard axis (90°, [1$\bar{1}$0] direction) observed for the as-grown sample is also found after the oxygenation treatment regardless of the overall increase in the values of the coercive fields. Thus, the increase in coercivity can be attributed to a decrease in magnetization in agreement with the idea of a ferromagnetic interaction that is in average weaker, extracted from the shift of T_c to lower temperatures.
As previously mentioned, the Mn L_2 and L_3 edges show the typical Mn d^5 lineshape for both as-grown and oxygenated samples indicating that the local magnetic moments at the Mn sites can be considered constant. Again this points towards a weakening of the coupling between them which leads to the observed decreased magnetization. On the other hand, it was discussed that the oxygen introduced by the treatment is thought to be neutral and possibly sitting in interstitial positions.

Theoretical studies in the literature analyzing oxygen impurities in GaAs show that neutral oxygen sitting in interstitial sites is one of the stable configurations in pure and p/n-doped GaAs [123]. The cited work shows that interstitial oxygen atoms introduce fully occupied states close to the top of the valence band as shown in the diagram in Fig. 4.4. According to the theory of hole mediated ferromagnetism [35] discussed in chapter 1, the magnetic properties in (Ga,Mn)As are strongly related to the hole density close to the valence band edge. A decrease in charge carrier concentration is predicted to cause a weakening of the ferromagnetic coupling which has been widely confirmed by experiments [124,131]. Therefore, in the present case the weakening of the ferromagnetic coupling is attributed to a decrease in the hole

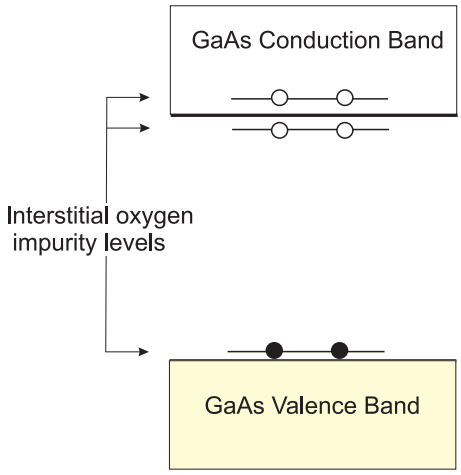

Figure 4.4: Diagram of the electronic energy levels introduced by a neutral oxygen impurity sitting in an interstitial site in GaAs relative to the valence and conduction band edges(adapted from *Orellana et al.* [123]).

density. Considering that neutral oxygen sitting in interstitial positions is a good picture of the structure of the (Ga,Mn)As samples after treatment the weakening of the ferromagnetic coupling is attributed to hole compensation by electrons from the occupied states of the interstitial oxygen atoms that lay close to the top of the valence band. This scenario also fits very well with the large increase in the resistance upon oxygenation.
In conclusion, the magnetic properties of (Ga,Mn)As have been strongly modified by exposure to an oxygen plasma. XAS measurements indicate that the occupation of the $3d$ levels of the Mn atoms remains unchanged upon oxygenation whereas the O K edge signal shows drastic changes with respect to the signal for the as-grown sample. The magneto-transport measurements show a significant decrease in the strength of the ferromagnetic coupling reflected in a reduction of T_c by 30% and an increase of the coercive field. According to XAS data, the mechanism behind the weaker ferromagnetic properties after treatment is not related to a reduction in the local Mn magnetic moments but is a consequence of a modulation of the hole density manifested in an increase in the zero-field resistance at all temperatures which depends on the density of the oxygen interstitial atoms.
The oxygenation treatment of (Ga,Mn)As presented in this work can be applied to large areas of a film. Using this oxygenation procedure, the local modification of the magnetic properties in specific locations becomes possible. This approach can be exploited to create structures allowing for the

controlled launching of domain walls in single-domain devices. Moreover, by this method these domain nucleation units could be generated in multiple and clearly defined locations at a time by the use of a suitable mask which is important for practical applications.

Chapter 5

Optical-gating of photo-sensitized (Ga,Mn)As

In this final chapter of the thesis the idea of studying the properties of modified versions of (Ga,Mn)As, as done with oxygenated materials in the previous chapter, will be further developed. The approach in this case, in contrast to the oxygenation experiment, is not linked to the modification of the chemical composition of the (Ga,Mn)As films but only to a surface treatment. To complement and compare the results obtained for the oxygenation process presented in the previous chapter, where the treatment modifies the chemical composition of the entire volume of the sample, the effects of surface functionalization will be now explored in detail.
The method used in the experiments presented in the following is the interaction of (Ga,Mn)As with various adsorbates. As will be shown, the effects observed in the magnetic and electrical properties are remarkable and on the order of what was found for oxygenation, where the chemical composition of the entire volume of the sample is modified. The initial success in manipulating the electrical and magnetic properties of (Ga,Mn)As by the interaction with adsorbates offered the possibility of working with selected adsorbates that can provide new functionalities to (Ga,Mn)As. This idea took form in the photo-sensitization of (Ga,Mn)As by bringing light sensitive molecules on the surface. In this way, the interaction with adsorbates is not only restricted to static charge-transfer or dipolar effects but can be also light regulated. The result is a proof of principle for the light control of the electrical and magnetic properties in organic-dye/GaMnAs structures.
In the following a description of the experimental details of the functionalization of (Ga,Mn)As will be given. In a second part, the study of the adsorbate-(Ga,Mn)As interaction in the absence of light will be presented. Lastly, the light effects on the properties of photo-sensitized (Ga,Mn)As will

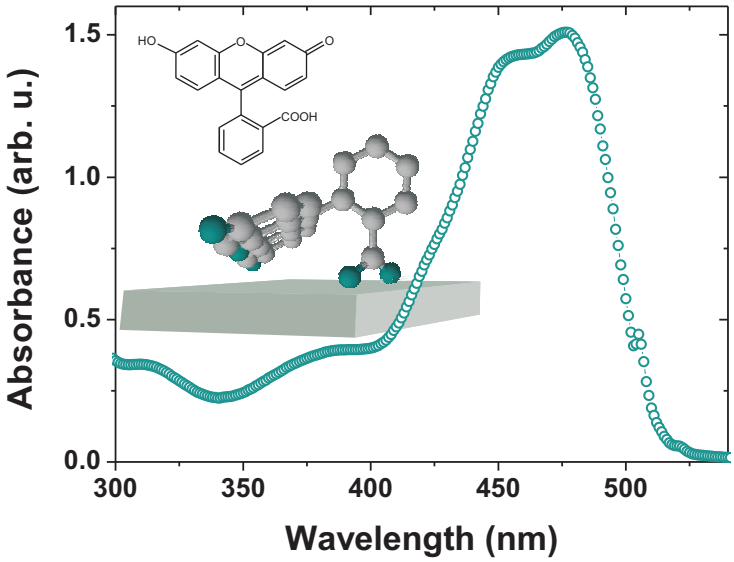

Figure 5.1: Ultraviolet-Visible absorption spectrum of the fluorescein dye molecule solution used for the (Ga,Mn)As modification. The molecule structure and a tentative adsorption geometry involving an interaction between the carboxylic group and the surface are also schematized (carbon atoms are colored grey and oxygen atoms green).

be addressed.

5.1 Functionalization of (Ga,Mn)As

The as-grown (Ga,Mn)As films used in this study will be once again designated as A and B. Sample A has a Mn concentration of 8% a thickness of 50 nm and a Curie temperature of 68 Kelvin. The respective properties for sample B are 3%, 40 nm and 45 Kelvin. The same Hall Bar devices employed for oxygenation experiments were also used here. After lithography, the resulting Hall structures were contacted and transport properties were measured before and after the adsorption of fluorescein.

The adsorption of the molecular layers was accomplished by simply immersing the (Ga,Mn)As films in a solution of the commercially available fluorescein dye. This solution is prepared by dissolving the powder of the free acid form of fluorescein in water to reach a final concentration of 2mM at room temperature and then adjusting the pH to 7 with a diluted solution of NaOH. Prior to the immersion in the dye solution the (Ga,Mn)As

films are treated with an HF containing etch mixture for approximately 10 seconds to clean the surface and remove the native surface oxide. The etch mixture consists of a 1:10 dilution in water of the commercial etch mixture AF 87.5-12.5 VLSI Selectipur. After HF treatment the samples are rinsed in purified water and thereafter immediately placed in the molecule solution for about 12 hours. Finally, the samples are rinsed in water to remove most of the non-chemisorbed species and are left to dry in air at room temperature and protected from visible light. Magneto-transport measurements performed before and after the HF treatment confirm that the etching procedure does not modify the properties of the (Ga,Mn)As films. These control experiments indicate that the amount of material etched is not comparable to the total thickness of the layer since no significant changes are observed in the value of the electrical resistance. The light source employed in the illumination experiments is a commercial HBO mercury lamp with a spot diameter of approximately 1 mm that covers the entire Hall bar structures. No light-induced effects have been observed in the magneto-transport of the as grown (Ga,Mn)As films under illumination.
The Ultraviolet-Visible absorption spectrum of the fluorescein solution is governed by the main absorption peaks occurring at wavelengths of 476 and 452 nm as shown in Fig. 5.1. This absorption profile will most likely be modified upon interaction with the (Ga,Mn)As surface but it is useful for estimating the absorption of the adsorbed molecules. The light source employed has one of its most strong emission lines at 436 nm that, according to the Ultraviolet-visible spectrum, is probably responsible for the excitation of the fluorescein molecules.
The chemical structure and tentative adsorption geometry of fluorescein is also schematized in Fig. 5.1. The dye molecule is thought to interact with the surface of the (Ga,Mn)As films mainly via the carboxylic group as proposed in the literature for the chemisorption of carboxyl-terminated molecules on GaAs/GaMnAs heterostructures [126] and for the adsorption of fluorescein and other aromatic acids on semi-insulating and metallic surfaces [127].

5.2 GaMnAs/organic-dye system in the absence of light

In this section the effects of the surface functionalization of (Ga,Mn)As will be presented. The changes in the magnetic and transport properties observed after the adsorption of fluorescein will be compared to the adsorption of other

similar molecular species. Finally, the effects of fluorescein will be analyzed in terms of the changes in electrical resistance and magnetic anisotropy.

5.2.1 Fluorescein on (Ga,Mn)As

Before addressing the changes in the magnetic and electrical transport properties of (Ga,Mn)As upon adsorption of fluorescein let us briefly discuss the interaction between the adsorbate and the surface.

The X-ray photoelectron specta (XPS) of sample A before and after fluorescein adsorption are shown in Fig. 5.1 (top) and (bottom), respectively. In the as-grown sample the dominating feature is the Ga 3d peak (19.6 eV) and a shoulder towards higher binding energies (21.3 eV) accounting for the presence of gallium oxide [128]. In order to identify all the contributions from surface oxides to the XPS spectra the as-grown sample has been measured with the surface oxide layer (Fig. 5.1 (top)) and after sputtering. All the features presented in the spectrum of Fig. 5.1 (top) are unchanged after sputtering except for the shoulder at 21.3 eV that as previously mentioned corresponds to gallium oxide and consistently disappears.

The mayor changes in the spectra related to the adsorption of the molecule occur at lower binding energies with respect to the Ga 3d peak, corresponding to the valence band states in bulk GaAs(001) [129] and by analogy also to the valence band of its p-doped variant (Ga,Mn)As. A distinct increase in the intensity of the existing peaks (around 7.3eV and 3.4 eV) relative to the Ga 3d peak and the observation of new features (at 5.7 and 4.9 eV) indicate the presence of occupied electronic levels in the energy range of the (Ga,Mn)As valence band states upon adsorption of fluorescein. The existence of populated levels at these relatively low binding energies could point at an effective hole quenching in the (Ga,Mn)As substrate that according to the theory of hole mediated ferromagnetism [35] would lead to the weakening of the ferromagnetic interaction.

It is important to mention at this point that the intensity of the XPS spectrum of the GaMnAs/fluorescein sample is approximately one order of magnitude smaller than that of the untreated sample. The escape depth of the photoelectrons that contribute to the XPS signal is approximately 2 nm and the dimensions of the adsorbed molecules in the proposed geometry is approximately 5 $\mathring{A}$. In view of these facts it is most probable that the reduction in intensity of the XPS signal is due to the presence of a multilayer of molecules. However, considering the small electron escape depth, an upper limit for the thickness of this multilayer can be proposed. The presence of 4 layers of molecules should already completely obscure the signal from the underlying (Ga,Mn)As, therefore, the multilayer is most probably composed

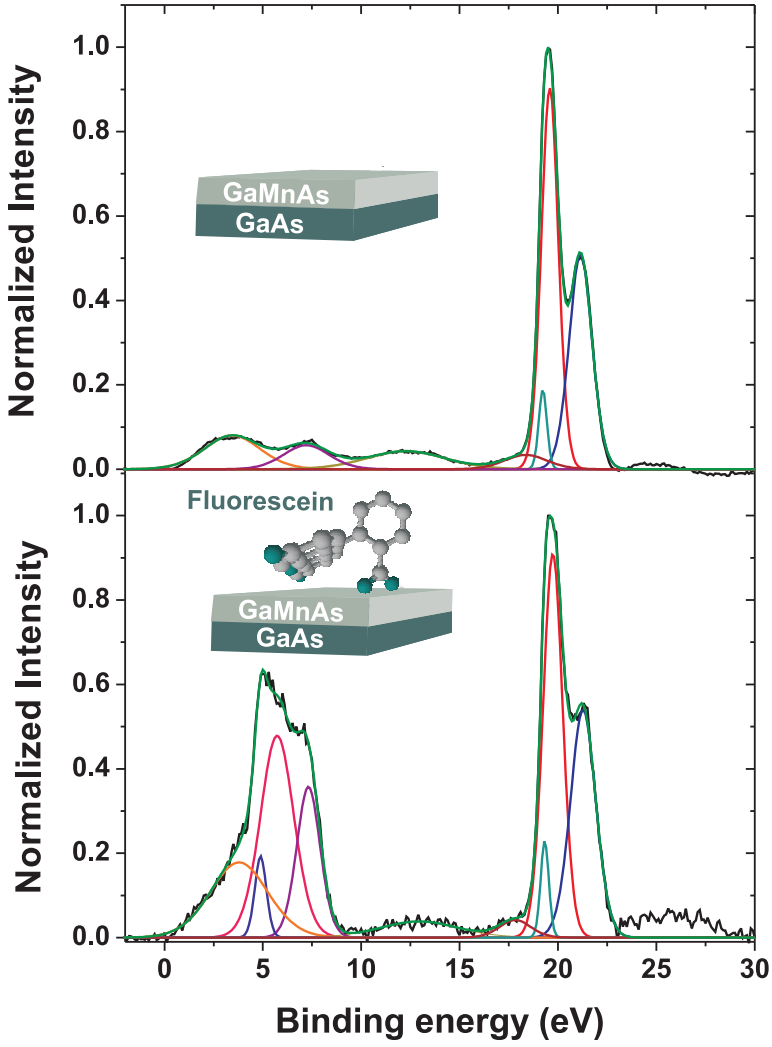

Figure 5.2: Normalized XPS spectra of the Ga 3d peak and the (Ga,Mn)As valence band before (top) and after (bottom) adsorption of fluorescein. A distinct feature composed of several peaks (see text) centered around 5 eV appears in spectrum (bottom) indicating the appearance of occupied electronic levels in the energy range of the (Ga,Mn)As valence band states upon adsorption of the molecule.

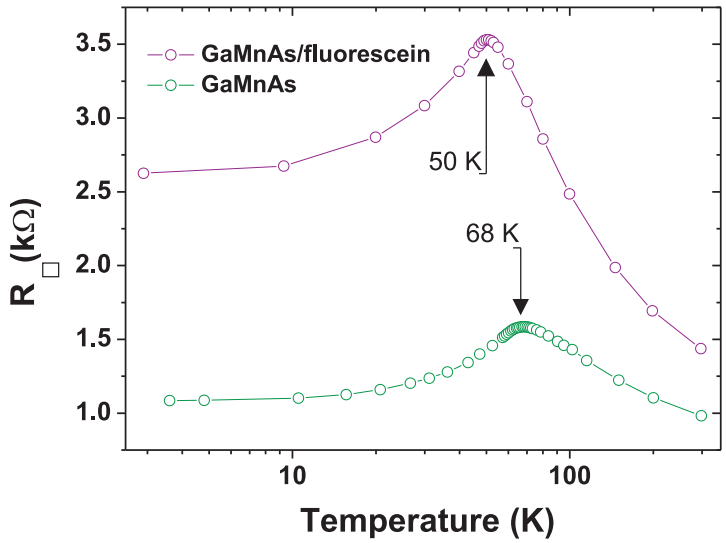

Figure 5.3: Sheet resistance vs. temperature for the as grown (Ga,Mn)As film A and its corresponding GaMnAs/fluorescein system. An increase in the electrical resistance and a shift of the resistance maximum 18 K towards lower temperatures is observed upon adsorption of the fluorescein dye.

of more than one but less than four layers.

The best way to evaluate a potential quenching of the hole charge carriers is to evaluate the transport properties of the GaMnAs/Fluorescein films. In Fig. 5.3 the temperature dependence of the sheet resistance, defined as the resistivity divided by the film thickness, of sample A is presented. A clear increase in the value of the electrical resistance at all temperatures together with a shift of the resistance maximum 18 K towards lower temperatures is observed after fluorescein adsorption. This behaviour is in close correspondence with the idea of having a depletion of the electric charge carriers extracted from the analysis of the XPS data. The combination of a higher resistance together with a lower Curie temperature (given by the position of the resistance peak) strongly points to a hole quenching mechanism due to the interaction of the molecules with the (Ga,Mn)As films. In the following, let us briefly discuss this correlation within the mean field approximation.
As mentioned in the introduction, using the mean field theory approximation a very useful relation between the ferromagnetic transition temperature and the charge carrier concentration (p) can be obtained [5]:

$$T_c \propto p^{1/3}. \tag{5.1}$$

In the proportionality factor the manganese concentration is included, however for the present case this parameter remains unchanged by the surface functionalization. This expression allows for the estimation of the changes in the charge carrier density upon adsorption of the molecular species by comparing the values of the Curie temperatures before and after the fluorescein treatment. The ratio between the Curie temperatures of the as-grown and treated samples is 68 K/50 K = 1.36. This implies that the carrier density is depleted by $\sim$ 26 % after the adsorption of fluorescein with respect to the as-grown sample. Following the expression in Eq. 5.1, it is useful to compare the ratio of the Curie temperature values with those of the charge carrier concentration dependent resistances. Assuming that the electrical resistance is inversely proportional to the charge carrier density a cubic root of the ratio of the sheet resistances at the lowest measurement temperature (3 Kelvin) can be readily compared to the T_c ratio. It is found that this ratio amounts to 1.35 which is in excellent agreement with the Curie temperature relation. In conclusion, it is possible to show not only that the interaction of adsorbates with (Ga,Mn)As effectively quenches hole carriers but also that this quenching is in agreement with the mean field model of hole mediated ferromagnetism in (Ga,Mn)As.

5.2.2 Effect of the electronegativity of the adsorbates' substituents

A hole quenching mechanism was identified as the source of the changes observed in the magnetic and electrical properties of (Ga,Mn)As upon adsorption of fluorescein. In the following the analysis of the hole quenching mechanism will be extended by considering the interaction of (Ga,Mn)As with different adsorbates.

In Fig. 5.4 the temperature dependence of the electrical resistance and the position of the resistance peak (inset) is shown for the interaction between (Ga,Mn)As (sample B) and fluorescein derivatives. In line with the picture of a hole compensation mechanism derived from the results presented in the last section an increase in the electrical sheet resistance and a shift of the resistance peak towards lower temperatures is observed for all the molecules, fluorescein producing the largest effect. The two fluorescein derivatives investigated are eosin Y (diamonds) and phloxine B (squares) which differ from fluorescein by additional electronegative bromide and chlorine groups as indicated in the molecular structure shown in Fig. 5.4. If the molecules are thought to act as electron donors, the presence of electronegative groups is expected to hinder the hole quenching capability of the molecule and is

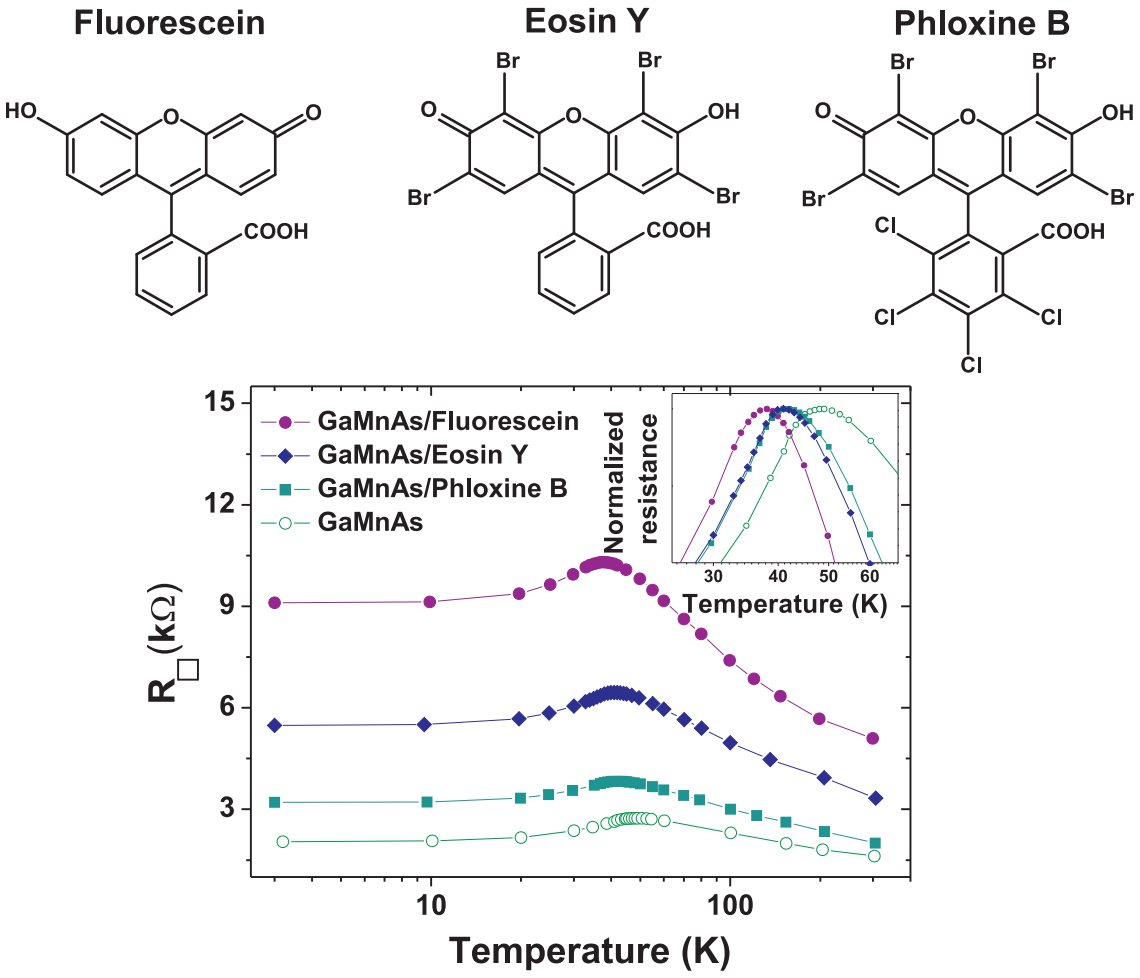

Figure 5.4: Effect of fluorescein and its derivatives eosin Y and phloxine B on the magnetic and electrical properties of sample B. The introduction of electronegative groups in the structure of the molecules reduces the hole quenching capability resulting in a smaller shift in T_c and a reduced increase in electrical resistance with respect to fluorescein.

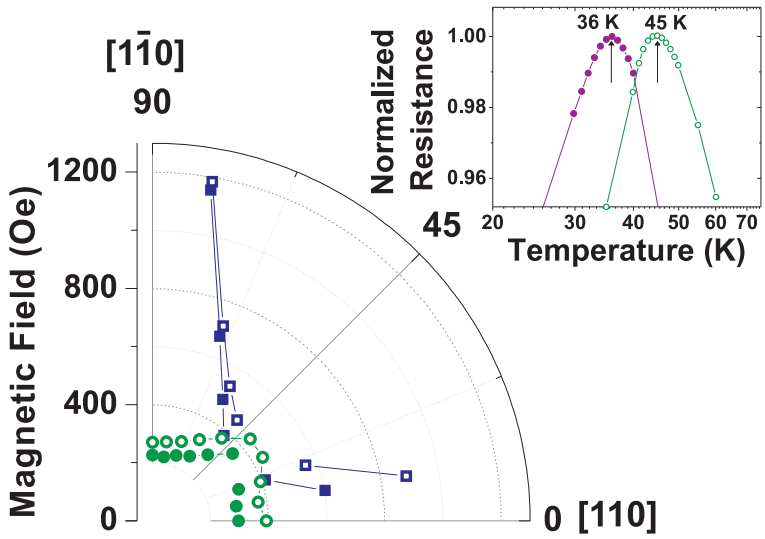

Figure 5.5: Coercive field as a function of the angle of the applied magnetic field with respect to the [110] direction at 1.5 K for sample B. An overall increase in the coercivity in all directions is observed upon adsorption of fluorescein which is attributed to a decrease in magnetization. The coercivity increase is larger for the 0° orientation due to a strengthening of the easy axis character of the [110] direction. The corresponding shift in Curie temperature for this sample is shown in the inset.

in agreement with the experiments. The adsorption of eosin Y produces a smaller decrease in the ferromagnetic transition temperature and a reduced increase in the electrical resistance with respect to fluorescein. An even less efficient hole quenching is observed for phloxine B where a slightly higher Curie temperature and a smaller resistance increase is observed with respect to eosin Y.
In summary, the effects of the molecule structure on the hole quenching capability could be clearly evidenced. These experiments show how the degree of modification of the electrical and magnetic properties of (Ga,Mn)As can be chosen almost at will by selecting the right chemical structure of the molecular adsorbates.

5.2.3 Magnetic anisotropy and transport properties in the absence of light

This section addresses the effects of the adsorption of fluorescein in further detail. Changes in the electrical properties and their correlation with the

Curie temperature were briefly discussed in section 5.2.1. To complete the analysis of the magnetic properties the effects on the magnetic anisotropy need to be addressed. To this end angle-resolved magneto-transport measurements were performed before and after the adsorption treatment and will be presented in the following.
In Fig. 5.5 the coercive fields H_{c1} (circles) and H_{c2} (squares) at a temperature of 1.5 Kelvin for (Ga,Mn)As (full symbols) and GaMnAs/fluorescein (open symbols) as a function of the direction of the applied magnetic field with respect to the [110] uniaxial easy axis direction are displayed. These plots correspond to sample B where like in sample A a reduction in Curie temperature was obtained upon adsorption of the dye. The corresponding shift ΔT= 9 Kelvin in the peak of the resistance vs. temperature measurement is shown in the inset (the resistance values are normalized to the peak resistance). After adsorption of the dye molecules the general profile of the anisotropy landscape given by the coercive field maps conserves the typical shape for as-grown materials: a rectangular shape with its long axis parallel to the [110] direction for the first coercive fields (H_{c1}, circles) and the second coercive fields (H_{c2}, squares) approaching the [110] and [1$\bar{1}$0] axes (see also section 3.1.1.) [54, 81].
After adsorption of the molecules in addition to the decrease in the value of T_c an overall increase of the coercive fields in all directions can be observed. This is in agreement with other studies in the literature reporting the decrease of the coercive field with increasing Curie temperature achieved by varying the manganese concentration [130]. A change in the magnetic anisotropy upon fluorescein adsorption is evidenced by a modest strengthening of the uniaxial easy axis ([110] axis, 0° direction) where the increase in coercivity is larger than along the uniaxial hard axis direction ([1$\bar{1}$0] axis, 90° direction): the ratio H_c[1$\bar{1}$0]/H_c[110] decreases from 0.75 for the as grown (Ga,Mn)As to 0.71 for GaMnAs/fluorescein indicating an approximately 5% increase in the easy axis character of the [110] direction. It has been shown both theoretically and experimentally that not only the Curie temperature but also the magnetic anisotropy in (Ga,Mn)As is susceptible to variations of the carrier density [35, 131, 132]. However, theory and experiments disagree when determining the anisotropy component (uniaxial or biaxial) that is most affected by changes in carrier concentration. Experimental work shows that the uniaxial term is most sensitive to variations in the carrier concentration, which can lead to a 90° change in the orientation of the uniaxial easy axis (from [$\bar{1}$10] to [110]) when reaching a critical value of the carrier density. A change of sign in the uniaxial magnetic anisotropy energy is not observed in the present study probably because of probing a hole concentration range that is far from the critical value. Nevertheless, the observation of a modest change

in the uniaxial anisotropy component with respect to the biaxial anisotropy component upon carrier concentration is clearly in line with results in the literature.
The general increase of coercivities in all directions was already discussed in terms of micromagnetic models in the last chapter dealing with the effects of oxygenation. In this case the same argument considering the domain wall pinning energy density $\epsilon = (\mathbf{M}_2 - \mathbf{M}_1) \cdot \mathbf{H}_c$ will be included in this analysis. Keeping in mind the small changes in the magnetic anisotropy after the adsorption of fluorescein we can assume that ϵ remains approximately constant for every direction. Therefore, once again according to the above expression a general increase in $\mathbf{H}_c$ could be directly related to a decrease in the absolute magnetization value M that is in agreement with the notion of a weakened ferromagnetic interaction given by the smaller value of Curie temperature after adsorption of fluorescein.

5.3 Manipulating magnetism by light

As mentioned in the introduction to this chapter the possibility of exploiting one more degree of freedom of the (Ga,Mn)As-fluorescein interaction will be explored by allowing the molecules to absorb light.
The interaction between light and (Ga,Mn)As with implications on the magnetic properties has been demonstrated by the injection of optically generated spin-polarized holes into the (Ga,Mn)As material causing changes in the magnetization [133]. In this thesis it is not intended to manipulate the magnetic properties by the direct interaction between (Ga,Mn)As and light. Instead, the approach involves modulating the hole quenching capability of the adsorbed fluorescein molecules as a sort of light regulated gating effect that enables the control of the magnetic properties by light.

5.3.1 Magnetic properties in the presence of light

The illumination experiments were started by shining the light on the magneto-transport devices at room temperature for approximately 30 minutes. The light was kept on also during the cool down of the sample and over the entire measurement time. As mentioned in the fist part of this chapter, the light source employed in all the experiments is a commercial mercury lamp. This lamp is also the light source used for the Kerr microscopy experiments presented in chapter 3.

Fig. 5.6 shows the effect of the illumination on sample A after the adsorption of fluorescein. A distinct shift of the resistance peak towards higher temperatures during illumination can be observed in Fig. 5.6 (top) which is accompanied by a decrease in the value of the resistance. In addition, a decrease in the value of the coercive field is observed in the field dependence of the planar Hall voltage as shown in Fig. 5.6 (bottom). Thus, the illumination effect is inverse to the pure adsorption effect and according to the previous discussion the effect can be attributed to an increase of hole carriers in (Ga,Mn)As by the action of light. The mechanism behind the illumination effect is possibly connected to the position in energy of the molecule ground and exited states with respect to the (Ga,Mn)As valence and conduction band edges. The molecule ground state is expected to be located close to the (Ga,Mn)As valence band in order to be able to effectively interact with the holes in these levels. Upon light absorption a fraction of these electrons that were interacting with the valence band are now being promoted to the excited state of the molecule, and are no longer able to contribute to the hole compensation producing a small increase in the hole concentration and an increase in the Curie temperature.

5.3.2 Time relaxation of the light induced state

The light effects presented in the last section are interpreted as the result of the promotion of electrons in the fluorescein molecules to electronic levels higher in energy. However, photodegradation of the molecules could also explain the observed behaviour. This possibility can be evaluated by testing the reversibility of the process. In the case of the light induced degradation of the molecular adsorbates a recovery of the original properties in the absence of light is not expected upon removal of the light source while if the excitation mechanism is valid the light effects should be reversible. In the present case it it found that the light induced state is reversible although the return to the original state occurs via a slow relaxation mechanism: Fig. 5.7 shows how the normalized resistance peak temperature slowly returns to the value before illumination. In this experiment after the resistance vs. temperature curve is completed (the last temperature point is taken at room temperature for all the plots presented in this study) the light is switched off and thereafter the complete temperature dependence of the resistance is remeasured repeatedly after waiting times of several hours, respectively. Fig. 5.7 a zoom-in of the curves obtained in the dark (filled symbols), during light illumination (open circles) and after waiting times at room temperature of 3 (open squares) and 21 (open triangles) hours after switching off the light

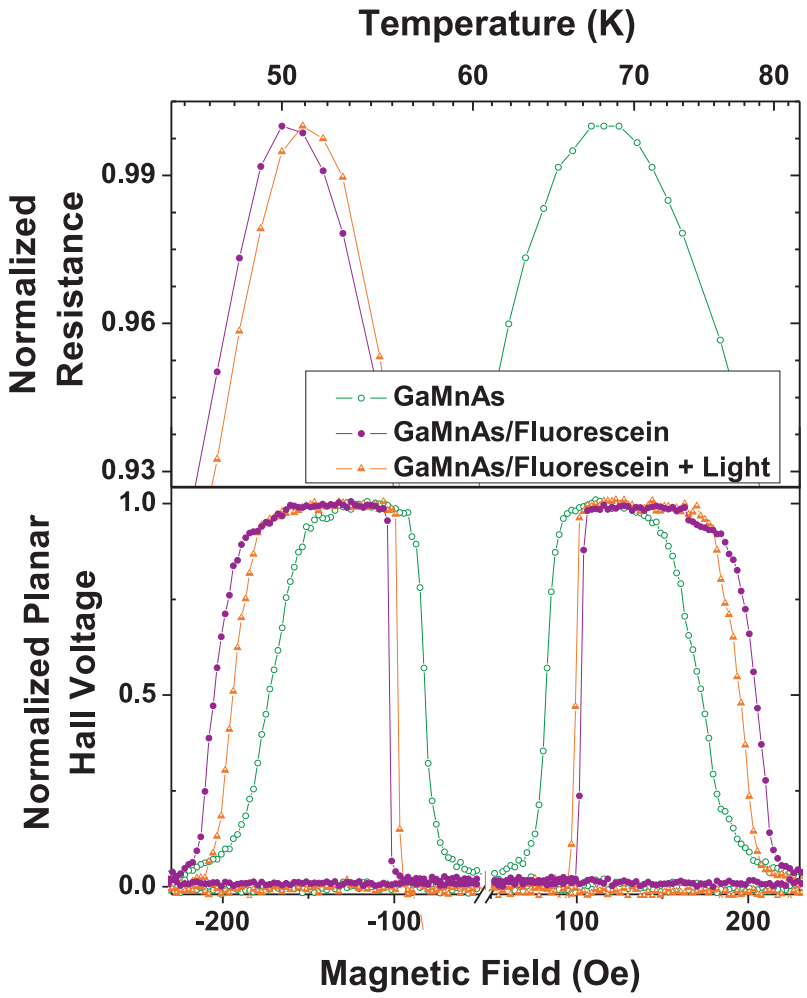

Figure 5.6: Light induced changes in the magnetic properties of GaMnAs/fluorescein. A shift in the Curie temperature towards higher values is observed upon illumination (top) together with a decrease in the value of the coercive field (bottom).

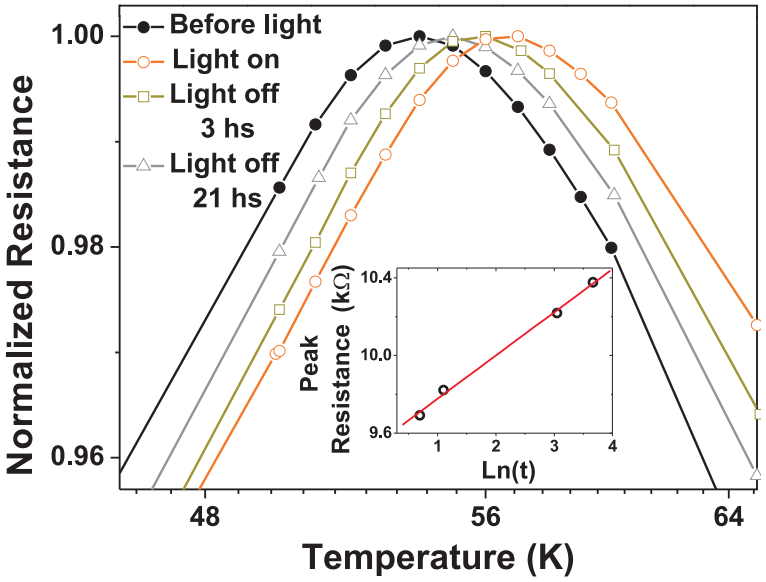

Figure 5.7: Relaxation effect after illumination. The resistance peak slowly moves towards the original position it had before illumination. The peak resistance as a function of the time (in hours) passed after removing the light source follows a logarithmic law.

source are shown.

Not only a shift in the temperature of the maximum resistance is observed during illumination but also the absolute value of the resistance decreases in the presence of light. Like the temperature where the resistance peak is observed, the maximum resistance also slowly recovers to the original value after switching off the light. The maximum resistance as well as the resistance peak temperature as a function of the waiting time have a logarithmic dependence. The plot of the peak temperature vs. the logarithm of time (in hours) and the corresponding linear fit are shown in the inset of Fig. 5.7. This rather unusual long relaxation time is also reflected in the values of the coercive fields.

The long time scales observed in this relaxation process well exceed any simple fluorescence or phosphorescence decay mechanism expected in fluorescein [134,135]. The physical explanation behind the long time scale relaxation remains an open question. Possible reasons explaining this long relaxation processes may be linked to charge trapping effects occurring at the interface

between the molecules and the (Ga,Mn)As substrate that might hinder the rapid relaxation of the light induced excited state. Nevertheless, these time relaxation measurements give important information supporting the idea of a reversible light switchable hole quenching mechanism in GaMnAs/organic systems that can influence the magnetic properties of the system by the interaction with light. They show that the effect is reversible and is not due to a photodegradation of the adsorbates.

In conclusion, the magneto-transport results presented in this chapter demonstrate the effectiveness of molecular layers in quenching hole carriers in different (Ga,Mn)As materials changing their magnetic properties. Most importantly this study shows how this interaction can be modified by light absorption of the molecular layers which is a first step towards light-controlled ferromagnetism in GaMnAs/dye devices. The reported observations provide a proof of principle for an effect that can be further explored using electron-acceptor molecules. These could help to improve the ferromagnetic response or even enhanced by functionalization with photoisomerizable molecules that can additionally provide non-volatility.

Summary and conclusions

In this thesis, the magnetic domain wall dynamics in the model ferromagnetic semiconductor (Ga,Mn)As were studied in detail. Kerr microscopy was the key technique for the observation of the magnetization dynamics processes at temperatures near and well below the ferromagnetic transition temperature. This work also presents the realization and low-temperature study of magneto-transport devices based on as-grown and modified (Ga,Mn)As thin films. The experimental work gathered in this thesis combines the scientific interest in the origin and understanding of physical phenomena with a practical view for potential applications.

The study of the time and space resolved magnetic domain wall dynamics of in-plane magnetized (Ga,Mn)As/GaAs by Kerr microscopy was presented in the third chapter of this manuscript. These measurements contribute to the understanding of a highly interesting topic where not many reports can be found in the literature. By working at variable temperatures the study of the magnetic domain wall dynamics in biaxial and uniaxial magnetic anisotropy regimes (at temperatures far below and in the vicinity of the ferromagnetic transition temperature, respectively) was performed. The magnetization reversal dynamics in (Ga,Mn)As was found highly susceptible to the in-plane magnetic anisotropy landscape. This was not only evidenced as a change in the internal structure of the magnetic domain walls going from an rotation of 120° to a complete 180° rotation of the magnetization but also as a dramatic change in the domain wall alignment. The irreversible magnetic aftereffect in (Ga,Mn)As was revealed by Kerr microscopy as a critical reduction in domain wall velocity over time under a constant magnetic field below coercivity. This behaviour is the result of a complex scenario where the overall time relaxation of the magnetization is the result of a combination of two individual relaxation processes acting simultaneously. The magnetization versus time measurements were successfully described by a biexponential model considering two coexisting relaxation processes. The model was used to estimate the time constants of the two relaxation processes and also the activation volumes that were found to be in agreement with the typical val-

ues for (Ga,Mn)As.
Some questions still remain open such as the origin of the distinct domain wall alignment of 120° domain walls at the lowest temperatures, however, a step forward in the understanding of the complex domain wall dynamics in (Ga,Mn)As/GaAs has been made. The study of the domain wall dynamics and magnetic anisotropy at temperatures closer to the ferromagnetic transition temperature is important in view of the relatively low values found in (Ga,Mn)As materials. As the room temperature ferromagnetism in (Ga,Mn)As seems at this moment not in sight it is fundamental for any possible application that its properties are fully characterized at the highest possible temperatures below the ferromagnetic-to-paramagnetic transition. The analysis of the magnetic aftereffect which is typically found in ferromagnetic materials, links and compares the distinct hole carrier mediated ferromagnetism found in ferromagnetic semiconductors to the more conventional and more extensively studied magnetism found in standard magnetic materials where the direct exchange interaction plays the dominant role.
Undoubtedly, from the results presented in this thesis those that are more practically oriented are the ones related to the modification of the properties of as-grown (Ga,Mn)As materials presented in chapter 4 and 5. In both cases the corresponding treatment was performed on micro-patterned (Ga,Mn)As devices that allowed for the detection of the changes in the magnetic and electrical properties by magneto-transport measurements. The first example is the controlled suppression of the ferromagnetic properties successfully achieved by the incorporation of oxygen species into the (Ga,Mn)As structure by oxygen plasma exposure. This method does not only allow for the regulation of the carrier density after completion of the standard material growth procedure but can also be applied to large extensions of a film. In fact the most interesting aspect of this large scale treatment is the potential applications related to the design of suitable masks that could provide the selective exposure of certain parts of the films to the treatment. In this way, isolated regions or even arrays of features with different magnetic properties with respect to the rest of the film could be easily achieved in one step. These arrays can be of use for the study of the interaction between different types of domain walls in addition to the more applied concept of specifically located domain wall switching units incorporated in single domain devices.
The second example of a controlled modification of the properties of as-grown (Ga,Mn)As is surface functionalization. In this case the possibilities that are open for tuning the properties of the magnetic substrate scale with the infinite number of different adsorbates that can be used. In this particular case the selected functionality of the adsorbates was the absorption of light in the visible range. This selection was made in order to explore the pos-

sibility of realizing photo-sensitized (Ga,Mn)As devices where the magnetic and electrical properties can be influenced by light exposure. In this work, proof-of-principles for this concept were successfully obtained employing fluorescein molecules as adsorbates.

The study of the effects of light on the electrical and magnetic properties of the (Ga,Mn)As/fluorescein devices can be readily continued in view of enhancing the effect and also for achieving a better understanding of the underlying mechanism. As an example, a dependence of the light effect on the wavelengths of the incident light can reveal a wavelength window where the light effect is maximum therefore giving room for a major improvement with respect to the white light illumination that has been employed so far. In addition, a dependence of the light effect on the dipping time could give important information regarding the role of the additional less tightly bound molecular layers (in addition to the first monolayer in direct contact with the (Ga,Mn)As substrate) in the light induced process. In this view point it would be highly desirable to analyze relaxation times after illumination in the presence of substantially different amounts of weakly bound layers.

Moving on from the (Ga,Mn)As/fluorescein system, improvements can be most likely achieved by choosing adsorbates that enhance the effect. This can be done by employing adsorbates with a larger electron-donation capability and a larger absorbance (extinction coefficient of fluorescein: 88000 mol^{-1} cm^{-1} at 513 nm) in the visible range such as Cy2 or Dy-590, two commercial dyes whose chemical composition is rich in alkyl chains and conjugated structures. These dyes have ${SO_3}^{-1}$ and ${CO_2}^{-1}$ potential binding groups and extinction coefficients of 150000 mol^{-1} cm^{-1} at 561 nm and 120000 mol^{-1} cm^{-1} at 580 nm, respectively. The use of such adsorbates on (Ga,Mn)As films with a relatively low hole carrier concentration could lead to the full quenching of the hole carriers in the absence of light. In this case another functionality could be achieved and investigated, the system described above would be insulating and paramagnetic in the dark and would become not only conductive but also ferromagnetic in the presence of light. This effect could be interesting from the point of view of applications in magneto-transport devices. It would allow for a fully light operated on-off electric and magnetic state in a magneto-transport device. Additionally, this experiments would complement the presented studies in highly conductive systems and help to understand the physical mechanism of this type of secondary interaction between the light and the (Ga,Mn)As material.

It is well known that magnetic anisotropy transitions (in-plane to out-of-plane or 90° easy axis reorientations within the plane) in (Ga,Mn)As can occur when the carrier density is changed provided that the films have an initial critical value of the charge carrier density. If the light effect can be enhanced

by the use of a more effective electron donor, working with (Ga,Mn)As films that have a hole carrier concentration in the vicinity of a critical anisotropy transition value could be of considerable interest. The molecule adsorption could drive the system to one side of the anisotropy transition and ideally the interaction with light could cause the system to cross the anisotropy transition back to the initial state. This could allow for a light operated easy-axis reorientation that in turn can provoke a light driven reorientation of the magnetization vector in the absence of magnetic fields.
Another important point that can be investigated is the possibility of achieving non-volatility in the light effect. This could be explored by the use of, for instance, photoisomerizable molecular adsorbates. This adsorbates would undergo a conformational change in the presence of light that would not be reversed by the removal of the light source as it is in the present case since chemical bonds are broken and reformed in the process. This would allow for the reliable and stable operation of the functionalized devices in either the more or less conductive (ferromagnetic) state without the need of constant illumination.
Due to the fact that this effect arises from surface functionalization there are an almost endless number of other promising routes to follow not proposed here. It would be highly desirable that the proof-of-principles presented in this thesis motivates further research activities in this direction.

Appendix

This appendix contains a summary of the most relevant properties of the samples studied in the different chapters of this thesis.

Chapter/section	Sample name
3/DW dynamics	37F
3/Aftereffect	17H, 264
4	11G, 32H
5	32H, 264

Sample name	Thickness (nm)	T_c (K)	Mn concentration (%)	MBE Laboratory
37F	170	49	5	Rome[1]
264	50	65	8	Nottingham[2]
17H	170	53	2.5	Rome
11G	170	22	1.2	Rome
32H	40	48	3	Rome

1: E. Placidi and F. Arciprete at Dipartimento di Fisica, Università di Roma "Tor Vergata".

2: A. W. Rushforth, R. P. Campion and B. L. Gallagher at School of Physics and Astronomy, University of Nottingham.

Bibliography

[1] B. T. Matthias, R. M. Bozorth, J. H. Van Vleck, Phys. Rev. Lett. **7**, 160 (1961).

[2] A. Mauger, C. Godart, Phys. Rep. **141**, 51 - 176 (1986).

[3] S. Kawabataa, Y. Asanoc, Y. Tanakad, S. Kashiwayae, Physica C **469**, 1621 (2009).

[4] T. Story, R. R. Galazka, R. B. Frankel,P. A. Wolff, Phys. Rev. Lett. **56**, 777 (1986).

[5] A. H. MacDonald, P. Schiffer, N. Samarth, Nature Mater. **4**, 195 (2005).

[6] H. Ohno, Science **281**, 951 (1998).

[7] H. Munekata, H. Ohno, S. von Molnár, Armin Segmller, L. L. Chang, and L. Esaki, Phys. Rev. Lett. **63**, 1849 (1989).

[8] H. Ohno, H. Munekata, T. Penney, S. von Molnár, L. L. Chang, Phys. Rev. Lett. **68**, 2664 (1992).

[9] H. Ohno, A. Shen, F. Matsukura, A. Oiwa, A. Endo, S. Katsumoto, Y. Iye, Appl. Phys. Lett. **69**, 363 (1996).

[10] J. Schiemann, J. König, H. H. Lin, A. H. MacDonald, Appl. Phys. Lett. **78**, 1550 (2001).

[11] H. Saito, V. Zayets, S. Yamagata, A. Ando, Phys. Rev. Lett. **90**, 207202 (2003).

[12] N. A. Theodoropouloua, A. F. Hebarda, D. P. Norton, J. D. Budaic, L. A. Boatnerc, J. S. Leed, Z. G. Khimd, Y. D. Parkd, M. E. Overbergb, S. J. Peartonb, R. G. Wilson, Solid State Electron. **47**, 2231 (2003).

[13] J. M. D. Coey, A. P. Douvalis, C. B. Fitzgerald, M. Venkatesan, Appl. Phys. Lett. **84**, 1332 (2004).

[14] M. A. Scarpulla, O. D. Dubon, K. M. Yu, O. Monteiro, M. R. Pillai, M. J. Aziz, M. C. Ridgway, Appl. Phys. Lett. **82**, 1251 (2003).

[15] O. V. Vikhrova, Y. A. Danilov, E. S. Demidov, B. N. Zvonkov, V. I. Kovalev, Z. E. Kunkova, V. V. Podolskii, M. V. Sapozhnikov, A. I. Suchkov, M. P. Temiryazeva, Bullet. Russ. Acad. Sc.: Phys. **71**, 32 (2007).

[16] A. Shen, H. Ohno, F. Matsukura, Y. Sugawara, N. Akiba, T. Kuroiwa, A. Oiwa, A. Endo, S. Katsumoto, Y. Iye, J. Cryst. Growth **175**, 1069 (1997).

[17] R. K. Kawakami, E. Johnston-Halpering, L. F. Chen, M. Hanson, N. Guébels, J. M. Stephens, J. S. Speck, A. C. Gossard, D. D. Awschalom, Materials Science and Engineering B **88**, 209 (2002).

[18] S. Sanvito, N. A. Hill, Appl. Phys. Lett. **96**, 530 (2009).

[19] A. Wolos, M. Kaminska, M. Palczewska, A. Twardowski, X. Liu, T. Wojtowicz, J. K. Furdyna, J. Appl. Phys. **78**, 3493 (2001).

[20] R. C. Myers, B. L. Sheu, A. W. Jackson, A. C. Gossard, P. Schiffer, N. Samarth, D. D. Awschalom, Phys. Rev. B **74**, 155203 (2006).

[21] K. M. Yu, W. Walukiewicz, T. Wojtowicz, I. Kuryliszyn, X. Liu, Y. Sasaki, J. K. Furdyna, Phys. Rev. B **65**, 201303(R) (2002).

[22] H. Ohno, F. Matsukura, Y. Ohno, Mat. Sc. and Eng. B **84**, 70 (2001).

[23] R. Shioda, K. Ando, T. Hayashi, M. Tanaka, Phys. Rev. B **58**, 1100 (1998).

[24] K. Y. Wang, K. W. Edmonds, R. P. Campion, B. L. Gallagher, N. R. S. Farley, C. T. Foxon, M. Sawicki, P. Boguslawski, T. Dietl, Appl. Phys. Lett. **95**, 6512 (2004).

[25] J. Blinowski, P. Kacman, Phys. Rev. B **67**, 121204 (2003).

[26] F. Matsukura, H. Ohno, A. Shen, Y. Sugawara, Phys. Rev. B **57**, 2037 (1998).

[27] P. A. Korzhavyi, I. A. Abrikosov, E. A. Smirnova, L. Bergqvist, P. Mohn, R. Mathieu, P. Svedlindh, J. Sadowski, E. I. Isaev, Yu. Kh. Vekilov, O. Eriksson, Phys. Rev. Lett. **88**, 187202 (2002).

[28] T. Hayashi, Y. Hashimoto, S. Katsumoto, Y. Iye, Appl. Phys. Lett. **78**, 1691 (2001).

[29] K. W. Edmonds, P. Bogusawski, K. Y. Wang, R. P. Campion, S. N. Novikov , N. R. S. Farley, B. L. Gallagher, C. T. Foxon, M. Sawicki, T. Dietl, M. Buongiorno Nardelli, and J. Bernholc, Phys. Rev. Lett. **92**, 037201 (2004).

[30] M. Malfait, J. Vanacken, V. V. Moshchalkov, W. Van Roy, G. Borghs, Appl. Phys. Lett. **86**, 132501 (2005).

[31] C. Zener, Phys. Rev. **81**, 440 (1950).

[32] C. Zener, Phys. Rev. **83**, 299 (1950).

[33] T. Dietl, A. Haury, Y. Merle d'Aubigné, Phys. Rev. B **55**, R3347 (1997).

[34] T. Dietl, H. Ohno, F. Matsukura, J. Cibert, D. Ferrand, Science **287**, 1019 (2000).

[35] T. Dietl, H. Ohno, F. Matsukura, Phys. Rev. B **63**, 195205 (2001).

[36] L. Thevenard, L. Largeau, O. Mauguin, A. Lemaître, K. Khazen, H. J. von Bardeleben, Phys. Rev. B. **75**, 195218 (2007).

[37] P. Boguslawsky, I. Gorczyca, Semicond. Sc. Technol. **9**, 2169 (1994).

[38] A. K. Bhattacharjee, G. Fishman, B. Coqblin, Physica **117B/118B**, 449 (1983).

[39] T. Jungwirth, J. Maek, K. Y. Wang, K. W. Edmonds, M. Sawicki, M. Polini, Jairo Sinova, A. H. MacDonald, R. P. Campion, L. X. Zhao, N. R. S. Farley, T. K. Johal, G. van der Laan, C. T. Foxon, B. L. Gallagher, Phys. Rev. B **73**, 165205 (2006).

[40] B. Sanyal, O. Bengone, S. Mirbt , Phys. Rev. B **68**, 205210 (2003).

[41] X. Luo, R. M. Martin, Phys. Rev. B **72**, 035212 (2005).

[42] J. Kreissl, W. Ulrici, M. El-Metoui, A.-M. Vasson, A. Vasson, A. Gavaix, Phys. Rev. B **54**, 10508 (1996).

[43] M. Sawicki, F. Matsukura, A. Idziaszek, T. Dietl, G. M. Schott, C. Ruester, C. Gould, G. Karczewski, G. Schmidt, L. W. Molenkamp, Phys. Rev. B **70**, 245325 (2004).

[44] K. Hamaya, T. Taniyama, Y. Kitamoto, T. Fujii, Y. Yamazaki, Phys. Rev. Lett. **94**, 147203 (2005).

[45] F. Matsukuraa, A. Oiwab, A. Shena, Y. Sugawaraa, N. Akibaa, T. Kuroiwaa, H. Ohnoa, A. Endob, S. Katsumotob, Y. Iyeb, Appl. Surf. Sci. **178**, 113 (1997).

[46] L. Thevenard, L. Largeau, O. Mauguin, G. Patriarche, A. Lemaître, N. Vernier and J. Ferré, Phys. Rev. B **73**, 195331 (2006).

[47] J. Daeubler, S. Schwaigera, M. Glunka, M. Tabora, W. Schocha, R. Sauera, W. Limmer, Phys. E **40**, 1876 (2008).

[48] I. Stolichnov, S. W. E. Riester, H. J. Trodahl, N. Setter, A. W. Rushforth, K. W. Edmonds, R. P. Campion, C. T. Foxon, B. L. Gallagher, T. Jungwirth, Nature Mater. **7**, 264 (2008).

[49] A. W. Rushforth, E. De Ranieri, J. Zemen, J. Wunderlich, K. W. Edmonds, C. S. King, E. Ahmad, R. P. Campion, C. T. Foxon, B. L. Gallagher, K. Výborný, J. Kučera, and T. Jungwirth, Phys. Rev. B **78**, 085314 (2008).

[50] C. Bihler, M. Althammer, A. Brandlmaier, S. Geprägs, M. Weiler, M. Opel, W. Schoch, W. Limmer, R. Gross, M. S. Brandt, S. T. B. Goennenwein , Phys. Rev. B **78**, 045203 (2008).

[51] M. Sawicky, K.-Y. Wang, K. W. Edmonds, R. P. Campion, C. R. Staddon, N. R. S. Farley, C. T. Foxon, T. Dietl, B. L. Gallagher, Mat. Sc. Pol. **24**, 627 (2006).

[52] M. Abolfath, T. Jungwirth, J. Brum, A. H. MacDonald, Phys. Rev. B **63**, 054418 (2001).

[53] U. Welp, V. K. Vlasko-Vlasov, X. Liu, J. K. Furdyna, T. Wojtowicz, Phys. Rev. Lett. **90**, 167206 (2003).

[54] H.X. Tang, R.K. Kawakami, D.D. Awschalom, M.L. Roukes, Phys. Rev. Lett. **90**, 107201 (2003).

[55] K. Pappert, C. Gould, M. Sawicki, J. Wenisch, K. Brunner, G. Schmidt, L. W. Molenkamp, New J. Phys. **9**, 354 (2007).

[56] K.-Y. Wang, M. Sawicki, K. W. Edmonds, R. P. Campion, S. Maat, C. T. Foxon, B. L. Gallagher, T. Diet, Phys. Rev. Lett. **95**, 217204 (2005).

[57] H.B. Callen, E. Callen, J. Phys. Chem. Solids **27**, 1271 (1966).

[58] P. Weiss, J. Phys. Rad. **9**, 373 (1907).

[59] W. Heisenberg, Z. Phys. **49**, 619 (1928).

[60] H. Barkhausen, Phys. Z. **20**, 401 (1919).

[61] A. Hubert, R. Schäfer, *Magnetic Domains: the analysis of Magnetic Microstructures* , Springer (2000).

[62] K. H. Stewart, *Ferromagnetic Domains* , Cambridge University Press (1954).

[63] D. J. Craik, R. S. Tebble, *Ferromagnetism and Ferromagnetic Domains* , Nord Holland Publishing Company (1965).

[64] L. D. Landau, E. Lifshitz, Phys. Z. Sowjetunion **8** , 153 (1935).

[65] R. S. Tebble, *Magnetic Domains* , Methuens Monographs on Physical Subjects (1969).

[66] R. OHandley, *Modern Magnetic Materials: Principles and Aplications* , Wiley Interscience (2000).

[67] N. Inaba, M. Futamoto, , J. Magn. Magn. Mater. **226-230**, 1014 (2001).

[68] R. Carey, E. D. Isaac, *Magnetic domains and techniques for their observation* , Academic Press (1966).

[69] I. Horcas, R. Fernández, J. M. Gómez-Rodríguez, J. Colchero, Rev. Sci. Instrum. **78**, 013705 (2007).

[70] M. N. Baibich, J. M. Broto, A. Fert, F. Nguyen Van Dau, F. Petroff, P. Eitenne, G. Creuzet, A. Friederich, J. Chazelas, Phys. Rev. Lett. **21**, 2472 (1988).

[71] G. Binasch, P. Grünberg, F. Saurenbach, W. Zinn, Phys. Rev. B 95bf39, 4828 (1989).

[72] N. Nagaosa, J. Sinova, S. Onoda, A. H. MacDonald, N. P. Ong, arXiv:0904.4154v1.

[73] N. P. Ong, W.-L. Lee, in *Foundations of quantum mechanics in the light of new technology (ISQM Tokio 2005)*edited by S. Ishioka and K. Fujikawa (World Scientific), p. 121, eprint arXiv:cond-mat/0508236.

[74] T. Jungwirth, Q. Niu, A. H. MacDonald, Phys. Rev. Lett. **88**, 207208 (2002).

[75] K. W. Edmonds, R. P. Campion, K. Y. Wang, A. C. Neumann, B. L. Gallagher, C. T. Foxon, P. C. Main, J. Appl. Phys. **93**, 6787 (2003).

[76] K. W. Edmonds, K. Y. Wang, R. P. Campion, A. C. Neumann, C. T. Foxon, B. L. Gallagher, P. C. Main, Appl. Phys.Lett. **81**, 3010 (2002).

[77] C. Gould, K. Pappert, G. Schmidt, L. W. Molenkamp, Adv. Mat. **19**, 323 (2007).

[78] A. Van Esch, L. Van Bockstal, L. Van Bockstal, G. Verbanck, A. S. van Steenbergen, P. J. Wellmann, B. Grietens, R. Bogaerts, F. Herlach, G. Borghs, Phys. Rev. B **56**, 13103 (1997).

[79] V. Novák, K. Olejník, J. Wunderlich, M. Cukr, K. Výborný, A. W. Rushforth, K. W. Edmonds, R. P. Campion, B. L. Gallagher, Jairo Sinova, T. Jungwirth, Phys. Rev. Lett. **101**, 077201 (2008).

[80] C. M. Hurd, *The Hall effect in metals and alloys* , Plenum Press (1972).

[81] L. Herrera Diez, R. K. Kremer, A. Enders, M. Rössle, E. Arac, J. Honolka, K. Kern, E. Placidi, F. Arciprete, Phys. Rev. B **78**, 155310 (2008).

[82] J. Honolka, L. Herrera Diez, R. K. Kremer, K. Kern, E. Placidi, F. Arciprete, New J. Phys. **12**, 093022 (2010).

[83] A Hubert, IEEE Trans. Mag. **15**, 1251 (1979).

[84] H. Kronmüller, *Nachwirkung in Ferromagnetika*, p. 63, Springer-Verlag, Berlin/Heidelberg/New York 1968.

[85] L. Néel, J. Phys. Radium **11**, 49 (1950).

[86] L. Néel, J. Phys. Radium **12**, 339 (1951).

[87] L. Néel, J. Phys. Rad. **13**, 269 (1952).

[88] J. L. Snoek, Physica **5**, 663 (1938).

[89] H. Kronmüller, *Topics in Applied Physics: Hydrogen in metals I, Chapter 11*, p. 289, Springer-Verlag, Berlin/Heidelberg/New York 1968.

[90] K.M. Yu, W. Walukiewicz, T. Wojtowicz, I. Kuryliszyn, X. Liu, Y. Sasaki, J.K. Furdyna, Phys. Rev. B **65**, 201303(R) (2002).

[91] J. Mašek, F. Máca, Phys. Rev. B **69**, 165212 (2004).

[92] E. P. Wohlfarth, J. Phys. F: Met. Phys. **14**, L155 (1984).

[93] G. Bayreuther, P. Bruno, G. Lugert, C. Turtur, Phys. Rev. B **40**, 7399 (1989).

[94] A. Kirilyuk, J. Giergiel, J. Shen, J. Kirschner, J. Magn. Magn. Mater. **159**, L27 (1996).

[95] E. P. Wohlfarth, J. Phys. F: Met. Phys. **14**, L155 (1984).

[96] N. Fujiwara, H. Tutu and H. Fujisaka, Prog. Theor. Phys. Suppl. No. 161, (2006).

[97] M. Sirena, L. B. Steren, J. Guimpel, Phys. Rev. B **64**, 104409 (2001).

[98] B. Hohler, H. Schreyer, J. Phys. F: Met. Phys **12**, 857 (1982) 354.

[99] A. Lisfi, J. C. Lodder, P. de Haan, T. Bolhuis, F. J. G. Roesthuis, J. Magn. Magn. Mater. **193**, 258 (1999).

[100] J. F. Liu, H. L. Luo, J. Magn. Magn. Mater. **94**, 43 (1991).

[101] P. J. Thompson, R. Street, J. Magn. Magn. Mater. **171**, 153 (1997).

[102] P. Gaunt, J. Appl. Phys. **59**, 4129 (1986).

[103] Sug-Bong Choe, Dong-Hyun Kim, Kwang-Su Ryu, Hae-Seung Lee, Sung-Chul Shin, J. Appl. Phys. **99**, 103902 (2006).

[104] M. Labrune, S. Andrieu, F. Rio, P. Bernstein, J. Magn. Magn. Mater. **80**, 211 (1989).

[105] H. X. Tang, R. K. Kawakami, D. D. Awschalom, M. L. Roukes, Phys. Rev. B **74**, 041310(R) (2006).

[106] A. Dourlat, V. Jeudy, L. Thevenard, A. Lemaître, C. Gourdon, J. Supercond. Nov. Magn. **20**, 453 (2007).

[107] S. T. B. Goennenwein, T. A. Wassner, H. Huebl, M. S. Brandt, J. B. Philipp, M. Opel, R. Gross, A. Koeder, W. Schoch, A. Waag , Phys. Rev. Lett. **92**, 227202 (2004).

[108] L. Thevenard, L. Largeau, O. Mauguin, A. Lemaître, B. Theys , Appl. Phys. Lett. **87**, 182506 (2005).

[109] http://www.pvateplaamerica.com.

[110] M. Tanaka , H. Shimizua, M. Miyamuraa , J. Cryst. Growth **227-228**, 839 (2001).

[111] J. F. Watts, J. Wolstenholme, *An introduction to surface analysis by XPS and AES*, Wiley, New York, Weinheim 2003.

[112] G. S. Chang, E Z Kurmaev, L. D. Finkelstein, H. K. Choi, W. O. Lee, Y. D. Park, T. M. Pedersen, A. Moewes , J. Phys.: Condens. Matter **19**, 076215 (2007).

[113] W. Storm, D. Wolany, F Schröder, G. Becker, B. Burkhardt, L. Wiedmann, A. Benninghoven , J. Vac. Sci. Technol. B **12**, 147 (1994).

[114] J. T. Wolan, C. K. Mount, G. B. Hoflund , Appl. Phys. Lett. **72**, 1469 (1998).

[115] W. Ranke, Y. R. Xing, G. D. Shen , Surface Sci. **122**, 256 (1982).

[116] D. C. Koningsberger, *X-ray absorption*, Wiley, New York, 1988.

[117] F. Maccherozzi, G. Panaccione, G. Rossi, M. Hochstrasser, M. Sperl, M. Reinwald, G. Woltersdorf, W. Wegscheider, C. H. Back, Phys. Rev. B **74**, 104421 (2006).

[118] Y. Ishiwata, M. Watanabe, R. Eguchi, T. Takeuchi, Y. Harada, A. Chainani, S. Shin, T. Hayashi, Y. Hashimoto, S. Katsumoto, Y. Iye, Phys. Rev. B **65**, 233201 (2002).

[119] S. Kobayashi, I. R. M. Kottegoda, Y. Uchimoto, M. Wakihara , J. Mater. Chem **14**, 1843 (2004).

[120] F. M. F. de Groot, M. Grioni, J. C. Fuggle, J. Ghijsen, G. A. Sawatzky and H. Petersen, Phys. Rev. B **40**, 5715 (1989).

[121] B. Gilbert, B. H. Frazer, A. Belz, P. G. Conrad, K. H. Nealson, D. Haskel, J. C. Lang, G. Srajer, G. De Stasio, J. Phys. Chem. A, **107**, 2839 (2003).

[122] D. M. Sherman, Am. Mineral., **69**, 788 (1984).

[123] W. Orellana, A. C. Ferraz, Phys. Rev. B **61**, 5326 (2000).

[124] G. Bouzerar, T. Ziman, J. Kudrnovsk, Europhys. Lett.**69**, 812 (2005).

[125] Chiba, M. Sawicki, Y. Nishitani, Y. Nakatani, F. Matsukura, H. Ohno, Nature **455**, 515 (2008).

[126] I. Carmeli, F. Bloom, E. G. Gwinn, T. C. Kreutz, C. Scoby, A. C. Gossard, S. G. Ray, Ron Naaman, Appl. Phys. Lett. **89**, 112508 (2006).

[127] J. N. O′Shea, J. B. Taylor, E. F. Smith, Surf. Sci. **548**, 317 (2004).

[128] Hwei-Heng Wang, Dei-Wei Chou, Jau-Yi Wu, Yeong-Her Wang,Mau-Phon Houng , Jpn. J. Appl. Phys. **39**, 4477 (2000).

[129] Y. Lu, J. C. Le Breton, P. Turban, B. Lépine, P. Schieffer, and G. Jézéquel, Appl. Phys. Lett. **88**, 042108 (2006).

[130] S. J. Potashnik, K. C. Ku, R. F. Wang, M. B. Stone, N. Samarth, P. Schiffer, S. H. Chun, J. Appl. Phys. **93**, 6784 (2003).

[131] Chiba, M. Sawicki, Y. Nishitani, Y. Nakatani, F. Matsukura, H. Ohno, Nature **455**, 515 (2008).

[132] M. Sawicki, K.-Y. Wang, K. W. Edmonds, R. P. Campion, C. R. Staddon, N. R. S. Farley, C. T. Foxon, E. Papis, E. Kamińska, A. Piotrowska, T. Dietl, B. L. Gallagher, Phys. Rev. B **71**, 121302 (2005).

[133] A. Oiwa, Y. Mitsumori, R. Moriya, T. Słupinski, H. Munekata, Phys. Rev. Lett. **88**, 137202 (2002).

[134] U. Resch-Genger, M. Grabolle, S. Cavaliere-Jaricot, R. Nitschke, T. Nann, Nature Meth. **5**, 763 (2008).

[135] L. Song, C. A. G. O. Varma, J. W. Verhoeven, H. J. Tanke, Biophys. J. **70**, 107201 (1996).

Publications

- L. Herrera Diez, R. K. Kremer, A. Enders, M. Rössle, E. Arac, J. Honolka, K. Kern, E. Placidi, F. Arciprete, *"Complex domain wall dynamics in compressively strained GaMnAs epilayers"* Phys. Rev. B **78**, 155310 (2008).

- L. Herrera Diez, J. Honolka, K. Kern, H. Kronmüller, E. Placidi, F. Arciprete A. W. Rushforth, R. P. Campion, B. L. Gallagher, *"Magnetic aftereffect in compressively strained GaMnAs studied using Kerr microscopy"* Phys. Rev. B **81**, 094412 (2010).

- J. Honolka, L. Herrera Diez, R. K. Kremer, K. Kern, E. Placidi, F. Arciprete, *"Temperature dependent Néel wall dynamics in GaMnAs/GaAs"* New J. Phys. **12**, 093022 (2010).

- L. Herrera Diez, M. Konuma, E. Placidi, F. Arciprete A. W. Rushforth, R. P. Campion, B. L. Gallagher,J. Honolka, K. Kern, *"Manipulation of ferromagnetic properties of photo-sensitized GaMnAs"* (submitted).

- L. Herrera Diez, M. Konuma, J. Honolka, K. Kern, E. Placidi, F. Arciprete, *"Magnetic properties of oxygenated GaMnAs"* (submitted).

Curriculum vitae

Name	Liza Herrera Diez
Date of Birth	September 20, 1984
Nationality	Argentine
1998-2002	High School at Centro Polivalente de Arte and Complejo Educativo Santiago Besso, Merlo, San Luis, Argentina.
2003-2006	Studies in Chemistry, Licenciatura en Química, Universidad Nacional de Córdoba, Córdoba, Argentina.
2007	Master thesis: "Magneto-optical and magneto-transport investigations of diluted ferromagnetic semiconductors", Abteilung Kern, Max-Planck-Institut für Festkörperforschung, Stuttgart, Germany.
2008-2010	Doctoral work in the group of Prof. K. Kern, Max-Planck-Institut für Festkörperforschung, Stuttgart, Germany.

Acknowledgments

I would like to thank in the first place Prof. Klaus Kern for giving me the opportunity to carry out my doctoral work in his group. His own passion for science is responsible for the unique work environment in the group. Here scientific work means the privilege of being in touch with the very heart of nature, and not a fixed number of hours per day. 'We do not work in a bakery!'... I could not agree more.
I have not enough words for my supervisor Dr. Jan Honolka. He is never too busy, never too tired and never too far. The most meticulous and inquiring of all reviewers and at the same time most encouraging and supportive. I owe to you the entirety of this work, I thank you deeply for your patience and extreme dedication, for always having a smile across your face and, of course, for the Marillenknödel and many wonderful memories.
One big *GRACIAS* to Magalí Lingenfelder, for playing a key role in the realization of this german adventure and later for being a great friend *a la Argentina*.
I have to thank Ravi Shankar Sundaram, my office pal and dear friend for the exceedingly complicated task of dealing with me every day. Thank you for understanding me, for the discussions about each other's research, and for playing Pink Floyd over and over again!
Special thanks to Steffen Kahle for still finding good company in my proud stubbornness and for being such a caring friend. It has been a most delightful series of disagreements.
I also owe hundreds of unforgettable memories to Sören Krotsky, Tobias Herden, Thomas Maurer, Robin Ohmann, Maximilian Assig, Violetta Sessi, Tanya Kurkina, Vivek Pachauri and Charlène Tonnoir. Chocolate party, bad movies and great food, S21, vodka on fire, Cannstatter Wasen, Schönes Wochenende ticket, Viking festivals, Genazzano, pasta and pesto, that one cabinet full of liquor...
Thanks to my 'second order office mate' Nassim Rafiefard and also to Markus Ternes, Axel Enders, Simon Hertenberger, Kannan Balasubramanian, Christian Michaelis, Adarsh Sagar, Sebastian Stepanow, Theresa Lutz, Isabella

Gierz, Christian Ast, Ulrich Stützel, Alexander Bittner, Lucia Vitali and many other current and former members of the department for being part of the wonderful times I had at the MPI.
I must thank my dear friend Jimena Olmos Asar for always being there for me across the ocean... we will always be around the corner!
Thanks to Sabine Birtel for being the most charming and incredibly efficient secretary.
I would like to thank the cleanroom crew, Achim Güth, Thomas Reindl and Ulrique Waizmann for shearing their time and experience with me and to the wonderful people of the Technology Group, Benjamin Stuhlhofer, Marion Hagel, Birgit Lemke and Stephan Schmid for their outstanding efficiency and kindness. Thanks to Ernesto Placidi and Fabrizio Arciprete in Rome and Andrew Rushforth, Kevin Edmonds and Bryan Gallagher in Nottingham for (Ga,Mn)As samples and for a most enriching scientific collaboration. I also have to thank Helmut Kronmüller for many fruitful scientific discussions and Ravi Shankar Sundaram, Kannan Balasubramanian and Thomas Weitz for their invaluable help with experimental work. I am also indebted to Eva Brücher and Mitsuharu Konuma at the chemistry and interface analysis service groups for their dedication and inestimable support with SQUID and XPS measurements.
At last I thank from the bottom of my heart Mifta, my mother. Thank you for showing me how it is not to give up, how to have things the right way or not at all and how a dream is never too big. I am home anywhere if you are there, everything I do is always dedicated to you.